Wrocław University
of Science and Technology

DOCTORAL THESIS

Laser powder bed fusion technology as an alternative method of metallic glasses manufacturing

mgr inż. Łukasz Szczepański

Supervisors: dr hab. inż. Tomasz Kurzynowski
Prof. Dr.-Ing. habil. Markus Bambach

Key words: *Laser Powder Bed Fusion (L-PBF), Additive Manufacturing, Metallic Glasses, Fe-based alloys, microstructure, hardness*

WROCŁAW 2023

Interdisciplinarity of the doctoral dissertation

The doctoral dissertation carried out as part of the project „InterDok – Interdisciplinary Doctoral Studies Projects at Wroclaw University of Science and Technology" (POWR.03.02.00-00-I003/16) is an interdisciplinary analysis of the assumed research problem and refers to both the discipline of **mechanical engineering** (leading discipline) and to the discipline of **materials engineering** (additional discipline). For this purpose, supervisors representing both scientific disciplines were also appointed:

- **Dr hab. inż. Tomasz Kurzynowski** – mechanical engineering,
  Wroclaw University of Science and Technology,
  Faculty of Mechanical Engineering,
  Department of Laser Technologies, Automation and Production Organization

- **Prof. Dr.-Ing. habil. Markus Bambach** – materials engineering/mechanical engineering,
  Swiss Federal Institute of Technology Zurich,
  Department of Mechanical and Process Engineering

The doctoral thesis was carried out in the leading discipline of mechanical engineering. It contains elements that prove a direct affiliation to this discipline, considering the development of the L-PBF process of two Fe-based metallic glasses and assessing the quality of the samples produced. Belonging to the discipline of materials engineering refers primarily to the applied research techniques used for the structural characterization of the produced samples (light microscopy, scanning and electron microscopy, X-ray diffraction).

Contents

Streszczenie

Temat: Technologia laserowej mikrometalurgii proszków jako alternatywna metoda wytwarzania szkieł metalicznych

W ostatnich latach szczególną uwagę poświęca się technologiom przyrostowym, do których zaliczana jest technologia laserowej mikrometalurgii proszków (L-PBF, ang. Laser Powder Bed Fusion). W technologii tej z powodzeniem wytwarzane są części maszyn z materiałów komercyjnych, znajdując zastosowanie w różnych gałęziach przemysłu. Blisko dekadę temu zapoczątkowano wytwarzanie szkieł metalicznych w technologii L-PBF, które dotychczas możliwe było jedynie z wykorzystaniem specyficznych metod, opracowanych dla tego typu materiałów. Do głównych technik konwencjonalnych wytwarzania szkieł metalicznych zaliczane są: metoda wirującego bębna (ang. melt-spinning method) oraz odlewanie do form miedzianych (ang. copper mold casting).

Kluczowym dla otrzymywania szkieł metalicznych jest uzyskiwanie wysokich przechłodzeń fazy ciekłej. Krytyczna szybkość chłodzenia, umożliwiająca powstanie struktury amorficznej, jest wartością zmienną i zależy od składu chemicznego wytwarzanego stopu. W technologii melt-spinning wytwarzane są taśmy o grubości około 20 μm, osiągając szybkości chłodzenia rzędu 10^4-10^6 K/s. Metoda ta stosowana jest głównie dla szkieł metalicznych o niskiej zdolności do zeszklenia (ang. glass-forming ability, GFA), przez wzgląd na uzyskiwane wyższe od krytycznych szybkości chłodzenia, umożliwiające tworzenie się struktury amorficznej. Termin „zdolność do zeszklenia" odnosi się do podatności stopu do tworzenia w trakcie chłodzenia z fazy ciekłej struktury amorficznej. Miarą zdolności do zeszklenia są szybkość chłodzenia oraz minimalny wymiar przekroju elementu dla którego otrzymana została jedynie struktura amorficzna. Wartościami zdolności do zeszklenia są zatem grubość taśm wytwarzanych w metodzie melt-spinning oraz grubość płytek lub średnica prętów otrzymywanych w technice odlewania do form miedzianych. W metodzie odlewania do form miedzianych wytwarzane są zazwyczaj pręty o średnicy powyżej 1 mm, osiągając szybkości chłodzenia nie przekraczające 10^3 K/s. Stopy wytwarzane w tej technologii posiadają wysoką zdolność do zeszklenia i nazywane są masywnymi

szkłami metalicznymi (ang. bulk metallic glass, BMG). Dotychczas dla szkieł metalicznych na bazie żelaza wytworzony został pręt o średnicy krytycznej 18 mm. W technologii laserowej mikrometalurgii proszków uzyskiwane są szybkości chłodzenia rzędu 10^3-10^8 K/s, które determinowane są wielkością ciekłego jeziorka, zależnego od dostarczonej mocy lasera oraz szybkości skanowania. Uzyskiwany w technologii L-PBF szeroki zakres szybkości chłodzenia umożliwia wytwarzanie szkieł metalicznych, co w połączeniu z dowolnością kształtu wytwarzanych elementów w tej metodzie, wynikającą z warstwowego charakteru procesu, stanowi przewagę nad technikami konwencjonalnymi, preferowanymi dla tej grupy materiałów.

Głównym celem niniejszej rozprawy doktorskiej jest ocena możliwości wytwarzania metodą L-PBF dwóch gatunków szkieł metalicznych na bazie żelaza o różnej zdolności do zeszklenia oraz określenie wpływu wybranych parametrów procesu L-PBF na mikrostrukturę, skłonność do powstawania defektów oraz twardość. W wyniku przeprowadzonej analizy literatury wybrano dwa stopy różniące się składem chemicznym. Stop $Fe_{79}Zr_6Si_{14}Cu_1$, o niskiej zdolności do uzyskiwania struktury amorficznej, wytwarzany dotychczas w postaci cienkich taśm, charakteryzuje się właściwościami cechującymi materiały magnetycznie miękkie. Stosowany jest na rdzenie induktorów, aktuatory liniowe oraz sensory. Z kolei stop $Fe_{45}Cr_{15}Mo_{14}C_{15}B_6Y_2Ni_3$ osiąga wysoki poziom własności wytrzymałościowych i twardości. Z powodu znacznie wyższej zdolności do tworzenia struktury amorficznej stop ten umożliwia wytwarzanie prętów o średnicy 3 mm w technologiach konwencjonalnych.

W pracy przedstawiono metodę doboru parametrów procesu L-PBF dla obydwu gatunków szkieł metalicznych według kryterium minimalizacji defektów. Wytworzone próbki stopów poddano badaniom mikrostruktury z wykorzystaniem mikroskopii świetlnej (LM), skaningowej mikroskopii elektronowej (SEM), transmisyjnej mikroskopii elektronowej (TEM) oraz strukturalnej dyfrakcji rentgenowskiej (XRD). Badania te pozwoliły na identyfikację występujących faz oraz defektów w postaci porów i pęknięć.

W strukturze stopu $Fe_{79}Zr_6Si_{14}Cu_1$ wytworzonego w procesie L-PBF stwierdzono występowanie faz krystalicznych, głównie roztworu stałego α-Fe(Si)

oraz fazy międzymetalicznej $Fe_{23}Zr_6$. Ponadto, zaobserwowano wzrost udziału fazy $Fe_{23}Zr_6$ w miarę wzrostu objętościowej gęstości energii lasera wskutek wzrostu mocy lasera. Przeprowadzone badania TEM natomiast wykazały występowanie struktury amorficznej w charakterystycznej strefie przy linii wtopienia ściegów. W strefie tej, w osnowie fazy amorficznej zidentyfikowano nanometryczne wydzielenia fazy α-Fe(Si). W wytworzonych próbkach zaobserwowano dwa rodzaje porowatości – technologiczną i metalurgiczną. Porowatość technologiczna charakteryzowała się rozbudowanym kształtem i występowaniem cząstek proszku wewnątrz porów, co spowodowane było niedostatecznym przetopieniem warstwy proszku oraz poprzednich warstw na skutek zbyt niskich wartości dostarczonej energii wiązki lasera. Tego rodzaju porowatość została wyeliminowana poprzez zwiększenie objętościowej gęstości energii poprzez wzrost mocy lasera i zmniejszenie prędkości skanowania. Porowatość metalurgiczną charakteryzowały sferyczne pory gazowe, których udział nie przekraczał 1%. Obecność, indukowanych podczas procesu naprężeń własnych, ujawniła się pojawieniem mikropęknięć po upływie trzech tygodni od chwili zakończenia procesu wytwarzania próbek. Charakter pęknięć wskazywał na pękanie na zimno i był związany z naprężeniami cieplnymi powstałymi w trakcie procesu wskutek objętościowego skurczu oraz liniowej rozszerzalności cieplnej.

W przypadku drugiego stopu $Fe_{45}Cr_{15}Mo_{14}C_{15}B_6Y_2Ni_3$ wytworzonego metodą L-PBF możliwe było wytworzenie struktury amorficznej w szerokim zakresie mocy lasera (80-160 W). Przy niskich mocach lasera, w zakresie 80-120 W, oraz prędkościach skanowania, w zakresie 333-500 mm/s, otrzymano strukturę amorficzną o porowatości w przedziale od 2,78% do 8,55%. Wzrost mocy lasera do 160 W i 180 W oraz wzrost prędkości skanowania do 700-1000 mm/s, spowodował obniżenie porowatości do 1,26%. Wartościami granicznymi mocy lasera oraz prędkości skanowania, dla których otrzymano strukturę całkowicie amorficzną, były odpowiednio 160 W i 1000 mm/s. Dalsze zwiększanie mocy oraz obniżanie prędkości skanowania powodowało krystalizację fazy $(Fe,Cr)_{23}(C,B)_6$. Głównym rodzajem porowatości występującym w tym gatunku materiału była porowatość gazowa. Ponadto, podczas procesu L-PBF powstawały mikropęknięcia na gorąco, które propagowały w kierunku zgodnym z kierunkiem przetapiania

ściegów. Charakter pęknięć wskazywał na pęknięcia likwacyjne związane z lokalnym nadtopieniem oraz naprężeniami cieplnymi powstałymi w trakcie procesu.

Dla obydwu stopów wytworzonych w technologii L-PBF przeprowadzono pomiary twardości. Dla stopu $Fe_{79}Zr_6Si_{14}Cu_1$ osiągnięto najwyższą twardość na poziomie 953 HV1 dla mocy lasera 120 W oraz szybkości skanowania 900 mm/s. W przypadku stopu $Fe_{45}Cr_{15}Mo_{14}C_{15}B_6Y_2Ni_3$ dla niskich mocy lasera (80-120 W) i niskich prędkości skanowania (333-500 mm/s) wytworzone próbki charakteryzowały się twardością na poziomie 1105-1196 HV1. Z kolei próbki wytworzone z mocami lasera 160 i 180 W posiadały twardość na poziomie 1141-1196 HV1, a ponowne przetopienie powodowało wzrost twardości osiągając maksymalną wartość 1279 HV1.

Na podstawie przeprowadzonych badań i uzyskanych wyników sformułowano wnioski dotyczące podatności szkieł metalicznych na bazie żelaza na przetwarzanie w technologii laserowej mikrometalurgii proszków. Stwierdzono, że zdolność do zeszklenia odgrywa kluczową rolę w otrzymywaniu struktury amorficznej. W przypadku stopów o niskiej zdolności do zeszklenia przetwarzanych w technologii L-PBF dochodzi do częściowej krystalizacji, przez wzgląd na osiągane szybkości chłodzenia niższe od krytycznej szybkości chłodzenia, gwarantującej utworzenie struktury amorficznej. Z kolei stopy o wysokiej zdolności do zeszklenia w szerokich zakresach mocy lasera i szybkości skanowania umożliwiają otrzymywanie struktury amorficznej. Zarówno w przypadku stopu o niskiej, jak i wysokiej zdolności do zeszklenia wzrost mocy lasera i obniżenie szybkości skanowania prowadzi do redukcji porowatości, będącej jednym z kryteriów stosowalności materiału w technologii L-PBF. Wytwarzanie szkieł metalicznych w metodzie laserowej mikrometalurgii proszków stanowi duże wyzwanie technologiczne przez wzgląd na ich niską plastyczność. Podczas przetwarzania dochodzi do powstawania naprężeń cieplnych, które prowadzą do powstawania mikropęknięć. W pracy potwierdzono możliwość otrzymywania struktur amorficznych dla szkieł metalicznych w technologii L-PBF. Nie mniej jednak dalszy kierunek badań powinien obejmować zagadnienia redukcji mikropęknięć, poprzez zastosowanie podgrzewania platformy roboczej lub selektywnego

podgrzewania dodatkową wiązką lasera oraz przeprowadzoną poprocesową obróbką cieplną.

Abstract

In recent years, special attention has been paid to additive manufacturing, which include the laser powder bed fusion method (L-PBF). This technology successfully produces machine parts from commercial materials used in various industries. Almost a decade ago, the production of metallic glasses in the L-PBF technology was initiated, which until now was possible only with the use of specific methods developed for this type of materials. The main conventional techniques for producing metallic glasses include – the melt-spinning method and copper mold casting.

The key to obtaining metallic glasses is achieving a high cooling rate by cooling from the melt. The critical cooling rate, enabling the formation of an amorphous structure, is a variable value and depends on the chemical composition of the alloy. The melt-spinning technology produces ribbons with a thickness of about 20 μm, achieving cooling rates of 10^4-10^6 K/s. This method is mainly used for metallic glasses with a low glass-forming ability (GFA) due to the higher than critical cooling rates obtained, enabling the formation of an amorphous structure. The term "glass-forming ability" refers to the ability of an alloy to form an amorphous structure from the liquid phase upon cooling. The measure of the glass-forming ability is usually the cooling rate or the minimum cross-sectional dimension of the element for which only the amorphous structure was obtained. Therefore, the values of the GFA are the thickness of the ribbons produced in the melt-spinning method and the thickness of the plates or the diameter of the rods obtained by casting into copper molds. In the copper mold casting method, rods of more than 1 mm diameter are usually produced, achieving cooling rates not exceeding 10^3 K/s. Alloys this technology produces have the high glass-forming ability and are called bulk metallic glass (BMG). So far, a rod with a critical diameter of 18 mm has been produced for iron-based metallic glasses. In the laser powder bed fusion technology, cooling rates of 10^3-10^8 K/s are obtained, which are determined by the size of the melt pool, depending on the supplied laser power and scanning speed. The wide range of cooling rates obtained in the L-PBF technology enables the production of metallic glasses, which, combined with the freedom of shape of the parts produced in this method, resulting from the layered nature of

the process, is an advantage over conventional techniques, preferred for this group of materials.

The main aim of this doctoral dissertation is to determine the processability of two iron-based metallic glasses with different glass-forming abilities in the laser powder bed fusion technology and to determine the effect of selected L-PBF process parameters on the microstructure, defects formation and hardness. As a result of the literature analysis, two alloys with different chemical compositions were selected. The $Fe_{79}Zr_6Si_{14}Cu_1$ alloy, with a low glass-forming ability, so far produced in the form of ribbons, is characterized by properties characteristic of soft magnetic materials. It is used for inductor cores, linear actuators and sensors. In turn, the $Fe_{45}Cr_{15}Mo_{14}C_{15}B_6Y_2Ni_3$ alloy achieves high strength properties and hardness. Due to its much higher ability to form an amorphous structure, this alloy allows the production of rods with a diameter of 3 mm using conventional technologies.

The thesis presents a method of selecting the parameters of the L-PBF process for both types of metallic glasses according to the defect minimization criterion. The produced alloy samples were subjected to microstructure studies using light microscopy (LM), scanning electron microscopy (SEM), transmission electron microscopy (TEM) and X-ray diffraction (XRD). These tests allowed the identification of the remaining phases and defects in the form of pores and cracks.

In the microstructure of the $Fe_{79}Zr_6Si_{14}Cu_1$ alloy produced in the L-PBF process, crystalline phases were found, mainly the α-Fe(Si) solid solution and the $Fe_{23}Zr_6$ intermetallic phase. In addition, an increase in the proportion of the $Fe_{23}Zr_6$ phase was observed as the volumetric laser energy density increased due to the increase in laser power. The TEM tests, however, showed the presence of an amorphous structure in the characteristic zone near the beads fusion line. In this zone, in the amorphous phase matrix, a nanometric α-Fe(Si) solid solution precipitations were identified. Two porosity types were observed in the produced samples – technological and metallurgical. The technological porosity was characterized by an extensive shape and the presence of powder particles inside the pores, which was caused by insufficient melting of the powder layer and previous layers due to too low values of the supplied laser beam energy. This kind

of porosity was eliminated by increasing the volumetric energy density by increasing the laser power and reducing the scanning speed. The metallurgical porosity was characterized by spherical gas pores, the share of which did not exceed 1%. The presence of residual stresses induced during the process was revealed by the appearance of microcracks three weeks after the end of the sample production process. The nature of the cracks was indicative of cold cracking and was related to thermal stresses generated during the process due to volumetric shrinkage and linear thermal expansion.

In the case of the second $Fe_{45}Cr_{15}Mo_{14}C_{15}B_6Y_2Ni_3$ alloy, produced by the L-PBF method, it was possible to produce an amorphous structure in a wide range of laser power (80-160 W). At low laser powers, 80-120 W range, and 333-500 mm/s scanning speeds, an amorphous structure with porosity ranging from 2.78% to 8.55% was obtained. The increase in laser power to 160 W and 180 W and the increase in the scanning speed to 700-1000 mm/s resulted in a decrease in porosity, reaching a minimum of 1.26%. The limit values of laser power and scanning speed, for which a fully amorphous structure was obtained, were 160 W and 1000 mm/s, respectively. Further increasing the power and lowering the scanning speed resulted in the crystallization of the $(Fe, Cr)_{23}(C, B)_6$ phase. The primary type of porosity occurring in this type of material was gaseous porosity. In addition, during the L-PBF process, hot microcracks were formed, which propagated in the direction of the bead formation. The nature of the cracks indicated liquation cracks associated with local melting and thermal stresses created during the process.

Hardness measurements were carried out for both alloys produced in the L-PBF technology. For the $Fe_{79}Zr_6Si_{14}Cu_1$ alloy, the highest hardness (953 HV1) was achieved for the laser power of 120 W and the scanning speed of 900 mm/s. Regarding the $Fe_{45}Cr_{15}Mo_{14}C_{15}B_6Y_2Ni_3$ alloy, the produced samples were for low laser power (80-120 W) and low scanning speed (333-500 mm/s) characterized by hardness of 1105-1196 HV1. In turn, the samples produced with laser powers of 160 and 180 W had a hardness of 1141-1196 HV1, and re-melting increased the hardness, reaching a maximum value of 1279 HV1.

Based on the conducted research and the obtained results, conclusions were formulated regarding the processability of iron-based metallic glasses in laser powder bed fusion technology. The glass-forming ability was found to be crucial in obtaining the amorphous structure. In the case of alloys with a low GFA processed in the L-PBF technology, partial crystallization occurs due to the achieved cooling rates lower than the critical cooling rate that guarantees the formation of an amorphous structure. On the other hand, alloys with high glass-forming ability in a wide range of laser power and scanning speed allow for achieving an amorphous structure. Both in the case of the alloy with low and high GFA, the increase in laser power and the reduction in the scanning speed lead to a reduction in porosity, which is one of the criteria for the material's applicability in the L-PBF technology. Manufacturing metallic glasses in laser powder bed fusion technology is a significant technological challenge due to their low plasticity in ambient temperature. During processing, thermal stresses occur, leading to micro-cracks formation. The dissertation confirmed the possibility of obtaining amorphous structures for metallic glasses in the L-PBF technology. Nevertheless, to reduce or eliminate cracks, it is necessary to undertake further research on the reduction of thermal stresses by heating the built plate or selective heating with an additional laser beam and post-processing heat treatment.

1. Introduction

Most likely, every person working with materials has come across the words that "microstructure determines the properties". One of the major paradigms of materials science successfully explains and predicts the behavior of conventional alloys. This is a direct result of the microstructural features that have been sufficiently known so far. In polycrystalline materials, we are able to easily and routinely identify them using a microscope and make modifications by appropriate alloy treatment. Occurring main phases, second phases precipitation, grain size, twin boundaries, or various types of stacking faults. All of these and many more are microstructure features that control the properties of crystalline alloys. However, what if an alloy lacks characteristic or imperceptible microstructure features? Metallic glasses, because that is what we are talking about, under a light microscope, each type of amorphous alloy looks the same, similarly with a scanning or transmission electron microscope. Always slightly blurred at high magnifications. Both on electron diffractions and X-ray diffractions, a characteristic halo effect. What about properties then? They are different. Even sometimes for the same metallic glass but with a different manufacturing history. Still amorphous but with other excellent properties. The absence of dislocations guarantees high mechanical strength, the absence of grain boundaries ensures a low corrosion rate, the absence of domain barriers that are blocked by dislocations and grain boundaries results in low magnetic coercivity, and the absence of long atomic arrangements ensures high electrical resistance.

So why have metallic glasses not replaced conventional alloys yet? In order to answer this question, it is first necessary to describe the manufacturing possibilities. In the production of metallic glass, the alloy is heated up to a liquid phase and then cooled down very rapidly, often at a cooling rate of more than 10^6 K/s. Conventional technologies in which metallic glasses are manufactured allow the production of thin ribbons, coatings, plates, or rods. To date, an 18 mm diameter rod has been successfully fabricated using iron-based metallic glass, which directly determines the limited industrial use of this type of materials.

Nevertheless, the rapid development of additive manufacturing in recent years allows for increasing the applicability of metallic glasses. Laser powder bed fusion

technology, in which metallic powder is selectively melted layer by layer with a laser beam, theoretically allows the production of larger and more complex products using amorphous alloys than in conventional technologies. This is because the laser spot, measuring several tens of micrometers, melts the material, creating a small melt-pool, which allows fast cooling due to its size.

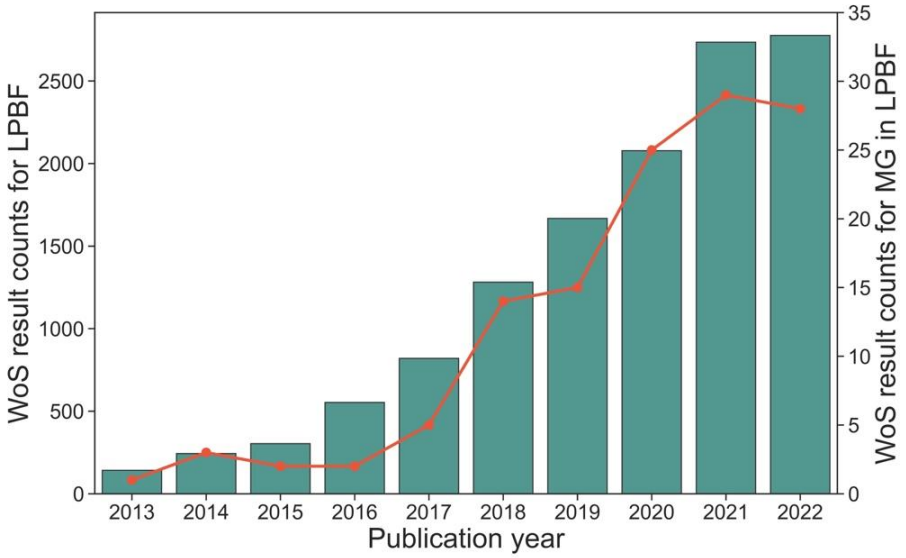

Fig. 1.1. *Yearly publications number for laser powder bed fusion (mint) and metallic glasses produced in L-PBF technology (orange)*

Laser powder bed fusion technology, both for conventional materials and metallic glasses, is currently playing a significant role. Its continuous development and trends can be observed, for example, in the number of publications released in recent years, which presents the upper figure (Fig. 1.1). The charts are based on data taken from the Web of Science Core Collection (WsO) database after entering the following phrases:

- for laser powder bed fusion: ((ALL=("selective laser melt*")) OR ALL=("laser powder bed fus*")) OR ALL=("direct metal laser sint*"),
- for metallic glasses manufactured in L-PBF technology: (((ALL=("selective laser melt*")) OR ALL=("laser powder bed fus*")) OR ALL=("direct metal laser sint*")) AND ALL=("metallic glass*").

For almost a decade, metallic glasses in laser powder bed fusion technology have been the subject of research by many scientists. In most works, special attention is paid to the appropriate selection of process parameters that determine

the structure of the manufactured elements. In this doctoral dissertation, the leading subject of the research is to evaluate the possibility of producing two types of iron-based metallic glasses with low and high glass-forming abilities using the laser powder bed fusion method and to determine the effect of selected parameters of the L-PBF process on the microstructure, defect formation, and hardness.

2. State of the art

2.1. Metallic glasses

The origins of metallic glasses date back to the 1960s, when Duwez, Willens and Klement developed a technique to produce thin films with a single-phase structure. In the initial phase, they successfully produced four copper-silver alloys whose phases were called metastable solid solutions [1]. Soon after, they obtained a non-crystalline structure for the $Au_{75}Si_{25}$ (at. %) alloy [2]. The proposed technique, consisting of a very fast cooling rate (>5×10^5 K/s) of a liquid metal drop on the metal surface with high thermal conductivity, has also been used as one of the techniques for preparing samples in transmission electron microscopy. The obtained structures were described in the literature as pseudo-amorphous [3].

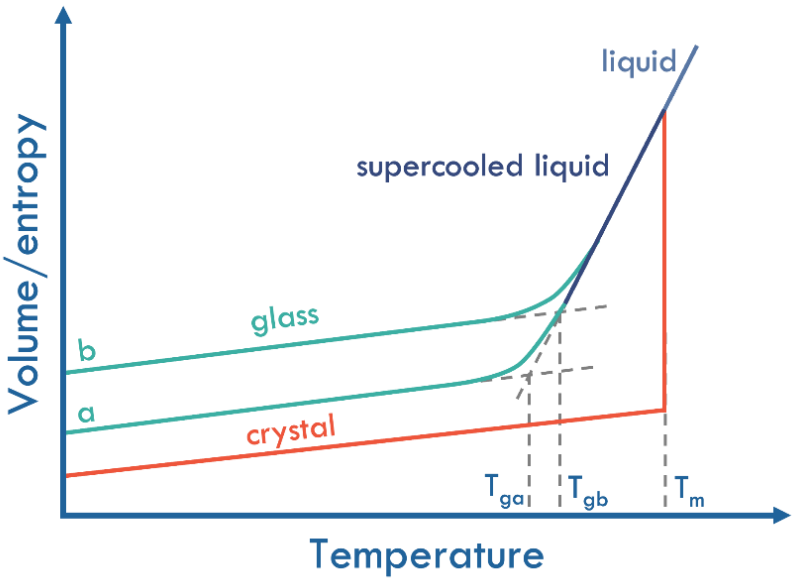

Fig. 2.1. *Schematic volume/entropy change in relation to temperature and cooling rate. T_{ga} and T_{gb} are glass transition temperatures depending on the cooling rate (a<b), and T_m is the melting temperature. Adapted from [4]*

The formation of an amorphous structure in metals can be explained by referring to the volume of the system or its entropy (Fig. 2.1). As the alloy is heated, the volume and entropy increase due to the supplied energy. Upon reaching the melting point, the system will change its state from solid to liquid. As a consequence, the volume and entropy of the system will abruptly increase. Similarly, during slow cooling from the liquid phase, due to the high atomic

packing density of the crystalline phase, there will be a sudden decrease in entropy and volume. In the case of rapid cooling from the liquid phase, there is a gradual supercooling of the liquid, accompanied by an increase in viscosity and a decrease in volume and entropy. Consequently, the movement of atoms is limited, and after reaching the glass-transition temperature, the alloy goes into a glassy state. Schematically described properties changes of the metallic alloy system depending on the temperature are shown in Figure 2.1 [4–7].

Currently, the term "metallic glass" describes metallic alloys whose structure is amorphous. Often, metallic glasses are incorrectly described as statistically disordered at the atomic level. Sheng et al. [8] proved that metallic glasses have a short-to-medium-range ordering of atoms. The nearest-neighbor atoms cause short-range order, while on the length scales further than the nearest neighbor, medium-range order [9]. The use of various sizes of atoms in the alloy is directly conducive to the efficient filling of free spaces, thus affecting the creation of local order. In addition, the nature of metal atoms, which interact through many-body, directly implies the neighborhood choice with the lowest energy, leading to a local order [10]. In the case of conventional alloys with a crystalline structure, the degree of local ordering is very high because almost all atoms occupy designated places, forming a crystal lattice. Only in the case of structure defects, such as grain boundaries, dislocations, and vacancies, a low degree of local ordering occurs in small amounts [11]. A schematic drawing showing the comparison of the degree of local ordering and the structural differences in metallic glasses and crystalline alloys is shown in Fig. 2.2.

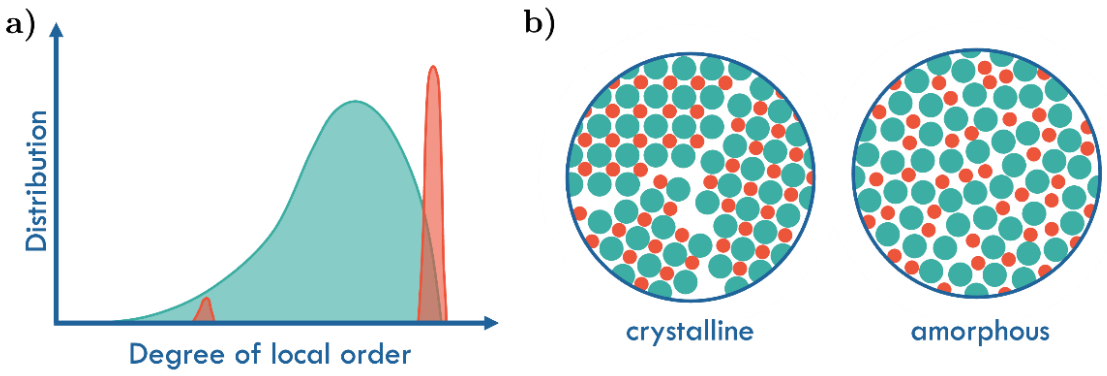

Fig. 2.2. *A schematic: a) distribution of local structures in metallic glasses and crystalline metals (adapted from [10]), b) comparison of crystalline alloy and metallic glass*

Metallic glasses, due to their metastable nature, require high cooling rates by cooling from the liquid phase [12–14]. Consequently, using conventional manufacturing techniques, such as melt-spinning or copper-mold casting, the obtained products are characterized by constrained thickness. Currently, the typical quantities defining the ability of the material to create an amorphous structure (so-called Glass-Forming Ability – GFA) are the critical casting thickness and the critical cooling rate. The produced alloys exceeding one-millimeter critical thickness are named bulk metallic glasses, and their cooling rates are often lower than 10^3 K/s [15]. Typically, the critical cooling rate for iron-based metallic glasses is approximately 10^6 K/s, limiting manufacturing only thin ribbons using conventional techniques [16,17].

Metallic glasses, due to their metastable nature, show limited thermal stability [18,19]. These materials heated to the primary crystallization temperature (T_x) gradually lose their amorphous structure in favor of the crystallizing phase. The degree of crystallinity depends on the temperature and time, which determines the size of the forming phase. Crystallization of metallic glasses mainly occurs as a result of exceeding the activation energy, causing increased diffusion of atoms [20].

Metallic glasses are characterized by glass-transition temperature (T_g). This temperature depends on the alloy composition and the heating/cooling rate [21]. As previously mentioned, metallic glasses cooled from the melt with a high cooling rate congeal after exceeding the glass-transition temperature. This results in the kinetic freezing of atoms with short and medium-range order [21]. On the other hand, an increase in temperature above the glass-transition temperature will cause a gradual increase in the mobility of the atoms without necessarily leading to abrupt crystallization. The value of the glass transition temperature alone may indicate the plasticity or brittleness of the produced metallic glass [22]. The range between the glass-transition temperature and the primary crystallization temperature is called a supercooled liquid region. Heating the alloy in this temperature range leads to relaxation and softening, and therefore the alloy may become highly ductile [23].

The production of metallic glasses in conventional technologies adopted for this group of materials is usually limited to the single-roller melt-spinning method [24,25], splat quenching method [25] and copper mold injection- or suction-casting methods [16]. With the first two methods, thin ribbons are produced. The thickness of the foil depends on the copper wheel velocity [26]. Ribbons with a thickness of 20 μm are most commonly obtained [24,25]. This method enables fast cooling rates in the range of 10^4-10^6 K/s [26]. Thin films are usually made of amorphous alloys with low glass-forming ability. The resulting ribbons are rolled into coils and then annealed at the primary crystallization temperature, depending on the chemical composition of the alloy. In the case of copper mold injection- or suction-casting, rods are produced whose diameter is dictated by the glass-forming ability of the alloy. Most often, tests are carried out for different diameters, thus determining the critical diameter of the rod, for which an amorphous structure will be obtained throughout the entire cross-section [27]. It has been assumed that alloys for which the rod diameter exceeds one millimeter are called bulk metallic glasses. The produced rods can be freely formed in a hot forming process, operating in the supercooled liquid region temperatures [28].

2.2. Iron-based metallic glasses

The first Fe-based metallic glass, belonging to the Fe-P-C group, was produced by Duwez and Lin in 1967 [23]. The developed alloy was characterized by significantly better magnetic properties (high magnetic saturation, low magnetic coercivity, low core loss) compared to conventional silicon steels. The proposed material directly matched the growing demand for high-performance soft magnetic materials. This discovery marked the beginning of an intense period of research into iron-based amorphous alloys. The main alloying elements were P, Si, Co, Mo and B [29–32]. The first metallic glasses designed for commercial use were developed. They were alloys from the Fe-Co-P-B and Fe-Co-Si-B groups called METGLAS [33]. Then, the group of commercial alloys was joined by the FINEMET alloy (Fe-Si-B group with the addition of Cu and Nb), invented by Yoshizawa et al. [34]. After annealing, this alloy was characterized by a very fine structure, significantly improving its magnetic properties. However,

the amorphous matrix had a low Curie temperature, which limited the use of this alloy. The alloy developed for operation at high temperatures was the nanocrystalline HITPERM alloy (group (Fe, Co)-M-B-Cu (M = Nb, Hf, Zr)) [35]. A breakthrough in metallic iron-based glasses was the production of rods with a diameter of 1 mm using $Fe_{73}Al_5Ga_2P_{11}C_5B_4$ alloy [36]. This started the period of iron-based bulk metallic glasses for which ever-larger critical diameters of produced rods were obtained [37–39]. The use of rare-earth elements in metallic glasses, such as erbium and yttrium, exceeded 10 mm in diameter of the produced rods [40,41]. So far, the rod with the largest diameter, 18 mm, for iron-based metallic glasses was made of the alloy $(Fe_{0.8}Co_{0.2})_{47}Cr_{15}Mo_{14}C_{15}B_{15}Tm_3$ and developed by A. Inoue [42].

The metallic glasses' nature, manifested by the lack of typical defects found in crystalline alloys, which include the already mentioned dislocations, grain boundaries or precipitates, leads to several favorable mechanical properties. High strength and hardness, low Young's modulus, high elastic strain and super-plasticity were obtained in the supercooled liquid region temperature range [43]. Figure 2.3 compares the selected mechanical properties of iron-based metallic glasses to other amorphous and conventional alloys [15]. Typically, metallic glasses exhibit higher strengths and hardness while maintaining lower Young's modulus values compared to conventional crystalline counterparts. Particularly noteworthy are Fe-based metallic glasses, for which 3-4 times higher strength and hardness values were achieved with a similar Young's modulus to high-performance steels. More broadly, the selected mechanical properties of iron-based metallic glasses are presented in Table 2.1.

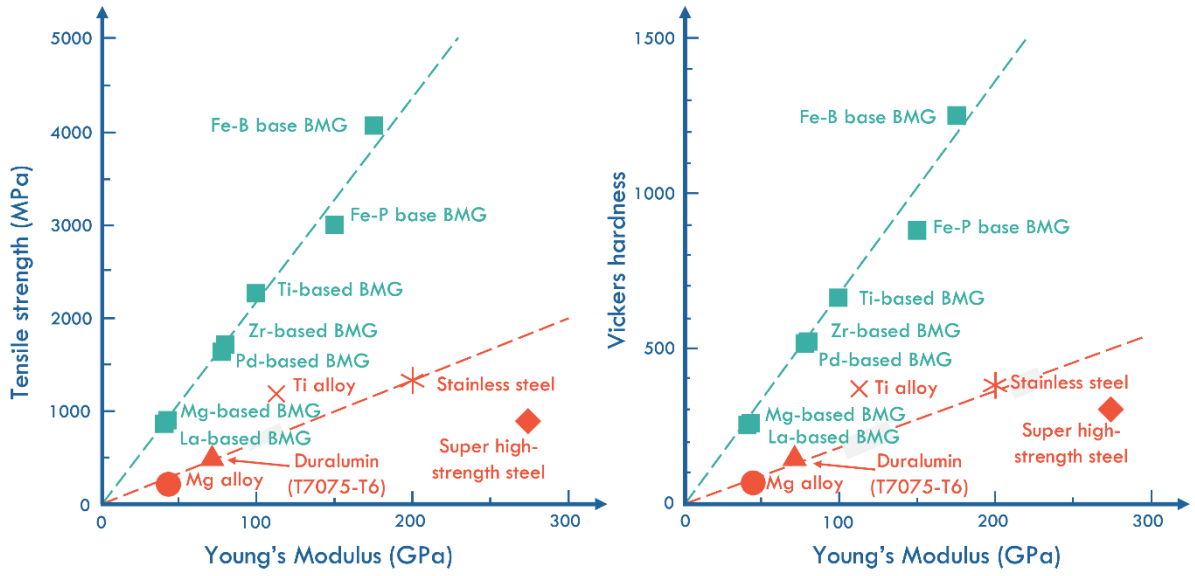

Fig. 2.3. *Comparison of tensile strength, Vickers hardness and Young's modulus for some metallic glasses and conventional alloys. Adapted from [15]*

In addition to high mechanical properties, many iron-based metallic glasses have excellent magnetic properties. These alloys are referred to as soft magnetic alloys, and their properties are usually due to their high iron content. Alloys from this group usually have a lower glass-forming ability and are obtained as thin ribbons. Due to high magnetic saturation (>1.3 T), low coercive force (<3.3 A/m) and low core losses [44], these alloys are used in electrical and electronic areas as inductor cores [45], sensors [46] or linear actuators [47].

Tab. 2.1. *Selected mechanical properties of iron-based metallic glasses developed since 2010 to date*

Alloy composition	σ_y (MPa)	σ_f (MPa)	ε_p (%)	E (GPa)	HV	D_c (mm)	Publ. year	Ref.
$(Fe_{0.8}Ni_{0.2})_{71}Mo_5P_{12}C_{10}B_2$	2400	3100	5.2	174	–	3	2010	[48]
$(Fe_{0.76}Si_{0.096}B_{0.084}P_{0.06})_{99.9}Cu_{0.1}$	3250	3300	3.1	–	–	2.5	2010	[49]
$Fe_{35.5}Ni_{35.5}Nb_6B_{23}$	3694	3888	4.2	–	–	1	2010	[50]
$Fe_{77}Mo_5P_9C_{7.5}B_{1.5}$	2200	4300	30.6	–	–	1	2010	[51]
$Fe_{73}C_7Si_{3.3}P_{8.7}B_5Mo_3$	–	3800	0.43	–	–	5	2011	[52]
$(Fe_{71}Nb_6B_{23})_{99.5}Cu_{0.5}$	3755	3902	4.3	–	–	1	2011	[53]
$Fe_{71}Mo_2Nb_3P_{12}C_{10}B_2$	2800	4000	1	–	–	1	2011	[54]
$Fe_{52}Co17.5B_{20}Si_4Nb_4V_{2.5}$	4200	4700	6.3	–	–	1	2012	[55]
$Fe_{79}Si_6B_{10}P_5$	3200	–	1.1	–	–	1.5	2012	[56]

Alloy composition	σ_y (MPa)	σ_f (MPa)	ε_p (%)	E (GPa)	HV	D_c (mm)	Publ. year	Ref.
$(Fe_{0.9}Ni_{0.1})_{77}Mo_5P_9C_{7.5}B_{1.5}$	2940	3260	8.1	–	–	1	2013	[57]
$(Fe_{0.335}Co_{0.335}Nb_{0.06}B_{0.27})_{99.9}Cu_{0.1}$	4830	4890	3.7	–	1220	1	2013	[58]
$(Fe_{0.335}Co_{0.335}Nb_{0.06}B_{0.27})_{99.8}Cu_{0.2}$	4900	4930	2.4	–	1230	1	2013	[58]
$Fe_{82}Mo_1P_{6.5}C_{5.5}B_2Si_3$	3267	–	1.3	–	–	1	2013	[45]
$Fe_{62}Ni_{18}P_{13}C_7$	2400	3000	50	–	–	1	2014	[59]
$[(Fe_{0.5}Co_{0.5})_{0.75}Si_{0.05}B_{0.20}]_{96}Nb_4$	–	4143	–	–	–	2	2014	[60]
$Fe_{50}Ni_{30}P_{13}C_7$	2250	–	22	–	–	1	2014	[61]
$Fe_{77}Al_3P_9C_9B_2$	–	3000	5	–	–	3	2015	[62]
$(Fe_{75}Mo_5P_{13}C_7)99.5B0.5$	2250	–	2.4	–	–	1.5	2016	[63]
$(Fe_{77}Mo_5P_9C_{7.5}B_{1.5})_{99.9}Cu_{0.1}$	–	3100	6.6	–	–	1.5	2017	[64]
$Fe_{70}Ni_{10}P_{13}C_7$	2690	–	50	–	–	1	2017	[65]
$Fe_{60}Ni_{20}P_{13}C_7$	2450	–	50	–	–	1	2017	[65]
$Fe_{43}Cr_{20}Mo_{10}W_4C_{15}B_6Y_2$	–	3990	–	–	1238	8	2018	[66]
$Fe_{50}Ni_{30}P_{13}C_7$	2265	–	26.3	–	–	1	2018	[43]
$Fe_{66.7}Co_5B_{16.7}Si_{8.3}Zr_{3.3}$	–	–	–	191	–	2.5	2018	[67]
$Fe_{62.5}Co_{10}B_{16.7}Si_{8.3}Hf_{2.5}$	–	–	–	212	–	2.5	2018	[67]
$Fe_{56}Ni_{20}Mo_4P_{12}C_4B_4$	2680	–	5.9	–	–	1.5	2019	[68]
$Fe_{56}Ni_{20}Mo_4P_{11}C_4B_4Si_1$	2780	–	7	–	–	2	2019	[68]
$Fe_{66}Er_5Nb_6B_{23}$	–	3320	–	–	1040	4	2019	[69]
$Fe_{66}Dy_5Nb_6B_{23}$	–	3650	–	–	1060	2	2019	[69]
$Fe_{66}Tm_5Nb_6B_{23}$	–	3150	–	–	1020	4.5	2019	[69]
$Fe_{79}B_{16}Mn_4Cu_1$	–	3228	–	–	754	3	2020	[70]
$Fe_{79}B_{20}Cu_1$	–	3908	–	–	1148	3	2020	[70]
$Fe_{74}Mo_6P_{13}C_7$	3100		25	173	–	1	2021	[71]
$Fe_{59}W_{23}B_{18}$	–	–	–	–	1381	1	2021	[72]
$Fe_{57}Cr_{10}Zr_8B_{18}Mo_5Nb_2$	–	1950	–	–	1310	3	2021	[73]
$Fe_{57}Cr_{10}Zr_8B_{18}Mo_4Nb_3$	–	2062	–	–	1180	3	2021	[73]
$Fe_{39}Ni_{39}B_{12.82}Si_{2.75}Nb_{2.3}P_{4.13}$	3074	–	10.7	–	–	1	2021	[74]
$Fe_{68}Ni_{12}P_{12}B_{4.9}Si_{2.5}Cu_{0.6}$	2722	2928	6	–	–	1	2022	[75]
$Fe_{71}Ni_9P_{12}B_{4.9}Si_{2.5}Cu_{0.6}$	2896	2979	5.1	–	–	1	2022	[75]

Considering the mechanical properties of iron-based metallic glasses, such as high strength and hardness, and the current production possibilities allowing to

obtain elements of limited shape and size, micro gears are manufactured [76]. The possibility of hot forming of metallic glass prefabricates is possible due to the viscous flow in the supercooled liquid region, which enables the easy production of small mechanical components.

Most iron-based metallic glasses have high corrosion resistance and high wear resistance. For this reason, these materials are often used for coatings obtained by spraying technologies [77–79].

2.3. Laser powder bed fusion technology

The laser powder bed fusion technology is classified as a powder additive manufacturing technique [80]. This technology uses a laser beam to melt the powder layer, and the generative character results from layer-by-layer fabrication [81]. Even with complex geometries, the manufactured parts are often characterized by mechanical properties similar to, or sometimes even better, than those manufactured using conventional techniques [82,83]. Due to a fully melted metal powder by high-power-density laser, the density of fabricated products is compared to near theoretical densities [84]. Due to the mechanical properties obtained and the possibilities of topological optimization of the manufactured parts, there is an increased demand for the L-PBF process use in critical industries, such as automotive, biomedical, aerospace, electronics and other advanced technologies [85–87]. Nevertheless, due to the nature of the process and incorrect parameter selection, undesirable defects may be introduced [88].

The laser powder bed fusion device is schematically presented in Fig. 2.4. The most important in laser powder bed fusion is a laser with sufficiently high power, which melts the applied powder layer entirely, and a scanning system enabling programmed laser beam guidance. The process advances automatically and computer controlled based on the developed CAD model, which contains basic information about the location of the laser beam and the given process parameters. Due to its layered nature, the technological process is divided into separate layers. First, the right amount of powder is delivered from the powder delivery system, which will be evenly distributed to the set layer thickness over the entire surface through a leveling system (re-coater, wiper, roller). The powder layer is melted

with a laser beam along the previously programmed path. Then the build platform moves down by the set layer thickness, the leveling system moves to the starting position, a portion of powder is delivered, and the further cycle of the process is repeated until the last layer is melted. The L-PBF device chamber is equipped with a shield gas supply system to prevent oxidation during the entire process.

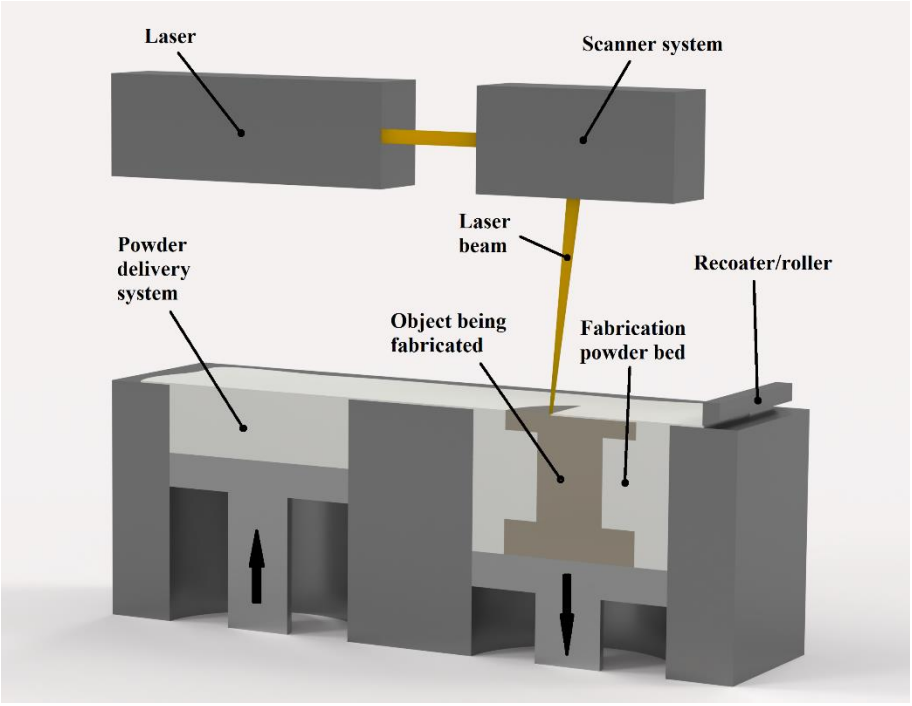

Fig. 2.4. *A simplified diagram of laser powder bed fusion technology. Adapted from [89–91]*

The melting of the powder layer using a laser follows a scanning strategy that traces paths to single beads (Fig. 2.5). The beads produced should overlap, thus leading to partial melting of the previous bead and the previously formed layer. In order to ensure proper bead formation, appropriate main process parameters are established, which include: laser power P (50-450 W), scanning speed v (100-2500 mm/s), hatch distance s (30-350 μm), layer thickness t (20-200 μm) and laser spot size d (50-200 μm) [94]. Appropriate selection of parameters allows the creation of a relatively small melt pool, which mainly enables rapid heat dissipation. In L-PBF technology, solidification occurs relatively quickly, and with a proper selection of the building platform, it is possible to achieve a cooling rate of up to 10^3 - 10^8 K/s [95].

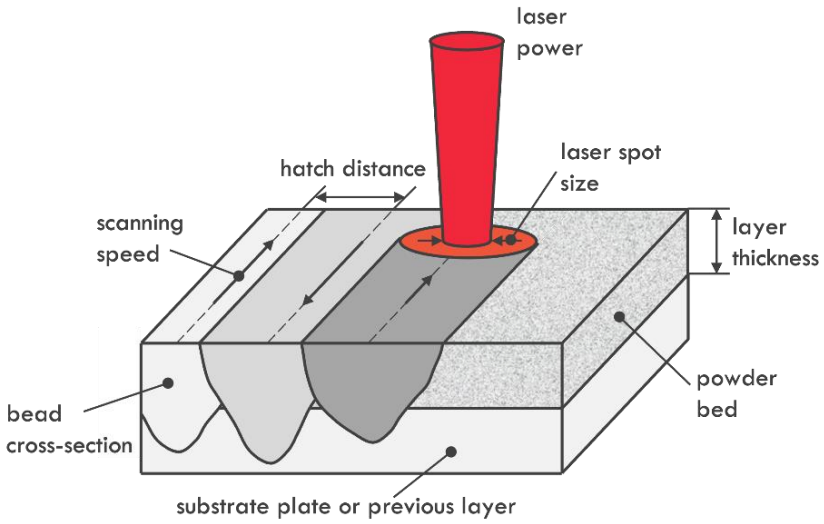

Fig. 2.5. *Schematic illustration of the L-PBF bead formation and the main process parameters. Based on [92,93]*

Often, the above-mentioned process parameters are reduced to a single value, the laser volumetric energy density (Eq. 2.1). It has been assumed that the energy density values, which are components of various process parameters, affect the relative density of the manufactured parts [96]. In the case of low values, only partial melting of the powder was observed, affecting the low shares of the liquid phase, which led to an increase in the viscosity of the melt pool, limiting its flowability, causing the formation of a non-homogenous bead, and consequently affecting a low relative density of the fabricated parts [97]. On the other hand, too high volumetric energy density can cause poor surface quality, balling effect and a decrease in relative density [98].

$$E_d = \frac{P}{vst} \qquad \text{(Eq. 2.1)}$$

Nevertheless, the laser energy density itself should not be an indicator of the properties characterizing the manufactured elements. According to [99], the ratios of scanning speed, layer thickness or hatch distance to laser power are more reliable. It is possible to achieve high relative densities for both low and high-energy densities. With the same laser energy densities and increasing laser powers, regardless of the variability of other parameters, the relative density increases. Therefore, it is believed that using higher laser power results in obtaining samples with lower pore content [99].

Besides the laser power, a similarly important parameter is the scanning speed, which affects the laser energy transfer time. At low scanning speeds, the laser beam's exposure time increases, leading to an increase in delivered energy [100]. Due to this, higher relative densities are observed at constant laser powers and decreasing scanning speeds [101]. It can be explained by the increased interaction time of the laser beam that causes sufficient energy supply to fully melt the powder and obtain a necessary amount of the liquid phase to create a highly dense part [92].

Considering the scanning strategy, choosing the proper hatch distance is crucial. This parameter is partially dependent on the laser power and the scanning speed, which directly impact the size of the melt pool and, consequently, of a single bead. The hatch distance should be chosen so that the beads overlap. If the hatch distance is too large, the formed beads will be too far apart, so neighboring beads will not connect. Therefore, voids will be formed between the beads, affecting the high porosity [102].

The layer thickness should be selected so that it is fully melted and the previously formed layer is at least partially melted. Otherwise, the layers will not create a strong connection, resulting in the appearance of voids between the layers. With increasing layer thickness, an increase in porosity was observed, which is repeated at regular intervals [99].

The selection of process parameters is crucial to fabricate homogeneous and dense elements. Incorrect selection of parameters can lead to the appearance of undesirable defects. The basic defects occurring in the laser powder bed fusion technology are porosity, balling effect, surface roughness, cracks and loss of alloying elements [92].

Different types of porosity can be present in the L-PBF technology. One of them is the fusion porosity, caused by the limited connection between the melted powder layer and the previously formed layer due to the too low energy supply. It is manifested by the lack of local melting and most often occurs between two neighboring layers, causing discontinuity [103]. It is most often triggered by too low laser power, high scanning speed and high layer thicknesses, resulting in low penetration depth. In addition, the appearance of fusion porosity can occur due to

excessive gas entrapment between the powder particles [104]. Fusion pores can be eliminated mainly by improving the process parameters, and guaranteeing full penetration of the powder layer and the previously fabricated layer [105,106]. The fusion porosity is characterized by an irregular shape with unmelted powder particles inside [107].

Another common type of porosity is gas porosity, which is caused by trapped gas between the powder particles, the porosity of the powder itself, and the keyhole effect [92,108]. Gas pores are spherical and usually do not exceed 30 μm in diameter. Gas pores coming from the powder are most often formed due to the limited time of solidification of the melt pool, which makes it impossible to move the pores outside the material being produced. Similarly, in the case of pores formed because of gases contained between the powder particles. The pores formed in the melt pool have no possibility of getting outside them [107]. In the case of gas pores formed due to the keyhole effect, intensive evaporation occurs, and as a result of surface tension and keyhole collapse, the pores are introduced into the solidifying melt pool [108].

The most common types of cracks in laser powder bed fusion technology are cold and hot cracks. For both groups, the sources of cracks are different. Solidification cracking, which is one of the types of hot cracking, occurs during the last phase of melt pool solidification. Thus, the crack appears inside the bead. This process is initiated by the interaction between mechanical and metallurgical factors and is intensified by the occurring temperature gradient [109]. Moreover, the pores present in the material become pre-existing nuclei for the formation of cracks and their propagation [110]. The dendritic morphology is observed for solidification cracks, which suggests the already-mentioned initiation in the last phase of the melt pool solidification [111]. The factors favoring the formation of solidification cracks are a wide solidification temperature region and the micro-segregation of alloying elements [111]. Another form of hot cracking is liquation cracking. In contrast to solidification cracks, these cracks do not show dendritic morphology, and their occurrence area is often reduced to a partially melted zone. Thus, liquation cracks are observed at the bead borders, outside the fusion zone, and their formation results from local melting in the area of both grain boundaries

or other boundaries and thermal stresses. The formation of liquation cracks may be favored by the grains structure, liquation extent, metal shrinkage in the melt region and hot ductility [111]. On the other hand, L-PBF technology may experience cold cracking. They are mainly caused by residual stresses arising from large temperature gradients and high cooling rates [89,112]. Due to the nature of the process, cyclical heating and cooling, reheat cracking may occur. This type of cold cracking is not always observed immediately after the process. The tendency to reheat cracking is often shown by alloys containing alloying elements liable to form carbides and increased precipitation [109].

One of the main drivers of crack formation in the L-PBF process is thermal stress due to heating and cooling cycles, high-temperature differences, and high cooling rates. Cracks can be reduced or eliminated by various types of treatments. It is already possible to optimize the process parameters during the manufacturing process. The use of high laser power and low scanning speeds results in a residual stress increase [113], which may result in the appearance of cracks. In order to reduce temperature gradients and thermal stresses, heating of the working platform and re-melting are successfully used [114]. A properly selected scanning strategy and the use of multiple lasers are also conducive to reducing residual stress [115]. In addition, post-processing is used to reduce stresses and cracking by common treatments, like heat treatment [116,117] and hot isostatic pressing [118,119].

2.4. Iron-based metallic glasses in laser powder bed fusion technology

For the first time, Fe-based metallic glasses were manufactured using L-PBF technology and described by S. Pauly et al. [120] in 2013. In order to carry out the process, the following parameters were used: laser power 320 W, scanning speed 3470 mm/s, hatch distance 124 μm, and layer thickness 50 μm. Cylindrical parts and scaffoldings were obtained using $Fe_{74}Mo_4P_{10}C_{7.5}B_{2.5}Si_2$ alloy. The tests showed that the manufactured elements were structurally similar to the input material. Namely, the X-ray diffraction spectra showed the presence of α-Fe, γ-Fe and $Fe_{23}B_6$ phases, similar to the used powder. A small amount of the crystalline phase characterized the produced parts. However, attention was paid to the quality of

the received scaffoldings, which could be successfully improved by refining the process parameters. Unfortunately, the conducted tests did not include the measurement of porosity or relative density, which is crucial in producing elements in the L-PBF technology.

Work [121] treats the impact of laser powder bed fusion process parameters on the microstructure, thermal stability, and magnetic properties of the $Fe_{68.3}C_{6.9}Si_{2.5}B_{6.7}P_{8.7}Cr_{2.3}Mo_{2.5}Al_{2.1}$ alloy. In order to obtain (cylindrical) samples for testing, the following parameters were used: laser power 280 - 340 W, scanning speed 1500 - 4500 mm/s, hatch distance 110 μm and layer thickness 75 μm. Therefore, variable parameters were scanning speed and laser power. It was noticed that when the scanning speed was too high (over 3500 mm/s), no connection of powder particles was obtained for any of the specified laser power parameters. As expected, the most significant penetration and powder connection occurred at the lowest scanning speeds (1500 mm/s) and the highest laser power (340 W). The highest relative density of 99.7% was obtained in this case. The obtained parts were characterized by low porosity. An amorphous structure was obtained in the entire volume, while the thermal stability and magnetic properties were similar to the powder being the input material. The authors recommend refining the process parameters because the samples produced had undesirable micropores, which most often initiate cracks in the produced parts.

In papers [122–124], changes in the microstructure, changes in mechanical properties, and the effect of the presence of micropores on cracks created in the L-PBF process using $Fe_{43.7}Co_{7.3}Cr_{14.7}Mo_{12.6}C_{15.5}B_{4.3}Y_{1.9}$ alloy are presented. Also, simulations using the finite element method were used. In the first research phase, attempts were made to determine the optimal process parameters: laser power 150 - 350 W, scanning speed 200 - 1000 mm/s, hatch distance 100 μm and layer thickness 40 μm, where cubic elements consisting of 12 layers were produced. Based on the tests, it was possible to produce fully amorphous elements for the following parameters: P = 200 W and v = 1000 mm/s. At too high laser power (350 W) and low scanning speed (200 mm/s), the formation of phases $(Fe, Cr)_3B$ and $(Fe, Cr)_{23}(C, B)_6$ occurring in the heat-affected zone was observed. To reduce the occurrence of undesirable phases, the energy density should be controlled and

optimized. Another important aspect is the occurrence of pores in the volume of manufactured elements, which are most often microcrack precursors. The authors explain the formation of cracks by accumulating thermal stresses on the surface between the liquid pool and the heat-affected zone, which strictly depends on the pores' size. The critical pore size resulting in the formation of cracks has been determined to be 30 μm. The authors proposed Cu and $CuNi_x$ doping to improve mechanical properties, thus forming a nanocomposite. The use of the described procedures increased tensile strength and impact strength.

Z. Mahbooba et al. [125] highlighted the limited possibility of producing amorphous elements by conventional manufacturing methods, among others, casting into copper molds. In his work, analyzing the structural aspects and mechanical properties of metallic glasses from the Fe-Cr-Mo-C-B group obtained using laser powder bed fusion technology with appropriate parameters: laser power 80-200 W, scanning speed 800-5000 mm/s, hatch distance between 50-150 μm and 20 μm layer thickness. The authors do not provide strictly defined parameters for which a cylinder with a relative density of 97% and practically completely amorphous was manufactured. A big problem occurring in L-PBF technology is the appearance of cracks and surface imperfections. In this case, the manufactured element was free from such defects. In hardness tests, a hardness of 902 HV was obtained. The approximate value of the elasticity modulus was estimated at 220 GPa, while Poisson's ratio was 0.3. These values are similar to bulk metallic glasses with similar chemical composition.

The work [95] describes the impact of process parameters such as laser power 220-380 W, scanning speed 2000 mm/s, hatch distance 90 μm and layer thickness 50 μm on mechanical properties, thermal stability, and microstructure of the $Fe_{49.6}Cr_{18.1}Mn_{1.9}Mo_{7.4}W_{1.6}B_{15.2}C_{3.8}Si_{2.4}$ alloy obtained in L-PBF technology. Elements manufactured using a laser power of 220 W had a relative density of 89.9%, while in the case of a 340 W laser power, the obtained relative density was 96.8%. The produced elements were characterized by an amorphous structure with few crystalline phases (α-Fe), while the nano hardness was about 13.7 GPa.

Ł. Żrodowski et al. [126] proposed a new strategy for producing metallic glasses with a low glass-forming ability in L-PBF technology. This method consisted of

two-step melting of the same layer with random spot scanning of a laser beam. The following parameters were used:

- in the first step: laser power 20 W, layer thickness 50 μm, exposure time 500 μs, point distance 100 μm, hatch distance 100 μm, focal spot diameter 40 μm,
- in the second step (re-melting): maximum laser power 120 W, layer thickness 50 μm, minimum point distance 1 mm, focal spot diameter 40 μm.

Due to the possibility of internal stresses in the material due to laser powder bed fusion, the obtained samples were heated to 550 °C and then cooled down. Thus, parts with an amorphous volume of 89.6% were obtained. The remaining part was the crystalline phase Fe(Si) and Fe_3Si. Besides, thanks to the used heat treatments, the L-PBF-inducted stresses were reduced, thereby reducing magnetic coercion, which was vital for metallic glass such as $Fe_{71}Si_{10}B_{11}C_6Cr_2$.

Tab. 2.2. *To date produced Fe-based metallic glasses in L-PBF and the implemented process parameters*

Alloy composition	P (W)	v (mm/s)	s (mm)	d (μm)	Year	Ref.
$Fe_{74}Mo_4P_{10}C_{7.5}B_{2.5}Si_2$	320	3470	0.124	–	2013	[120]
$Fe_{68.3}C_{6.9}Si_{2.5}B_{6.7}P_{8.7}Cr_{2.3}Mo_{2.5}Al_{2.1}$	280–340	1500–4500	0.11	–	2015	[121]
	250	200–800	–	80	2018	[124]
$Fe_{43.7}Co_{7.3}Cr_{14.7}Mo_{12.6}C_{15.5}B_{4.3}Y_{1.9}$	150–190	600	–	80	2018	[122]
	150–350	200–1000	0.1	80	2018	[123]
FeCrMoCB	80–200	800–5000	0.05-0.15	–	2018	[125]
$Fe_{92.4}Si_{3.1}B_{4.5}$	90	100–1500	0.04	34	2018	[127]
$Fe_{54.35}Cr_{18.47}Mn_{2.05}Mo_{13.93}W_{5.77}B_{3.22}C_{0.90}Si_{1.32}$	260–380	2000	0.09	–	2019	[95]
$Fe_{71}Si_{10}B_{11}C_6Cr_2$	20–120	–	0.1	40	2019	[126]
$Fe_{73.7}Si_{11}B_{11}C_2Cr_{2.28}$	90	–	0.08	10	2020	[128]
$Fe_{79}Zr_6Si_{14}Cu_1$	100-180	700–1000	0.1	80	2021	[129]
$(Fe_{0.76}B_{0.1}Si_{0.09}P_{0.05})_{99}Nb_1$	90–230	1000–1700	0.095	–	2022	[130]
$Fe_{55}Cr_{25}Mo_{16}B_2C_2$	100	300	0.105	–	2022	[131]
	100–120	230–400	0.05	50	2022	[132]
FeCrMoWMnSiBC	60–420	1200–3400	0.095	30	2022	[133]
$Fe_{73}Si_{11}Cr_2B_{11}C_3$	80–370	800–6000	–	–	2022	[134]

Based on the described works (Tab. 2.2), the following relationships can be noticed regarding the selection of laser powder bed fusion process parameters:

- Too low laser power does not guarantee that the powder will be melted and consequently does not result in permanent bonding of layers. Too high laser power can cause too high energy density, which in turn significantly affects the formation of microcracks and crystallization in the heat-affected zone,
- Too high scanning speed may result in too low energy density. Thus, it can result in no connection of powder, in consequence, not creating a permanent connection between layers. Too low scanning speed can result in a high energy density, determining the formation of cracks and crystallization in the heat-affected zone.
- The hatch distance affects the amount of supplied energy to the powder layer. It is assumed that these distances should not exceed the width of the melt pool.

As described in Chapter 2.1, metallic glasses are mainly produced through conventional technologies in the form of ribbons or rods. Thanks to the use of L-PBF technology, it is possible to produce parts with more complex geometries. The small melt pool, which allows for rapid heat dissipation, theoretically enables the production of iron-based metallic glasses. So far, in L-PBF technology, an electric motor rotor with a nanocomposite structure consisting of an amorphous matrix and nanometric crystalline phases has been produced [134]. Figure 2.6 shows the L-PBF-produced rotor and typical melt-spinning ribbons of $Fe_{73}Si_{11}Cr_2B_{11}C_3$ alloy.

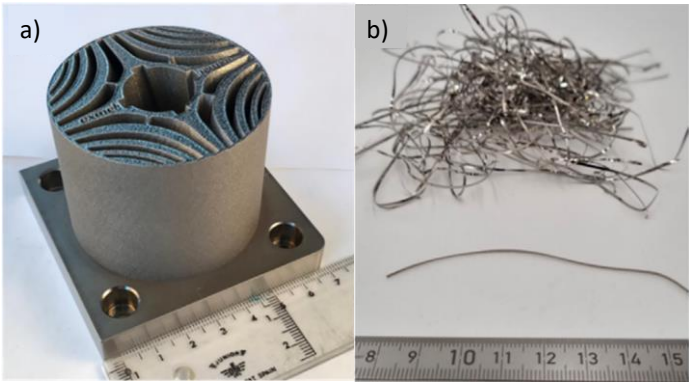

Fig. 2.6. *Electric motor rotor produced in L-PBF technology (a) and ribbons manufactured in conventional melt-spinning method (b). Taken from [134]*

3. Research gap and approach

The conducted "State of the art" directly shows the research gaps and the potential for producing still not fully understood metallic glasses in the laser powder bed fusion technology. Even more so in the case of iron-based metallic glasses, for which only a few papers have been published. In relation to the above, three areas that will contribute to further understanding of relatively new materials, such as iron-based metallic glasses in L-PBF technology, have been identified. The following subsections contain the areas, main aim of this work and the approach to the above-mentioned subjects.

3.1. Production of two different iron-based metallic glasses with low and high glass-forming abilities through the laser powder bed fusion process

Metallic glasses are mainly produced using conventional technologies, which results in their small size and limited geometry. The L-PBF technology, due to the small melting area, achieves high cooling rates, allowing the production of metallic glasses of complex shapes and much larger sizes than in conventional technologies, which would significantly contribute to the use of this group of materials in the industry. Therefore, it is crucial to determine the processability of metallic glasses in the L-PBF technology.

3.2. Influence of process parameters on the crystallization of iron-based metallic glasses during the L-PBF process

During the L-PBF process, metallic glasses may crystallize due to cyclic re-melting and accompanying heat transfer into the material. Areas of the heat-affected zone are particularly vulnerable. Controlled and conscious crystallization of metallic glasses can improve their properties. Nevertheless, it is crucial to know the influence of individual process parameters on emerging crystal structures.

3.3. Influence of process parameters on the functional properties of iron-based metallic glasses

Metallic glasses produced in conventional technologies have several beneficial properties. The use of manufactured elements, in addition to the aforementioned properties, is also determined by the low share of defects, which include porosity and the appearance of cracks. Depending on the process parameters that correspond with the supplied energy, it is possible to form both the structure and the number of defects in the final products.

3.4. The main aim of the work

Based on the literature review and the observed research gaps, the aim of the work was formulated:

Determination of the processability of Fe-based metallic glasses in the laser powder bed fusion technology based on two alloys with low and high glass-forming ability concerning the obtained microstructure, defects, and hardness.

3.5. Approach and research plan

Powder characterization

In the L-PBF technology, the material to be remelted is in the form of powder. Good powder quality does not always guarantee the production of elements with excellent characteristics, which mainly depends on selecting process parameters. Nevertheless, a powder with an inappropriate fraction, extensive morphology or high humidity can contribute to undesirable events, such as the impossibility of creating a homogeneous powder layer, already in the initial phase. In addition, pores trapped inside individual powder particles will introduce additional risks in producing elements with high relative density. Low absorptivity, characterizing the ability of the powder to absorb the electromagnetic wave by the powder, will affect the efficiency of the process itself and the laser power used to provide the appropriate energy to melt the powder. In connection with the above, the powder particle size distribution, reflectivity, chemical composition, shape, and cross-section of the powder were studied. The tests carried out are described in detail separately for two different alloys in chapters 5.2 and 6.2.

Porosity reduction via process parameters

The applicability of the material of a given material, in addition to physicochemical or mechanical properties, is also determined by the low share of defects, which include porosity. Low laser powers and low scanning rates are recommended for iron-based metallic glasses to achieve both an amorphous structure and a low pore content. Nevertheless, the use of low laser power values may result in too low energy supply, resulting in limited powder melting, thus affecting high porosity. Therefore, tests were carried out with low and high laser power values and variable scanning speeds. These tests are described in chapters 5.4 and 6.4 for iron-based metallic glass with low and high glass-forming ability, respectively.

Microstructure evolution concerning process parameters

The properties of materials are most often evidenced by the obtained microstructure, which can be shaped by the treatments carried out. In the case of metallic glasses, the obtained amorphous structure also determines their properties. Nevertheless, obtaining only an amorphous structure in the entire cross-section is not always beneficial. In the L-PBF technology, during production, due to the amount of thermal energy supplied, crystallization may occur, mainly of alloys with low glass-forming ability, both by too low cooling rate and by cyclic heat transfer into the material. Controlled and planned crystallization in some iron-based metallic glasses can improve their magnetic properties, which has been a wide area of research. The description and characterization of the structures obtained depending on the applied process parameters were made in chapters 5.5 and 6.5.

Hardness in relation to process parameters

Metallic glasses have high strength/mechanical parameters resulting from the amorphous structure and the lack of typical structure defects observed in conventional crystalline alloys. In order to determine the impact of individual process parameters on the obtained hardness, tests were carried out, the results of which are presented in chapters 5.6 and 6.6.

Research plan

In the dissertation, tests were conducted for two different iron-based amorphous alloys with low and high glass-forming abilities. The L-PBF processes and the performed tests were carried out in various research units. Therefore, two separate chapters have detailed descriptions of the devices on which the tests were carried out. Nevertheless, the approach and scope of the tests remained the same for the two alloys and are shown in the research plan in Fig. 3.1.

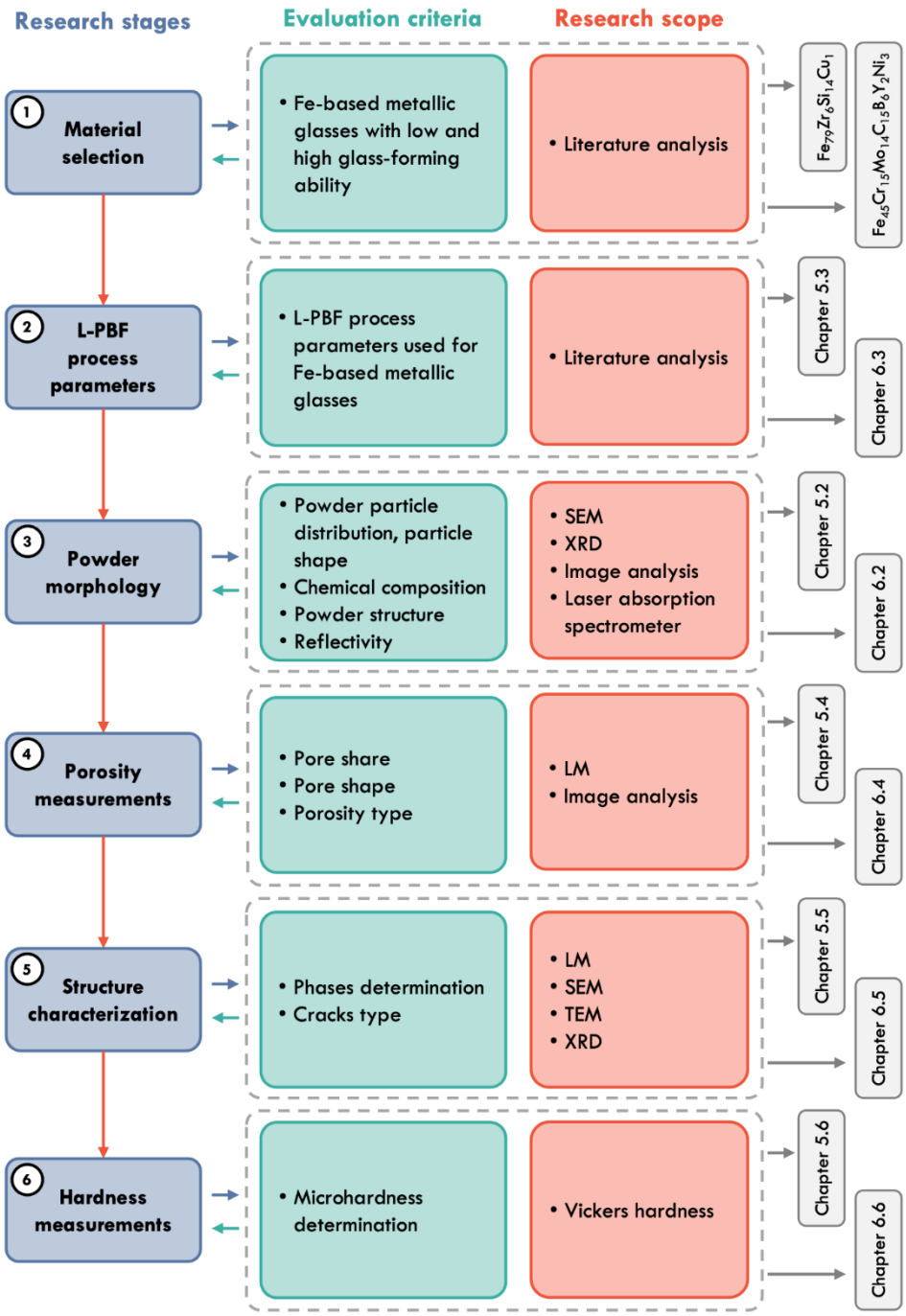

Fig. 3.1. *Research plan of two Fe-based alloys manufactured in L-PBF technology*

4. Materials

4.1. $Fe_{79}Zr_6Si_{14}Cu_1$ (at.%) alloy

Research on alloys from the Fe-Zr-Si group has been presented in [135–137]. Individual iron-based metallic glasses' microstructures and magnetic properties were determined before and after aging and after copper doping. For this purpose, 20-30 μm thick ribbons were produced using the melt-spinning method. J. Long et al. [135] produced ribbons having an amorphous structure for $(FeCu)_{80}Zr_xSi_{20-x}$ (x=5, 6, 8) alloys, which was confirmed using X-ray diffraction. In addition, the manufactured samples were subjected to annealing at 450 °C, 480 °C, and 550 °C. As a result of the heat treatment carried out in the primary crystallization temperature, a nanocomposite consisting of an amorphous matrix containing crystalline α-Fe(Si) phases was obtained. The phase sizes depended on the annealing temperatures, carried out for 1 hour, and were 10 nm for 480 °C and 14 nm for 550 °C. After doping copper into different alloys, the regular crystalline phases distribution was observed, which confirmed the positive effect of Cu addition on the nucleation of Fe-based amorphous alloys described in [138,139]. In turn, the size and distribution of nanocrystalline phases determine magnetic properties, such as low coercivity and low magnetic core loss. The amorphous structure was obtained only for thin ribbons in the melt-spinning method, indicating low glass-forming ability.

4.2. $Fe_{45}Cr_{15}Mo_{14}C_{15}B_6Y_2Ni_3$ (at.%) alloy

The $Fe_{45}Cr_{15}Mo_{14}C_{15}B_6Y_2Ni_3$ alloy can be classified as a bulk metallic glass from the Fe-Cr-Mo-C-B-Y group. These alloys are characterized by high glass-forming abilities, for which the maximum critical diameter of 8 mm was obtained for the $Fe_{48}Cr_{15}Mo_{14}C_{15}B_6Y_2$ alloy [140]. Due to the high hardness obtained, these materials show high resistance to abrasion. For the $Fe_{48}Cr_{15}Mo_{14}C_{15}B_6Y_2$ alloy, a hardness of 1188 HV0.3 and Young's modulus of 206 GPa [140] were obtained. $Fe_{45}Cr_{15}Mo_{14}C_{15}B_6Y_2Ni_3$ metallic glass has been described in article [141], in which a rod with a diameter of 3 mm was produced. The tests carried out made it possible to determine the characteristic temperatures causing structural changes due to

the heating of the alloy. The determined glass transition temperature was approximately 570 °C, and the crystalline onset temperature was 620 °C. In the samples annealed at 640 °C, the intermetallic phase $(Fe, Cr)_{23}(C, B)_6$ was observed apart from the amorphous phase. Further heating to the temperature of 710 °C led to the crystallization of the Fe_3Mo_3C phase.

5. Laser powder bed fused Fe-Zr-Si-Cu alloy

5.1. Examinations methods

Metallography

The samples for structural investigations were first embedded in epoxy resin, then subsequently wetly polished using grinding papers and diamond pastes. Finally, to reveal the microstructure, the polished samples were etched with a 3% nitric acid and alcohol solution.

Light microscopy

The samples' porosity and microstructure observations were performed on Nikon Eclipse MA200 light microscope equipped with Nikon DS-Fi2 digital camera.

Scanning electron microscopy

The microstructure and chemical composition investigations were carried out using JEOL JSM-6610A scanning electron microscope. The structural observations were conducted in material contrast using a back-scattered electrons detector (BSE detector) in an etched state. The chemical composition analysis was performed by energy-dispersed X-ray method using a JEOL JED-2300 spectrometer coupled with the scanning electron microscope. During the performed surface microanalysis, all elements lighter than carbon were excluded due to the relatively high measurement error.

Transmission electron microscopy

The lamella for transmission electron microscopy observations was prepared with SEM/Ga-FIB Microscope FEI Helios NanoLab™ 600i. The TEM investigations were carried out with Hitachi H-800 Transmission Electron Microscope, working with 150 kV acceleration voltage. The selected area diffraction patterns were calculated with CrysTBox software [142].

X-Ray diffraction

The X-ray diffraction measurements were performed using an Empyrean (PANalytical) diffractometer with Co Kα irradiation (λ = 1.78901 Å) within

the range from 30° to 110° in 0.01° steps with an exposure time of 1 s per point. The XRD spectra were analyzed in Profex software [143].

Hardness measurements

The hardness measurements were conducted on Zwick-Roell ZHVμ-A fully automatic Vickers machine. The indentation was performed with a 1 kg load and in accordance with the EN ISO 6507 norm.

5.2. Powder characterization

The $Fe_{79}Zr_6Si_{14}Cu_1$ (at. %) powder was gas atomized by the NANOVAL company and then sieved to the +15/-50 μm fraction. The powder's particle size distribution has been determined through the digital process of five randomly taken photos using a scanning electron microscope during observations in material contrast. The powder particle size measurements were conducted in open-source Fiji/ImageJ software.

Based on the visual analysis, a histogram showing the distribution of powder particle fractions was made (Fig. 5.1). The calculated median average size of the powder was 30.6 μm, and the lower and upper deciles were respectively, 26.3 μm and 42.1 μm.

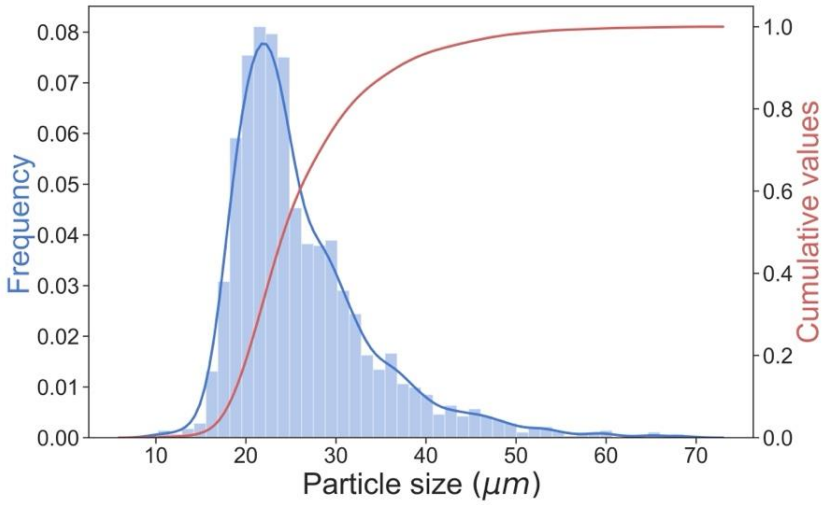

Fig. 5.1. *Particle size distribution of the $Fe_{79}Zr_6Si_{14}Cu_1$ powder*

Due to the manufacturing process of the powder, besides its mainly spherical shape, some powder particles had diverse morphology consisting of many smaller

satellite particles, which is typical for gas atomization. As observed (Fig. 5.2), a large amount of the particles was also covered with build-up coatings, protrusions and dents.

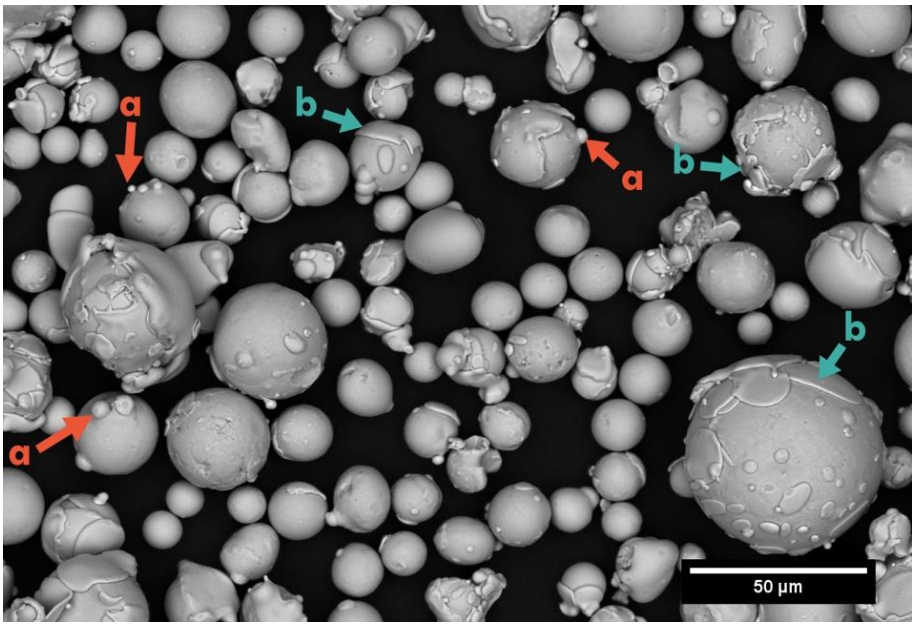

Fig. 5.2. *$Fe_{79}Zr_6Si_{14}Cu_1$ powder particles morphology with visible satellite particles (a) and built-up coatings (b)*

The chemical composition of the powder was carried out by the EDX method in three random areas of the powder. The results of the measurements are presented in Table 5.1. The mean values of the alloy composition in atomic percentages were: %Fe – 79.20, %Si – 13.92, %Zr – 5.87 and %Cu – 1.01.

Tab. 5.1. *Chemical compositions of Fe-based powder in at. %*

Element	I	II	III	Mean	SD
Fe	79.64	78.82	79.14	79.20	0.41
Si	13.85	13.95	13.95	13.92	0.06
Zr	5.56	6.20	5.85	5.87	0.32
Cu	0.95	1.03	1.06	1.01	0.06

During conducted microscopic investigations of the powder cross-sections using a scanning electron microscope, a multi-phase dendritic structure was observed (Fig. 5.3), which was confirmed by the presence of various contrast.

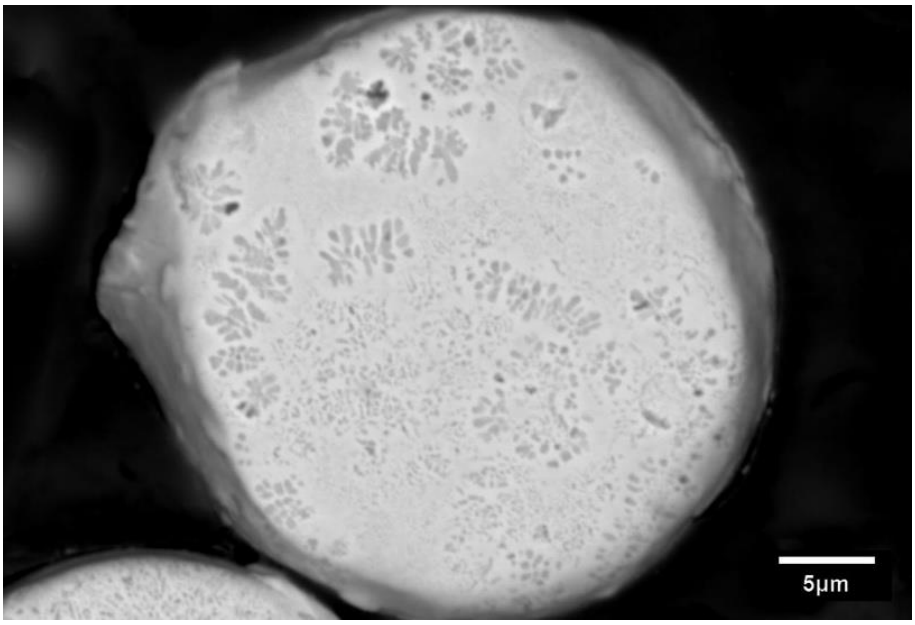

Fig. 5.3. *Powder cross-section of $Fe_{79}Zr_6Si_{14}Cu_1$ alloy showing crystalized dendritic structure*

According to the X-Ray diffraction measurements (Fig. 5.4), the powder contained in the structure mainly α-Fe(Si) solid solution and $Fe_{23}Zr_6$ intermetallic phase. Moreover, trace amounts of the $FeZr_2$ intermetallic phase and $Fe_{16}Si_7Zr_6$ phase were identified in the powder structure.

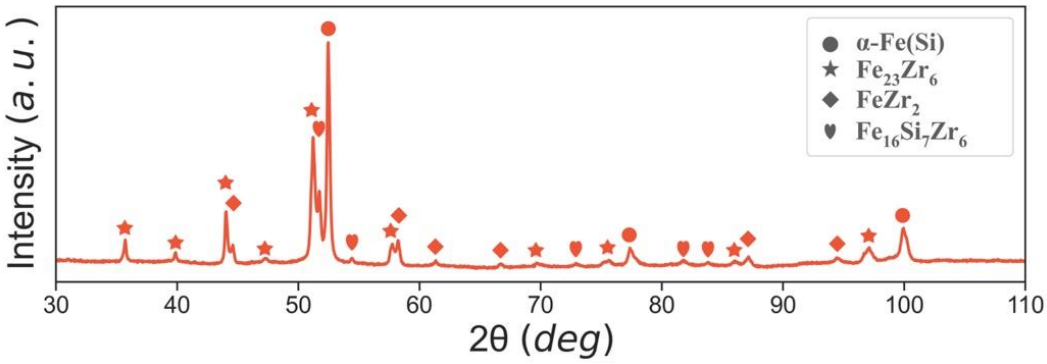

Fig. 5.4. *XRD spectrum of the $Fe_{79}Zr_6Si_{14}Cu_1$ powder with a qualitative determination of the phases*

The reflexivity of the powder for different wavelengths, between 900 and 1100 nm, was measured by a laser diffractometer. The results of the investigations are presented in Figure 5.5.

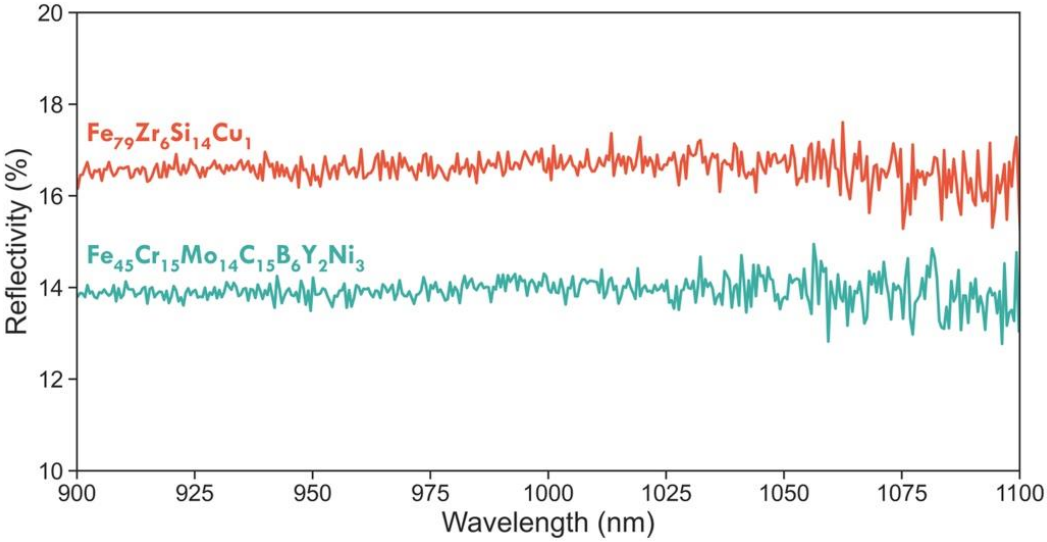

Fig. 5.5. *Comparison of the reflectivity of the two powders used.*

5.3. L-PBF process parameters

For all conducted processes, the sample models were designed in Autodesk Netfabb Premium 2019 software. For the individual samples, by appropriate layer thicknesses, hatch spaces and scanning strategies, layers and paths were generated. The process parameters, like laser power and scanning speed, were specified in the device manufacturers control software Aconity STUDIO.

The Laser Powder Bed Fusion process was conducted using an Aconity MIDI machine equipped with a fiber laser. The laser beam with a focus diameter of 80 µm was generated with a wavelength of 1070 nm and a maximum power of 400 W at the powder bed. During the conducted processes, the build chamber was flooded with argon gas to limit the oxygen content below 100 ppm. The samples were manufactured directly on the 316L stainless steel building platform to provide fast heat dissipation.

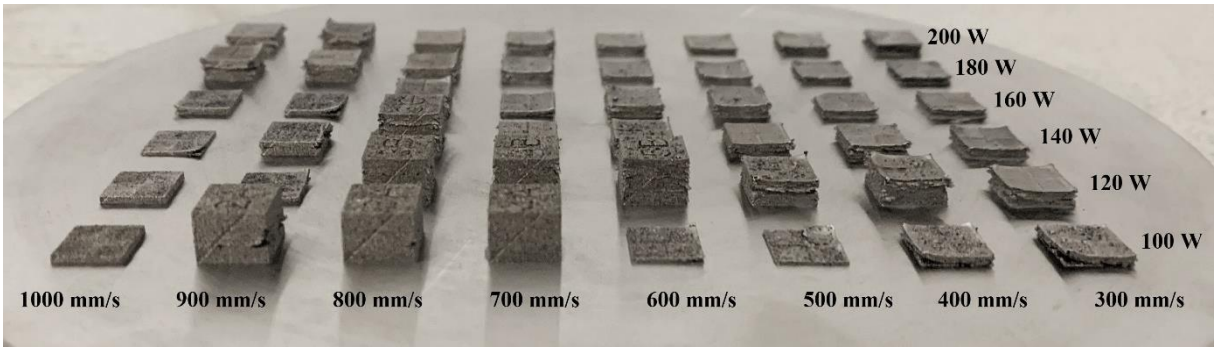

Fig. 5.6. *Samples produced in an early stage of the research with included process parameters*

The main experiment was performed for cylindrical specimens with a 5 mm diameter and height of 6 mm, based on reconnaissance studies, narrowing the process window (Fig. 5.6). During the process, several parameter variations with the laser power P ranging between 100 and 180 W and the scanning speed v between 700 and 1000 mm/s were implemented. The layer thickness t and hatch spacing s were set to 30 and 100 µm, respectively. The scanning strategy of 45° inclined back and forth line scanning with 90° rotation in the next layer was implemented (Fig. 5.7). The process parameters for all manufactured samples, with corresponding energy densities E_d calculated from equation 2.1, are presented in Table 5.2.

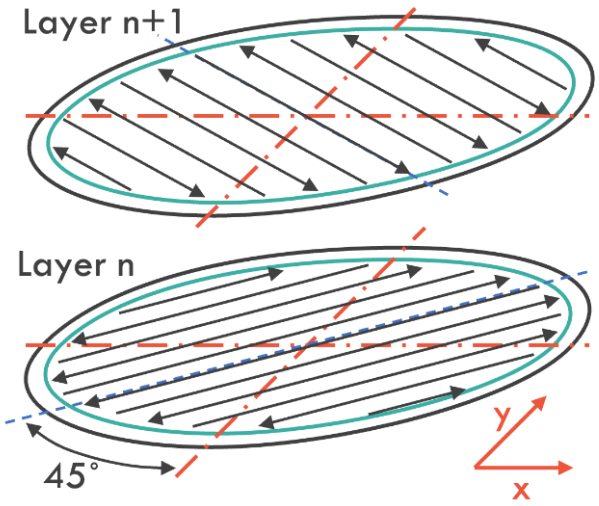

Fig. 5.7. *Schematic illustration of the scanning strategy used during the L-PBF process*

Tab. 5.2. *L-PBF parameters with corresponding energy densities (J/mm³).*

		Laser power (W)				
		100	**120**	**140**	**160**	**180**
Scanning speed (mm/s)	**1000**	33.3	40.0	46.7	53.3	60.0
	900	37.0	44.4	51.9	59.3	66.7
	800	41.7	50.0	58.3	66.7	75.0
	700	47.6	57.1	66.7	76.2	85.7

5.4. Porosity

The porosity measurements were conducted on the polished and unetched cross-sections of the samples. During the observations, each sample was photographed in three random areas. After this, the pictures were digitally processed to calculate the pore shares.

The conducted porosity measurements allowed the determination of pores percentage in relation to different laser powder bed fusion parameters. The first diagram shows the porosity shares in accordance with implemented laser power and scanning speed (Fig. 5.8). Based on the obtained results, it was found that the porosity of the samples decreased when increasing the laser power and decreasing the scanning speed. The highest pores percentage (24.4%) was measured for the sample manufactured with 100 W laser power and 900 mm/s scanning speed. The sample with the lowest porosity (0.4%) was produced by applying 180 W laser power and 800 mm/s scanning speed.

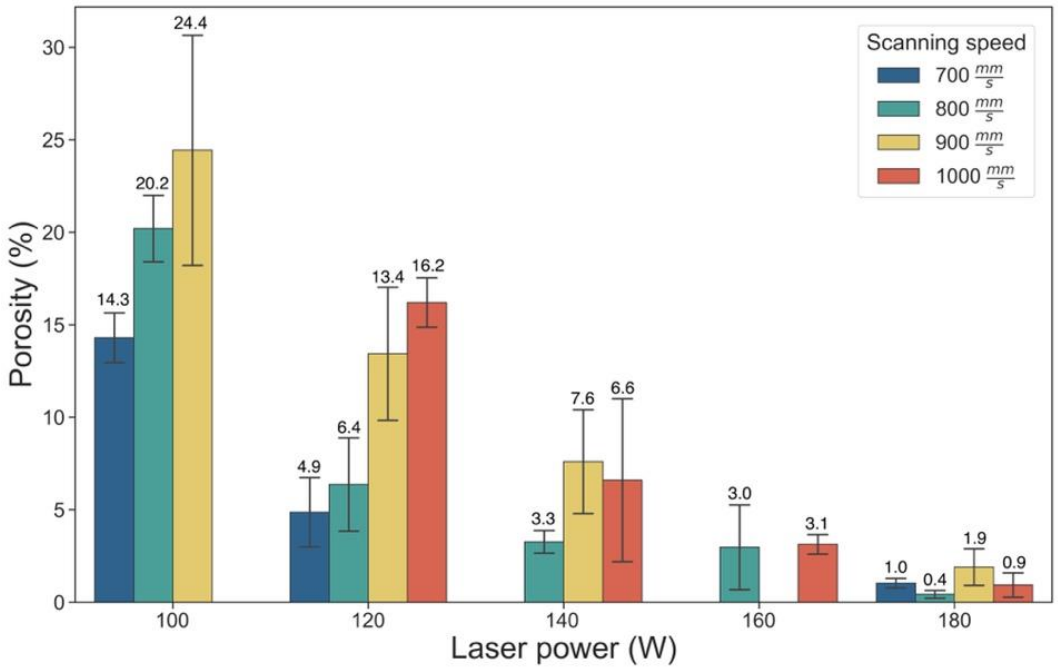

Fig. 5.8. *The porosity fractions of samples produced with varying laser power and scanning speed*

Comparing the measured porosity with the implemented laser energy density for different samples (Fig. 5.9) shows that while increasing the laser energy density, the percentage of pores decreased exponentially.

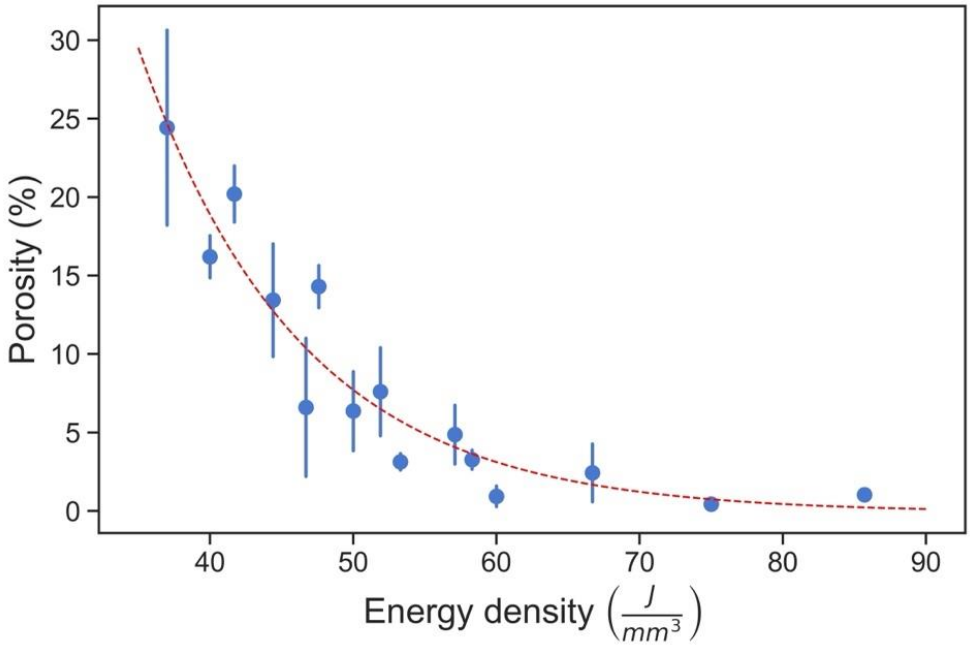

Fig. 5.9. *The porosity fractions of samples compared in accordance with implemented laser energy density*

5.5. Microstructure characterization

The conducted microscopic investigations using optical light microscope allowed the observation of significant differences between samples manufactured in laser powder bed fusion technology with applied various process parameters. The beads created during the process imitate the previous melt pool. Their shape varies significantly depending on the selected process parameters. When considering the width of the beads, it was found that it increased with the increase in scanning speed and with the increase in laser power.

The manufactured samples with different process parameters, besides the various shape, also had diverse, multi-phase structures (Fig. 5.10.ab). During the investigations, the samples were subjected to re-observation after three weeks from the day of conducting the L-PBF process. It contributed to the observation of a large number of microcracks (Fig. 5.10cd), which were not previously identified. The cracks nuclei formed after time were located mainly on the fusion line, while the propagation direction was normal to the fusion line.

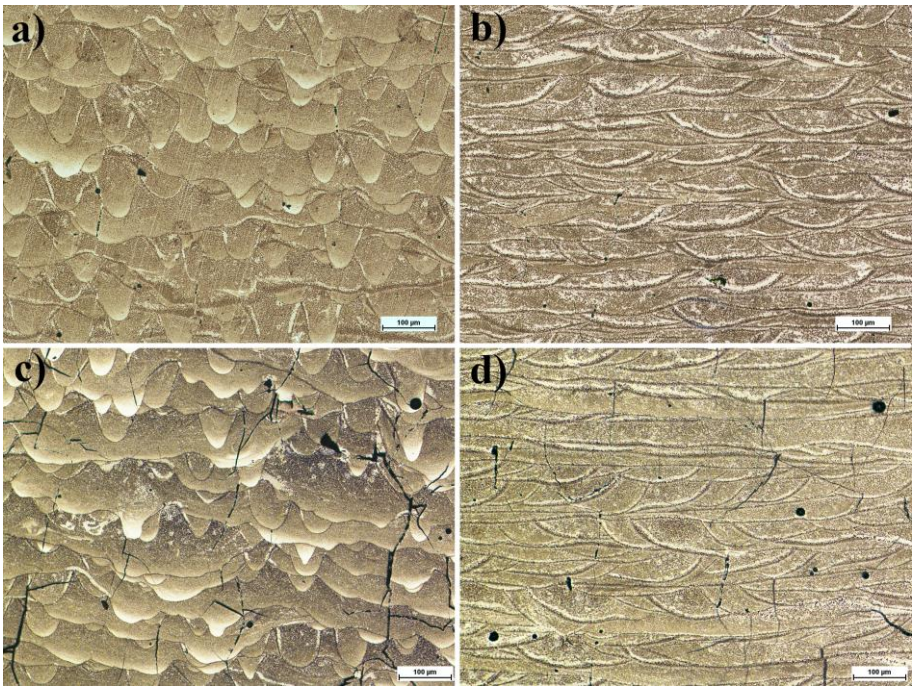

Fig. 5.10. *The microstructure of samples manufactured in L-PBF technology: (a) laser power 120 W, scanning speed 800 mm/, hatch distance 100 µm, layer thickness 30 µm, (b) laser power 180 W, scanning speed 700 mm/s, hatch distance 100 µm, layer thickness 30 µm. (c-d) parameters successively as in (a) and (b), three weeks after the process*

Scanning electron microscopy investigations allowed the observation of three different zones that characterize the bead created during the L-PBF process for the Fe-Zr-Si-Cu group alloy (Fig. 5.11.). The first zone was mainly composed of a fine, dendritic structure. The interdendritic area was characterized by homogeneous chemical composition, which confirms the presence of comparable contrast (Fig. 5.11a). During the SEM investigations, no dendrites were observed in the second zone. In this zone, the occurred structure was similar to the interdendritic areas. The third zone can be described as a fusion line and, compared to other areas, is characterized by a darker contrast. The present phases had an irregular, dendritic shape and a noticeable bright contrast. This suggests the segregation of zirconium, depleting the dendritic phase, which was confirmed by the chemical elements distribution (Fig. 5.11b-e). conducted by the EDX mapping.

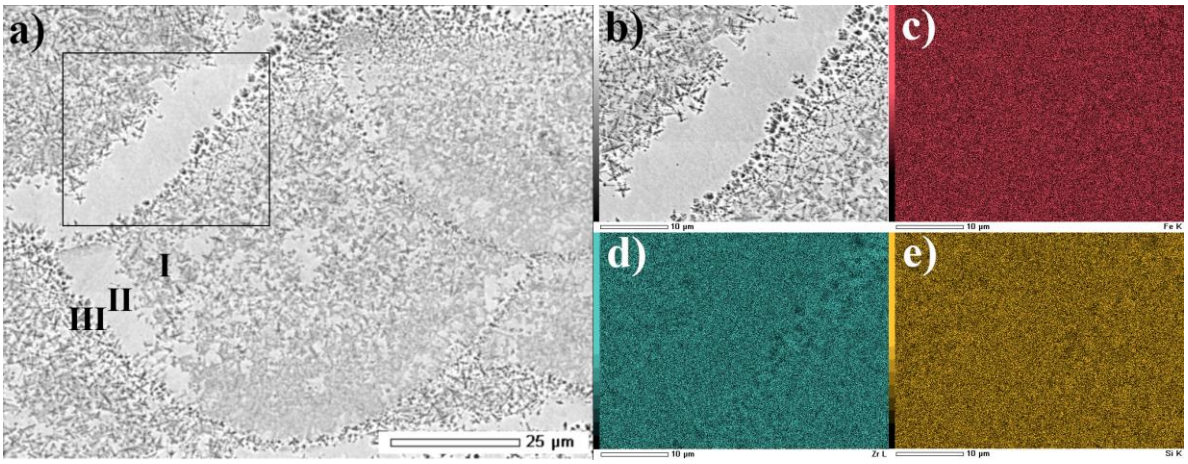

Fig. 5.11. *The microstructure of the bead in a sample manufactured in L-PBF technology (laser power 180 W, scanning speed 700 mm/s, hatch distance 100 µm, layer thickness 30 µm). Three zones are visible, marked as I, II, and III (a). EDX mapping of the tested sample: (b) reference image, (c) iron, (d) zirconium, and (e) silicon distribution*

To characterize in more detail the present phases, transmission electron microscopy observations were made (Fig. 5.12). Previously described zone three, the fusion line, mainly consists of dendritic solid solution α-Fe(Si), and in the interdendritic areas, intermetallic $FeZr_2$ and $Fe_{23}Zr_6$, which corresponds to the previous assumptions regarding zirconium segregation in the peri-dendritic region. In the second zone of the bead, the presence of nanometric α-Fe(Si) solid solution phases was observed, surrounded by an amorphous matrix. The presence of the amorphous phase is confirmed by the characteristic halo ring obtained on the selected area electron diffraction, shown in Figure 5.12e.

In order to indicate differences in phase occurrence for samples produced in laser powder bed fusion technology with different energy densities, X-ray diffraction studies were performed on two representative samples (same as in Fig. 5.10). Based on the conducted investigations, the low energy density sample contained α-Fe(Si) solid solution and $Fe_{23}Zr_6$ intermetallic phase. Similarly, the higher energy density sample consists of α-Fe(Si) and $Fe_{23}Zr_6$ phases. Moreover, a small fraction of the $FeZr_2$ intermetallic phase was apparent. Comparing the X-ray diffraction spectra (Fig. 5.13) between samples with lower and higher energy densities, higher content of $Fe_{23}Zr_6$ intermetallic phase was noticed in the sample manufactured with higher energy density. The assessment was based on the XRD reflex intensity values originating from different phases.

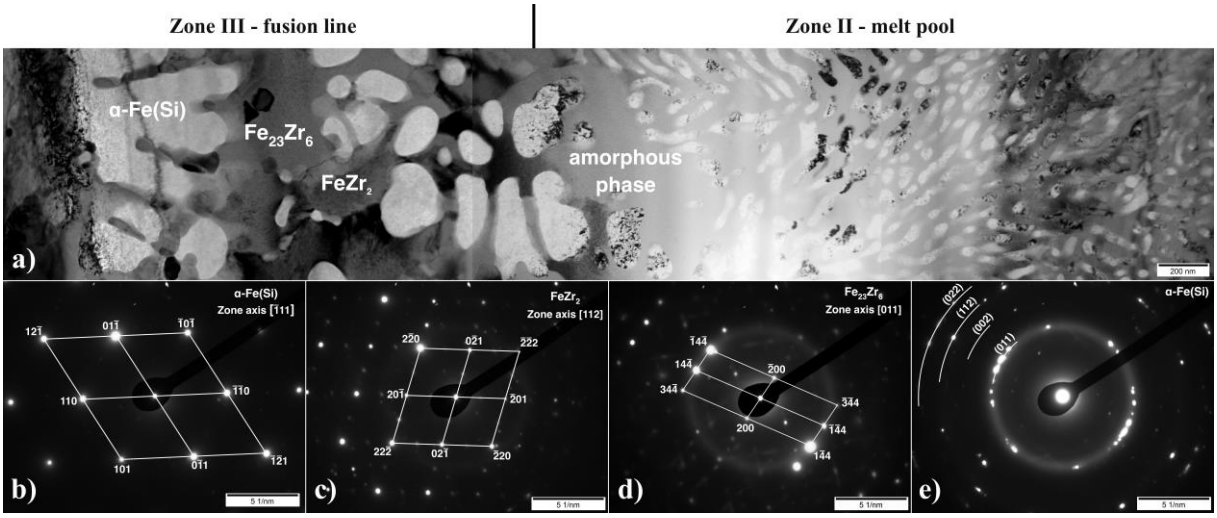

Fig. 5.12. TEM bright-field image of zone II and zone III (a), and the corresponding selected area electron diffraction patterns of the present phases: (b) α-Fe(Si), (c) $FeZr_2$, (d) $Fe_{23}Zr_6$, and α-Fe(Si) with an amorphous matrix

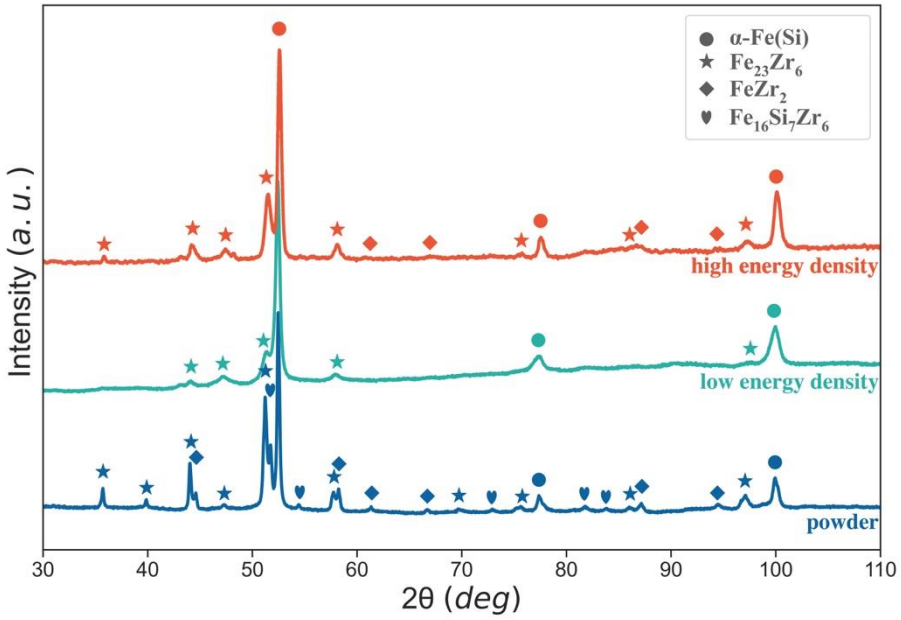

Fig. 5.13. X-ray diffraction spectrum with phase identification for powder and samples with lower and higher energy density, produced in the L-PBF technology

5.6. Hardness

Hardness measurements for samples produced in the L-PBF technology for the Fe-Zr-Si-Cu material are presented in Figure 5.14. The sample produced with a laser power of 120 W and a scanning speed of 900 mm/s was characterized by the highest hardness of 955 HV1. The lowest value was observed for a sample

produced with a laser power of 180 W and a scanning speed of 700 mm/s. Based on the conducted tests, decreases in hardness accompanying the increase in laser power to 160 W can be observed, similarly in the case of increasing scanning speeds. Only in the case of samples produced with a laser power of 180 W, increasing scanning speeds resulted in an increase in hardness.

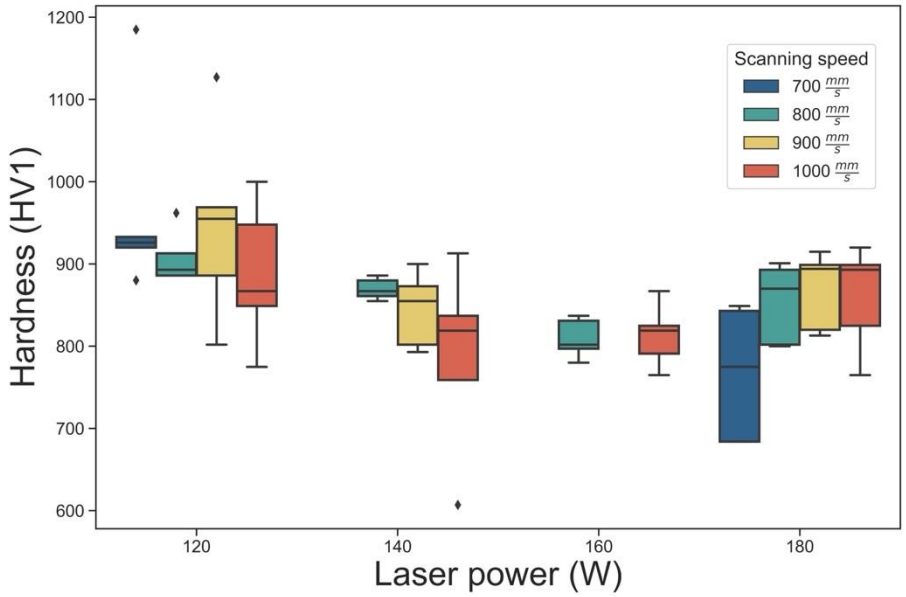

Fig. 5.14. *Hardness comparison of samples produced with varying laser powers and scanning speeds*

5.7. Discussion

The conducted laser powder bed fusion process contributed to significant structural changes of the Fe-Zr-Si-Cu metallic glass used for the first time in this technology. The majority of the powder structure constitutes α-Fe(Si) solid solution and $Fe_{23}Zr_6$ intermetallic phase. Moreover, small shares of $FeZr_2$ and $Fe_{16}Si_7Zr_6$ phases were identified. The use of various parameters of the laser powder bed fusion process, in this case, the laser power and the scanning speed, made it possible to indicate the structural differences in the material during the process. Higher scanning speeds and lower laser powers resulted in low laser energy density. Consequently, the beads produced were characterized by small widths and relatively high depths. For samples produced with low scanning speeds and high laser powers, the bead morphology differs significantly from samples

manufactured with low energy densities. The observed large widths and low depths are closely related to the melt pool size and the supplied energy [144].

In the case of the Fe-Zr-Si-Cu alloy, considering the kinetics and dynamics of crystallization, the first crystallizing phase is the α-Fe(Si) solid solution, and the second is the $Fe_{23}Zr_6$ intermetallic phase [135–137]. In samples with lower energy densities (120 W and 800 mm/s), the share of the second phase was lower due to the lower temperature gradients, which were higher in samples with higher energy densities (180 W and 700 mm/s) [145]. Typically, an amorphous structure for metallic glasses produced in the laser powder bed fusion is achieved in the melting zone through high cooling rates that enable this technology [123,126,146]. The primary phase crystallization appears most often in the fusion line and the heat-affected zone. Moreover, crystallization of the second and third phases in the heat-affected zone and the previous melting zone can also take place. This is due to the cyclically supplied heat during the manufacturing of the following layers, which leads to the diffusion increase of atoms [147]. In the investigated Fe-based metallic glass an amorphous structure was most likely obtained in the melt pool zone (zone I). However, as a result of cyclically supplied heat, the primary α-Fe(Si) phase crystallized. Crystallization mostly occurred in the solid solution α-Fe(Si) and intermetallic $Fe_{23}Zr_6$ and $FeZr_2$ in the fusion line and in the heat-affected zone (zone III). The performed transmission electron microscopy investigations confirmed the presence of nanometric precipitation of α-Fe(Si) solid solution and the amorphous matrix in zone II, which was the previous melt pool.

In the context of additive manufacturing technology and the application of produced parts, the examination of pore contributions is important from a technological perspective. The application of the created elements is mainly determined by the mechanical properties, including the material's structure and the defects that occur, which may be pores or microcracks [148]. Based on the performed porosity tests of the laser powder bed fused Fe-Zr-Si-Cu metallic glass manufactured with different process parameters, high scanning speeds (900-1000 mm/s) and low laser powers (100-140 W) leads to high pore content. This porosity was mainly processing-induced, which was driven directly by the low

laser energy density. Namely, low energy values caused limited liquid phase content during the process. This, mixed with fine powder particles, increased the viscosity of the melt pool and finally contributed to the lack of fusion formation with un-melted powder particles within large and irregular pores [121,148,149]. On the other hand, samples produced with low scanning speeds (700-800 mm/s) and high laser powers (160-180 W) were characterized by significantly lower pore content (0.4-3.0%), and it is related to higher values of the laser energy densities. The observed pores were primarily circular, and their form and distribution were typically for keyhole porosity [148,150].

In the laser powder bed fusion technology for some iron-based metallic glasses (e.g. $Fe_{43.7}Co_{7.3}Cr_{14.7}Mo_{12.6}C_{15.5}B_{4.3}Y_{1.9}$ at.%) micro-cracks are created during the building-up process. It is usually related to large thermal stress in the micro-pores area [124]. For the investigated $Fe_{79}Zr_6Si_{14}Cu_1$ alloy, where cracks appeared after some time, the mechanism of crack creation seems to be different. This demonstrates that thermal stress arises and accumulates in the material during the ongoing process. As previously noted, the fusion line is the most typical location for crack initiation, and the crack propagates normal to this line. There is most likely a structural notch at the interface between the crystalline and amorphous phases, which is a potential initiation fracture point because of the brittle crystalline phases formed during the process [151]. So far, the Fe-based metallic glasses manufactured in the laser powder bed fusion technology were characterized by many micro-cracks [95][120–124][126][128][146][152–154]. This could be prevented by process parameters improvement or by stress-relief annealing following the L-PBF process. Due to the fact that the $Fe_{79}Zr_6Si_{14}Cu_1$ alloy starts to crystallize from the amorphous phase after exceeding the primary crystallization temperature, it would be possible by using the appropriate heat treatment up to 490°C [155]. Therefore, releasing the thermal-induced stresses inside the material would be an outstanding possibility. The laser powder bed fusion of crack-free samples using Fe-based metallic glasses is currently challenging. So far, only one work describes the production of crack-free samples by implementing a novel chessboard scanning strategy [156].

6. Laser powder bed fused Fe-Cr-Mo-C-B-Y-Ni alloy

6.1. Examinations methods

Metallography

The samples for structural investigations were first embedded in epoxy resin, then subsequently wet polished using grinding papers and diamond paste.

Light microscopy

The samples porosity and microstructure observations were performed on Olympus LEXT OLS4000 confocal microscope.

Scanning electron microscopy

The microstructure and chemical composition investigations were carried out using Carl Zeiss EVO MA25 scanning electron microscope. The structural observations were conducted in material contrast using back-scattered electrons detector (BSE detector). The chemical composition analysis was performed by energy-dispersed X-ray method. During the performed surface microanalysis all elements lighter than carbon were excluded due to the relatively high measurements error.

Transmission electron microscopy

The lamella for transmission electron microscopy observations was prepared with SEM/Ga-FIB Microscope FEI Helios NanoLab™ 600i. The TEM investigations were carried out with Hitachi H-800 Transmission Electron Microscope, working with 150 kV acceleration voltage.

X-Ray diffraction

The X-ray diffraction measurements were performed using Rigaku MiniFlex 600 XRD diffractometer with Cu Kα radiation (λ = 1.5406 Å) within the range from 30° to 90° in 0.01° steps with an exposure time of 1 s per point. The XRD spectra were analyzed in Profex software [143].

Hardness measurements

The hardness measurements were conducted on Zwick-Roell ZHVμ-A fully automatic Vickers machine. The indentation was performed with 1 kg load and in accordance to the norm EN ISO 6507.

6.2. Powder characterization

The $Fe_{45}Cr_{15}Mo_{14}C_{15}B_6Y_2Ni_3$ (at. %) powder was gas atomized by the NANOVAL company and then sieved to the +15/-50 μm fraction. The determination of particle size distribution of the powder has been conducted through digital process of five randomly taken photos using a scanning electron microscope during observations in material contrast. The powder particle sizes measurements were conducted in open-source Fiji/ImageJ software.

Based on the visual analysis, a histogram showing the distribution of powder particles fractions was made (Fig. 6.1). The calculated median average size of the powder was 26.5 μm and the lower and upper decile were respectively 13.1 μm and 52.1 μm.

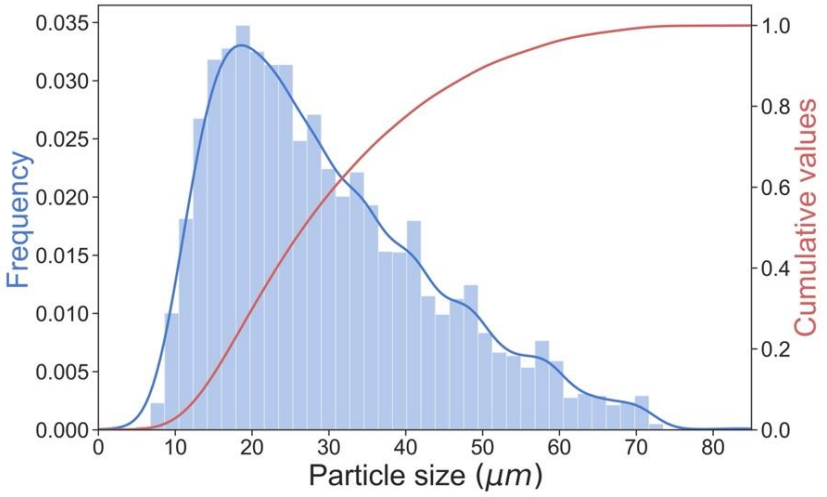

Fig. 6.1. *Particle size distribution of the $Fe_{45}Cr_{15}Mo_{14}C_{15}B_6Y_2Ni_3$ powder*

The powder produced in gas atomization process was characterized by a near spherical shape. Nevertheless, a large part of the powder particles was covered with build-up coatings called 'Splat Cap'. In addition, elongated rod-like particles and characteristic elongated drops were also observed, as shown in Fig. 6.2.

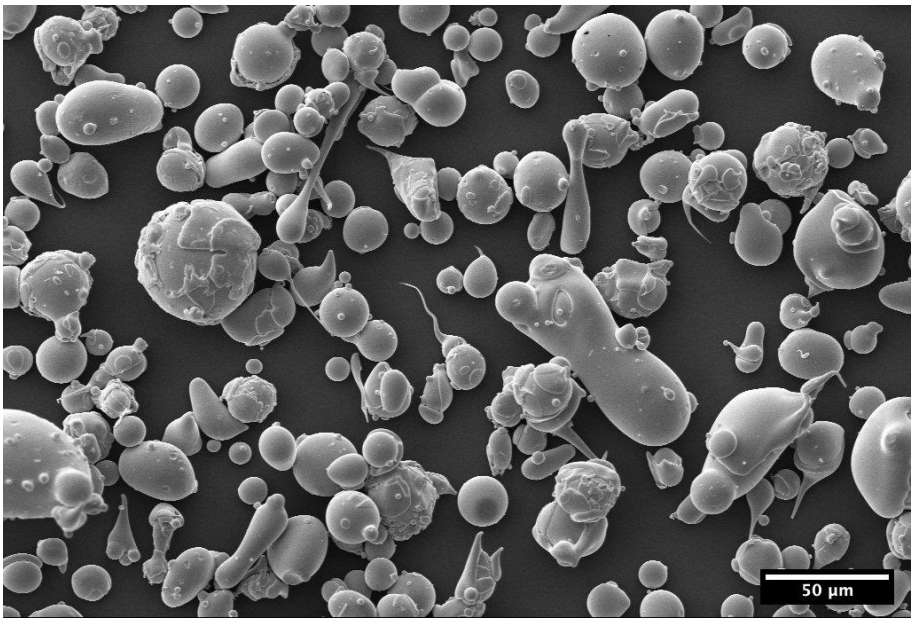

Fig. 6.2. *$Fe_{45}Cr_{15}Mo_{14}C_{15}B_6Y_2Ni_3$ powder particles morphology with visible satellite particles and built-up coatings*

The conducted microscopic examinations of the powder cross-section allowed the observation of homogeneous structure of the powder, which was indicated by a uniform contrast. For some powder particles, characteristic gas pores were also observed, formed during powder gas atomization (Fig. 6.3.).

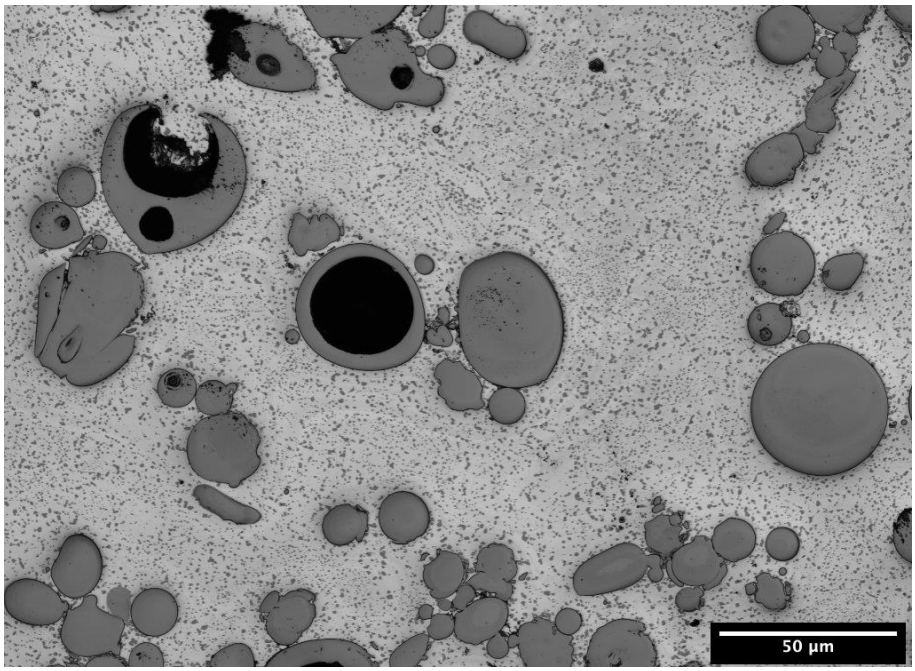

Fig. 6.3. *Powder cross-section of $Fe_{45}Cr_{15}Mo_{14}C_{15}B_6Y_2Ni_3$ alloy showing homogeneous structure and gas pores*

The chemical composition of the powder was carried out by the EDX method in three randomly areas of the powder. Due to the small atomic mass of boron the qualitative investigation was impossible, therefore this element was excluded from the examination. The results of the measurements are presented in table 6.1. The mean values of the alloy composition in atomic percentages are: %Fe – 49.51, %Cr – 16.11, %Mo – 14.67, %C – 13.86, %Y – 2.23 and %Ni – 3.62.

Tab. 6.1. *Chemical compositions of Fe-based powder in at. %*

Element	I	II	III	Mean	SD
C	13.16	16.10	12.33	13.86	1.98
Cr	16.66	15.27	16.41	16.11	0.74
Fe	49.86	47.84	50.82	49.51	1.52
Ni	3.81	3.49	3.57	3.62	0.17
Y	1.97	2.68	2.04	2.23	0.39
Mo	14.55	14.62	14.83	14.67	0.15

On the basis of the X-ray diffraction tests, only the amorphous structure was found in the tested powder, which is confirmed by the characteristic halo reflections around the 42.5° and 78.0° angle (Fig. 6.4).

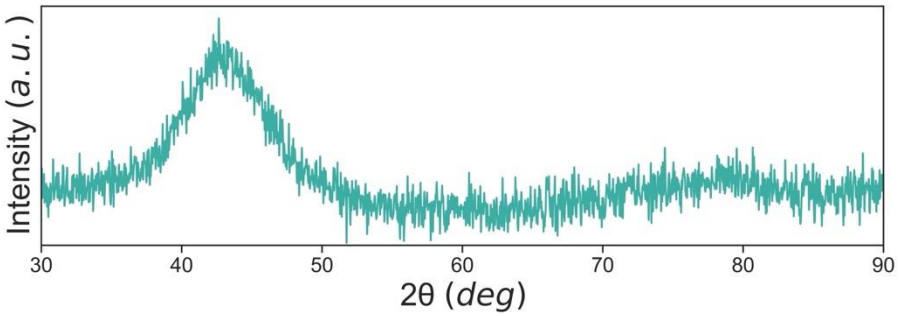

Fig. 6.4. *XRD spectrum of the $Fe_{45}Cr_{15}Mo_{14}C_{15}B_6Y_2Ni_3$ powder with characteristic amorphous reflection*

The reflexivity of the powder was measured by laser diffractometer in the wavelength range between 900 and 1100 nm. The results of the investigations are presented in figure 6.5.

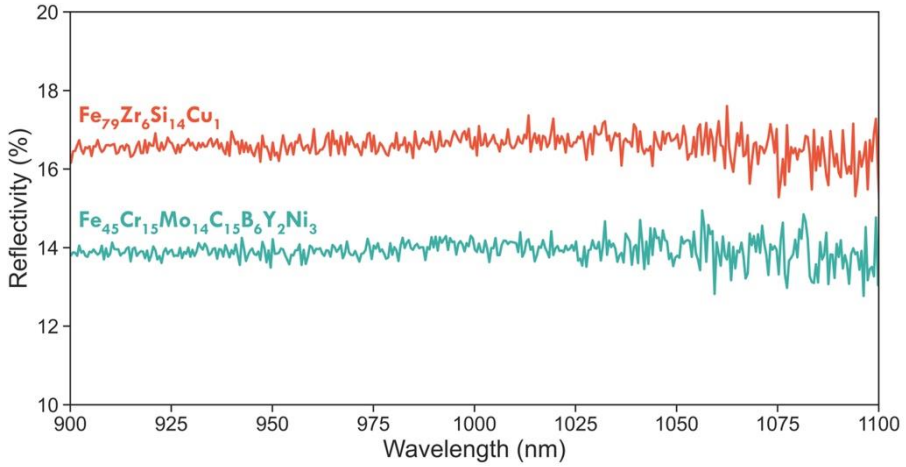

Fig. 6.5. *Comparison of the reflectivity of the two powders used*

6.3. L-PBF process parameters

For the tested material, the basic shape of the samples produced in the laser powder bed fusion technology was a cuboid with a square base. The STL models were designed in Autodesk Fusion360. In the software dedicated by the device manufacturer, the process parameters for individual samples were assigned, which are described in detail later in the text. The L-PBF process was carried out on a Realizer SLM 250 device equipped with an Ytterbium fiber laser with a wavelength of 1070 nm and a maximum power of 400 W. During the conducted processes, the build chamber was flooded with argon gas to limit the oxygen content below 100 ppm. The samples were manufactured directly on the 304 stainless steel building platform to provide fast heat dissipation.

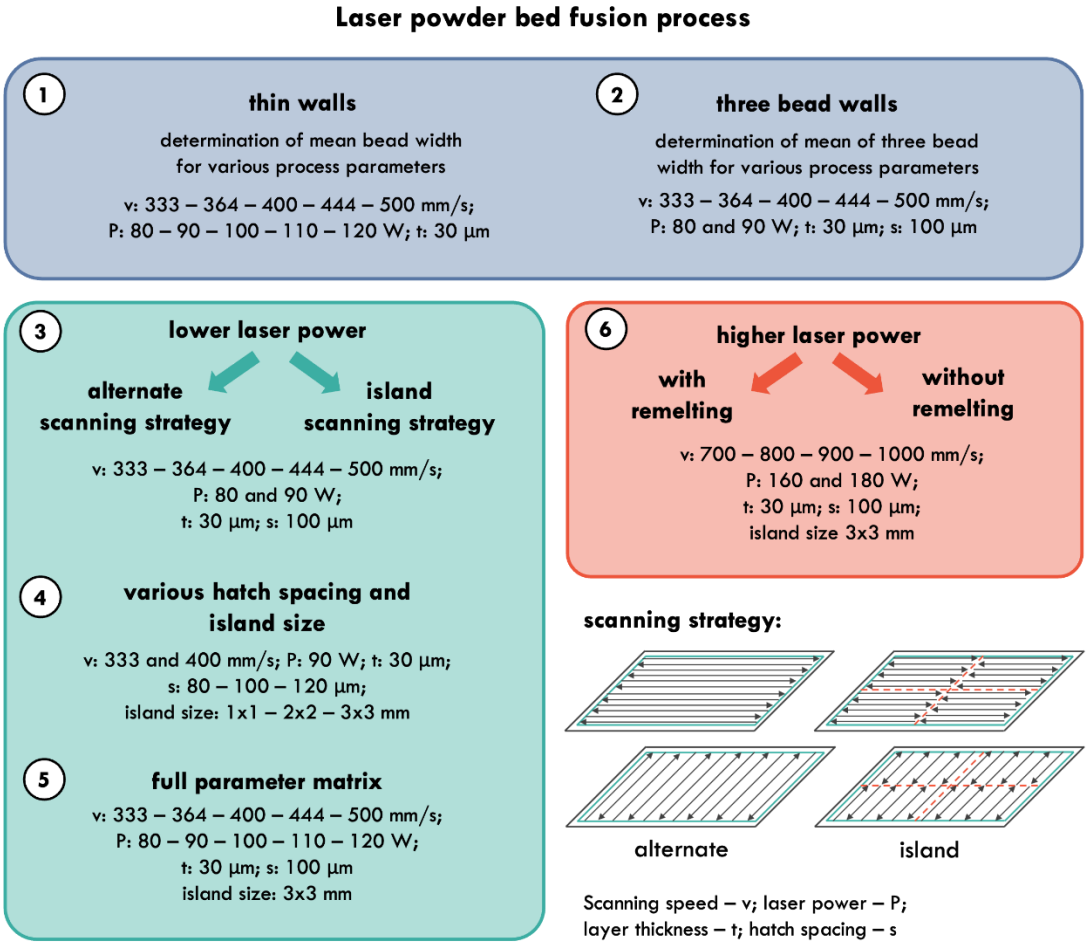

Fig. 6.6. *Steps of L-PBF process of the* $Fe_{45}Cr_{15}Mo_{14}C_{15}B_6Y_2Ni_3$ *alloy*

All conducted processes for Fe-Cr-Mo-C-B-Y-Ni metallic glass were performed for thin walls using 3x3x3 mm cuboid model and for the solid samples 6x6x4 mm. According to the Figure 6.6 firstly, to determine the right hatch spacing s thin walls were manufactured. During the process several parameter variations with laser power raging between 80 and 120 W and scanning speed between 333 and 500 mm/s and 30 µm layer thickness were implemented. After the conducted single bead walls thickness measurements (Fig. 6.7), the hatch spacing s for the following processes was chosen to be equal to 100 µm.

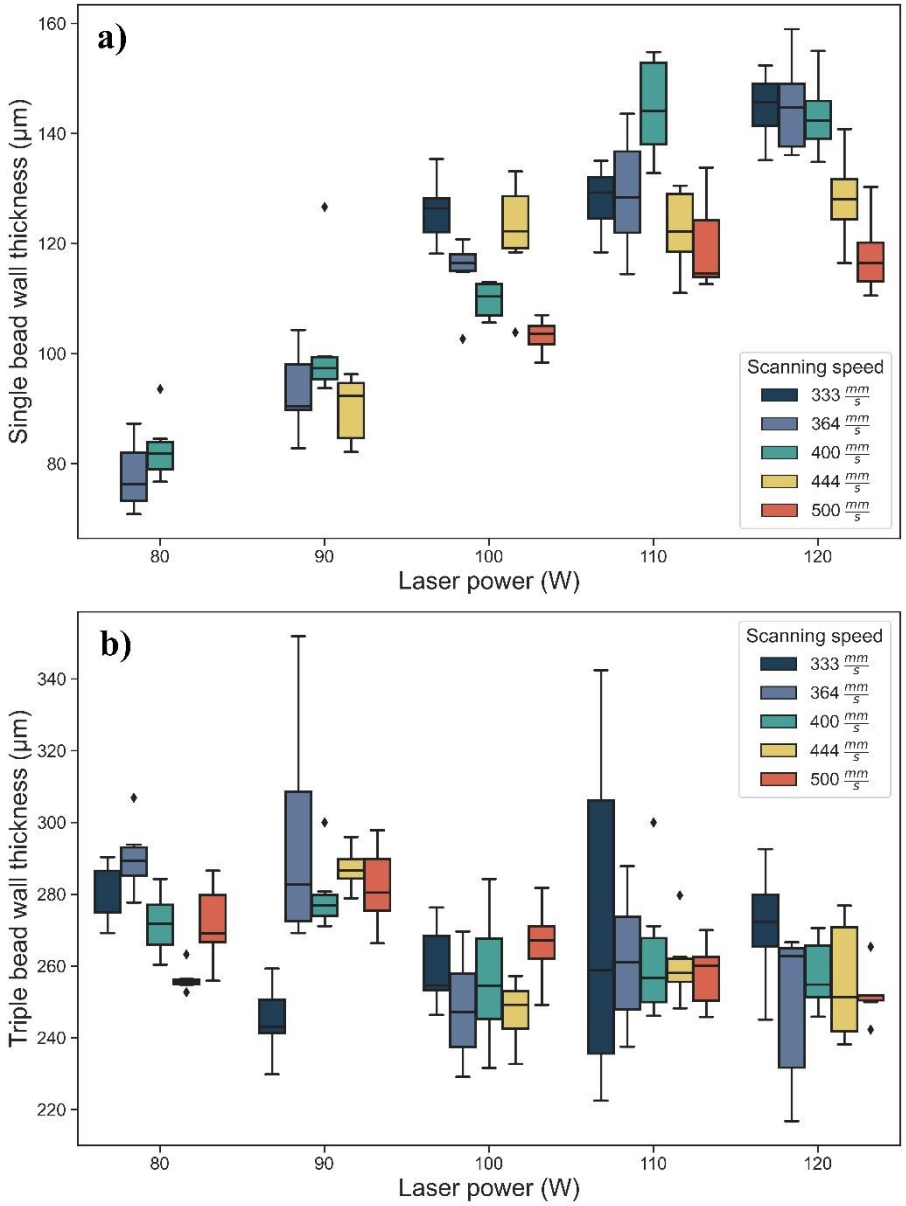

Fig. 6.7. *a) Single bead wall and b) triple bead wall thicknesses of samples produced with various process parameters*

Subsequently, a process was conducted to compare two different scanning strategies: alternate and island. For the island scanning strategy, the island size was set to 3x3 mm and in the next layer the 90° rotation was used (island-alternate scanning strategy). As before, variable parameters were used for scanning speeds (333 to 500 mm/s) and laser powers (80 and 90 W). Considering the surface of the produced samples, a much better surface quality was observed for the island strategy, which was confirmed by the digital defect calculation. The comparison between the surface of samples produced in two different scanning strategies is shown as an example in Figure 6.8.

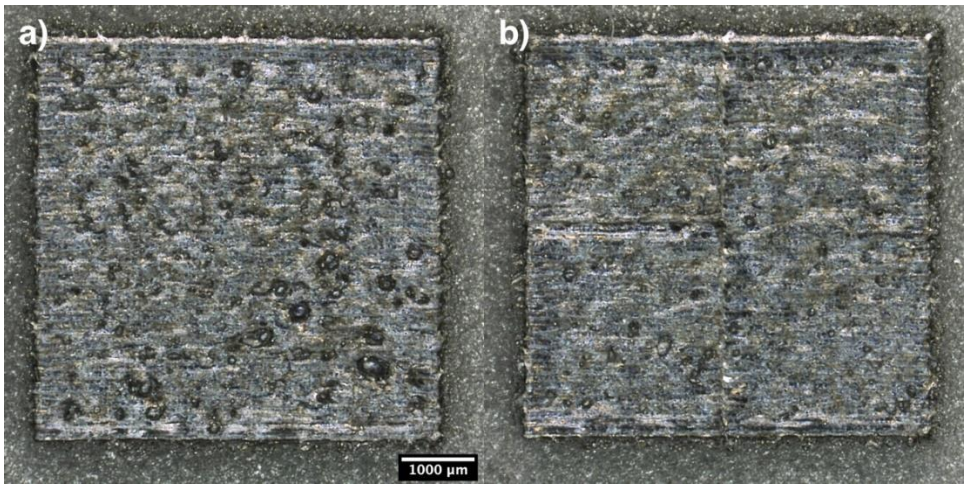

Fig. 6.8. *Surface comparison for samples built with a) alternate and b) island-alternate scanning strategy*

As the following process, for scanning speed 333 and 400 mm/s and for laser power 90 W, various hatch spacings (80, 100, 120 µm) and island sizes (1x1, 2x2, 3x3 mm) were implemented.

Finally, the process with extended laser powers (80, 90, 100, 110, 120 W), scanning speeds (333, 364, 400, 444, 500 mm/s), 30 µm layer thickness, 100 µm hatch spacing, and 3x3 mm island size with 90° rotation in the next layer was conducted. The manufactured in this process samples were investigated for porosity and microstructure characterization.

Due to the conducted porosity examination, it was observed that the pore content was significantly lower in the overlapping (re-melted) area of the islands. Therefore, a process with higher laser powers (160 and 180 W), higher scanning speeds (700, 800, 900, 1000 mm/s), and implemented re-melting was carried out. The samples were manufactured with and without re-melting and the other process parameters were set as in the case of previous processes.

6.4. Porosity

The porosity measurements were conducted on the polished and unetched cross-sections of the samples. During the observations, each sample was photographed in three random areas. After this, the pictures were digitally processed to calculate the pore shares.

The determined porosity distributions for the process with lower laser power values and lower scanning speeds are presented in Figure 6.9. The obtained test results allowed the indication of relatively high porosity in the produced samples. Nevertheless, it was observed that for almost all scanning speeds, except for 500 mm/s, the lowest porosity values were obtained using a 120 W laser power value. The 333 mm/s scanning speed and 120 W laser power resulted in the lowest median porosity (2.78%), while the highest, 8.55%, was obtained for the 364 mm/s scanning speed and the 100 W laser power. Depending on the increase in laser power, the highest porosity decrease was observed for the 333 mm/s scanning speed.

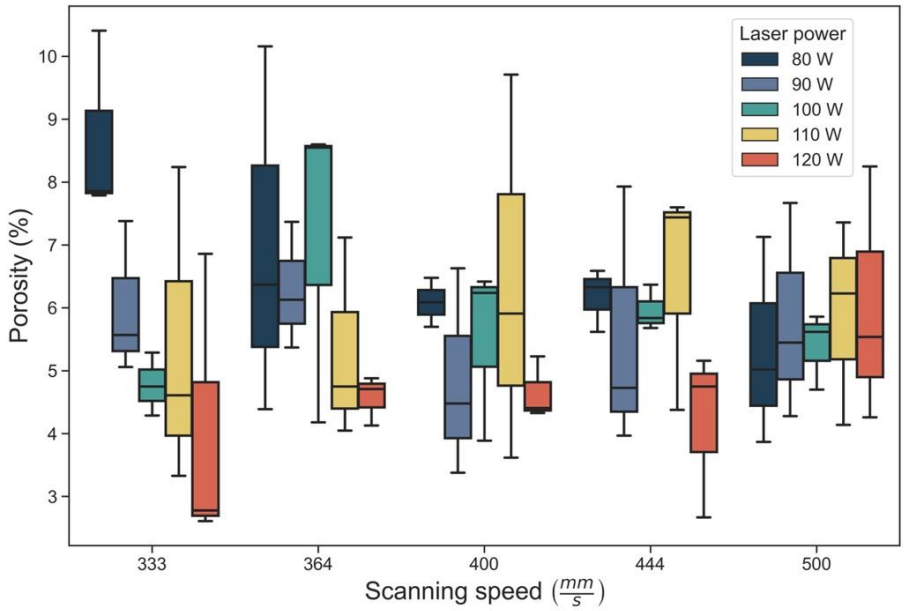

Fig. 6.9. *Porosity shares of samples manufactured with varying laser powers and scanning speeds*

Taking into consideration the aforementioned dependencies, the following L-PBF process was performed with greater laser powers and higher scanning speeds to ensure that the manufactured samples did not overheat. In addition, another set of samples using the same process parameters and implementing re-melting

was performed. The results of the measured porosity distributions are shown in Figure 6.10. For both sample sets prepared with different laser powers and with and without re-melting, a slight increase in porosity was observed for 900 mm/s scanning speed. The scanning speed decrease resulted in a porosity decrease. For a series of samples prepared with a 160 W laser power, slightly higher porosity was observed in the samples where re-melting was supplied. In the case of samples produced using a 180 W laser power, slightly lower porosity values were obtained for samples with applied re-melting. The lowest porosity medians of 1.26% were measured in specimens manufactured with 700 mm/s scanning speed and 160 W laser power, and 180 W with and without re-melting.

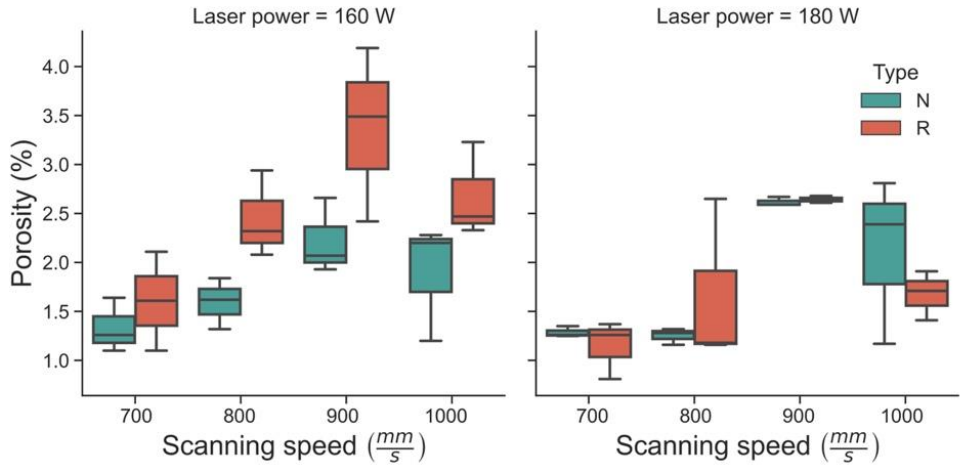

Fig. 6.10. *Porosity comparison between samples produced with (R) and without (N) re-melting using different scanning speeds (700, 800, 900, 1000 mm/s) and laser powers (160 and 180 W)*

6.5. Microstructure characterization

For light microscopy examination, the first series of samples were subjected to the etching process. Nevertheless, the crystal structures were not revealed, indicating their fully amorphous nature. Fig. 6.11 shows cross-sections of samples produced with two different scanning strategies. Smaller amounts of discontinuities in the structure were observed for samples prepared using the island-alternate strategy. Due to numerous cracks and the preparation process, fragments of the samples were chipped. Most often, they were rectilinear. Such an area is marked in Figure 6.11b.

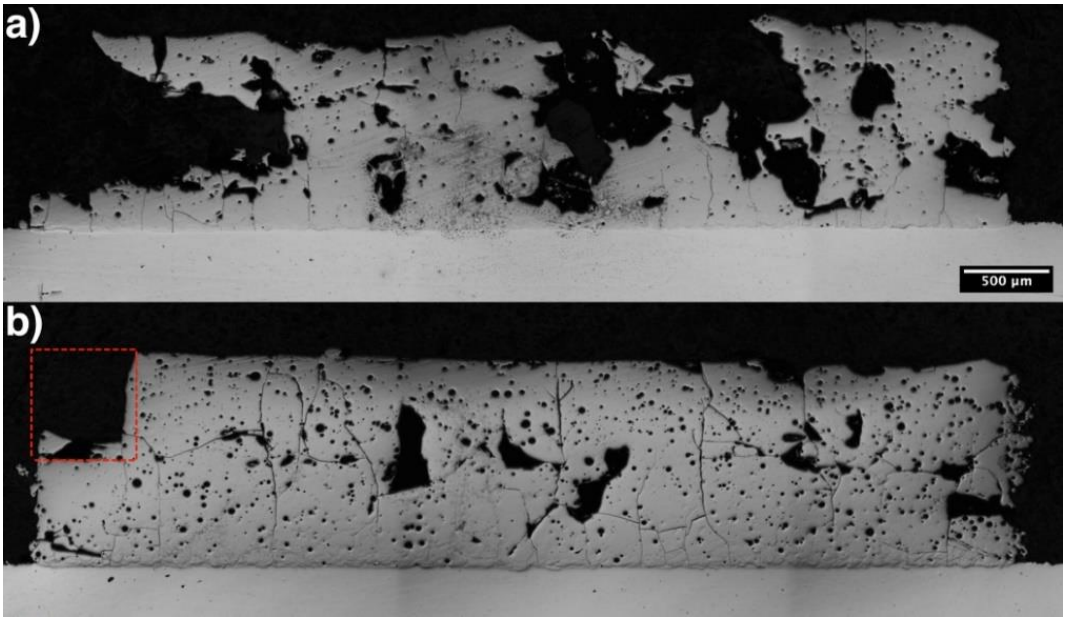

Fig. 6.11. *a) Alternate and b) island-alternate scanning strategy comparison for samples produced with 364 mm/s scanning speed and 90 W laser power*

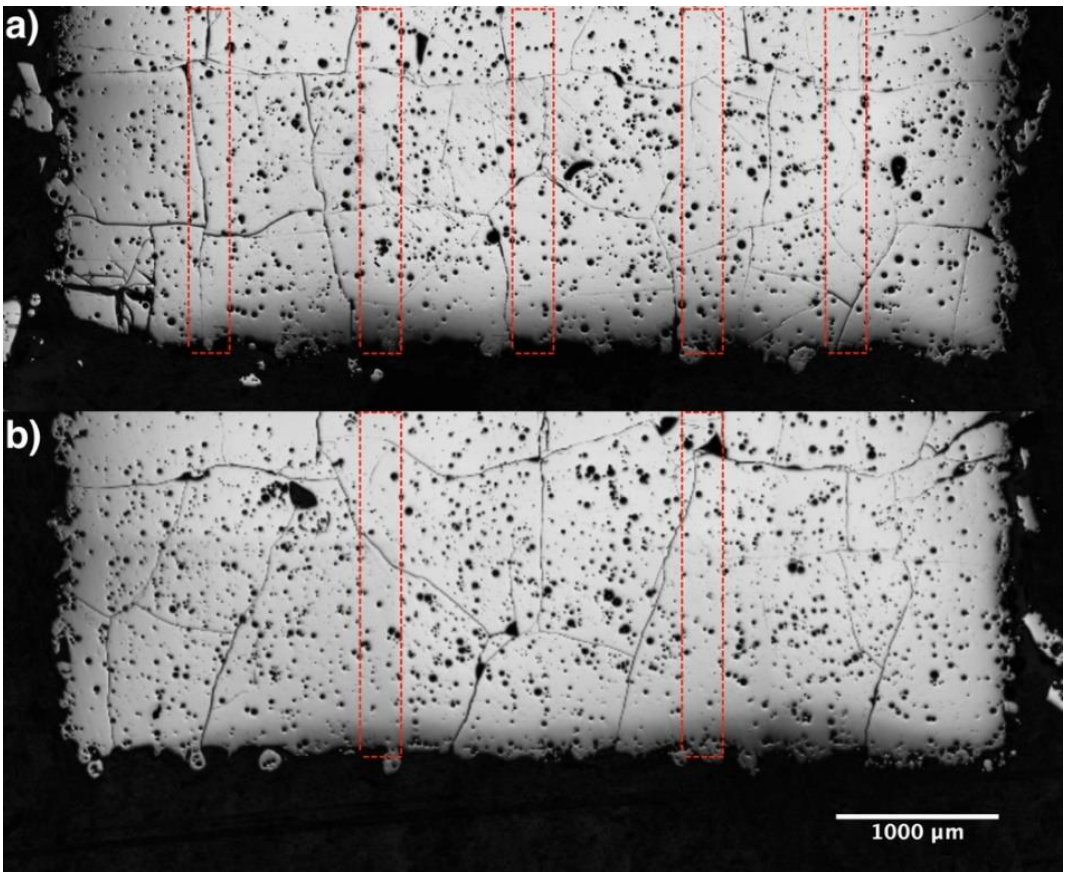

Fig. 6.12. *Samples manufactured with a) 1x1 mm and b) 2x2 mm island sizes, 364 mm/s scanning speed, and 90 W laser power*

Due to fewer structure discontinuities and better surface quality of the samples produced using the island-alternate scanning strategy, it was also used in subsequent processes. One of the parameters that can change for this strategy is the size of the islands. Fragments of cross-sections of samples produced with island sizes of 1x1 and 2x2 mm are shown in Figure 6.12. During the tests, it was observed that in the case of an island size of 1x1 mm, cracks were most often initiated at the border of the islands, which can be seen in Figure 6.12a. Taking into account the number and nature of the cracks, it can be concluded that in the case of the size of the island 1x1 mm, the cracks ran more regularly, creating segments similar in size to the size of the island, which directly translates into a more significant number. In the case of the sample prepared with an island size of 2x2 mm, the fractures were more random. In both cases, smaller amounts of pores were observed at the borders of the islands, as indicated in Figure 6.12.

As before, no crystalline phases were found in light microscopy observations for a series of samples with extended laser current values up to 120 W. Selected samples were XRD tested to determine the phase composition. The results of the conducted tests are presented in Fig. 6.13. Only the amorphous phase was found for all five samples, which is confirmed by the characteristic halo reflections around 42.5 degrees.

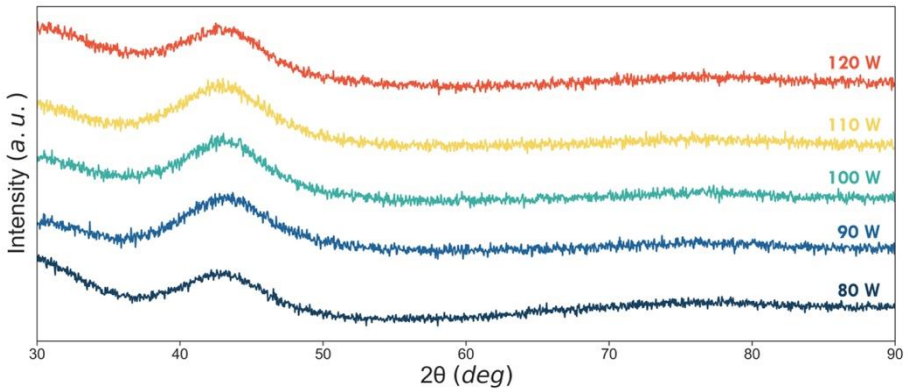

Fig. 6.13. *XRD spectra from samples produced in island-alternate 3x3 mm scanning strategy with 444 mm/s scanning speed and 80 to 120 W laser power*

For verification, a selected sample (90 W laser power and 333 mm/s scanning speed) was examined using transmission electron microscopy. During the tests, a homogeneous structure was observed (Fig. 6.14a). However, the occurrence of

the characteristic blurry halo ring on selected area electron diffraction confirmed the amorphous nature of the structure (Fig. 6.14b).

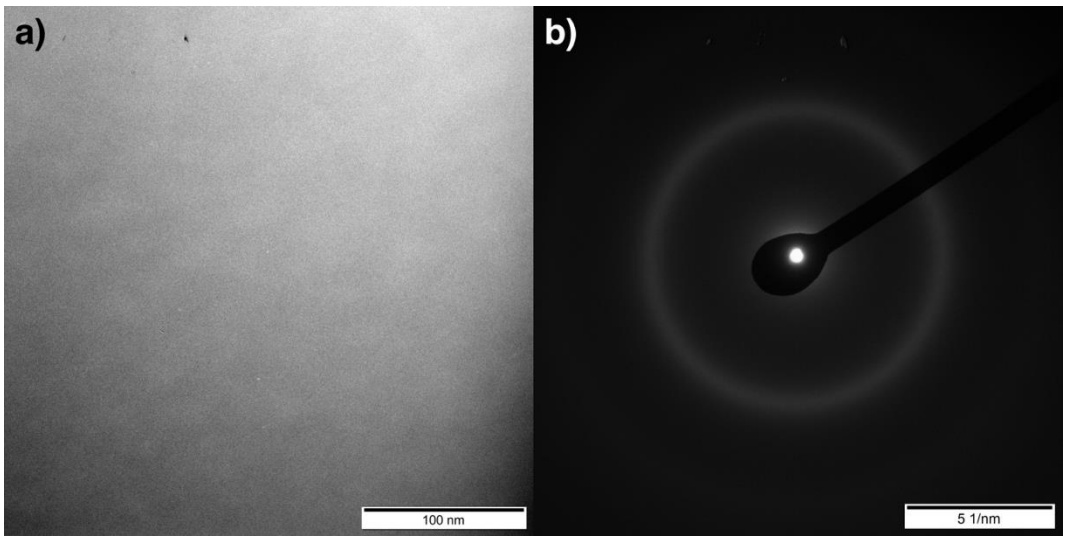

Fig. 6.14. *TEM bright-field image (a) and selected area electron diffraction pattern (b) of sample manufactured in L-PBF technology using 90 W laser power and 333 mm/s scanning speed*

Samples produced with higher laser powers and samples with re-melting were subjected to observations using scanning electron microscopy. The sample produced with the scanning speed and the laser power of 1000 mm/s and 160 W, respectively, was characterized by a homogeneous structure, as indicated by the homogeneous contrast (Fig. 6.15a). Slight differences in contrast were observed in some areas, indicating segregation of the elements during manufacture. In the case of a sample prepared with the same process parameters and the additional use of re-melting, small fractions of phases were observed, which are shown and marked in Figure 6.15b. The described phases occurred most often in clusters with regular intervals. The spaces between the clusters showed uniform contrast. Similarly, in Figures 6.15c and 6.15d, samples produced with a scanning speed of 700 mm/s, a laser power of 160 W, and additionally applied re-melting are presented. The obtained structures were characterized by variable contrast. As before, phases with a dark shade were observed. These phases in some areas took the form of dendrites. Based on the differences in contrast, it was possible to observe the laser beam's scanning position and the melt pool's shape. Structurally, the samples produced with different scanning speeds differed significantly from

each other, and the applied re-melting resulted in the appearance of crystalline phases.

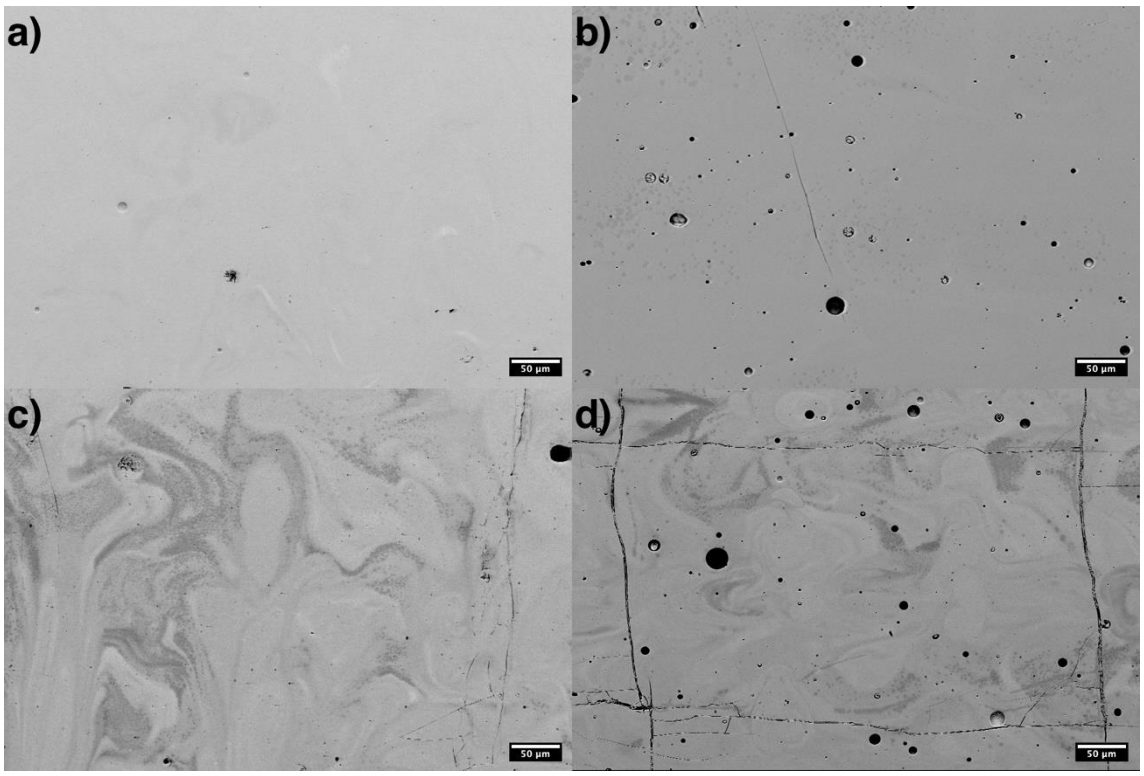

Fig. 6.15. *Scanning electron microscopy micrographs of samples produced in L-PBF technology using 160 W laser power, 1000 mm/s (a, b) or 700 mm/s (c, d) scanning speed and with (b, d) or without (a, c) re-melting*

In order to determine the qualitative phases present, XRD tests were carried out. Four samples were tested, for which the spectra obtained are shown in Figure 6.16. The samples were produced with the same laser power of 160 W and various scanning speeds of 1000 mm/s and 700 mm/s (marked in Figure 6.16, a and b, respectively). In addition, re-melting was used for the same values of process parameters. For the sample prepared without re-melting and the scanning speed of 1000 mm/s, no sharp reflections indicating the presence of crystalline phases were observed. A sample with the same parameters, produced with additional re-melting in the spectrum, had mainly amorphous halos, while the low-intensity reflections indicate the presence of a small proportion of the crystalline phase, identified as the intermetallic $(Fe, Cr)_{23}(C, B)_6$ phase. The sample prepared with a scanning speed of 700 mm/s and without re-melting had some degree of amorphism. The occurring reflections came from the intermetallic $(Fe, Cr)_{23}(C, B)_6$

phase. Compared to the previously described sample, the share of the crystalline phase was significantly higher. A sample with the same process parameters and re-melted underwent more advanced crystallization. As in the previous cases, the presence of the $(Fe, Cr)_{23}(C, B)_6$ phase was observed in its structure. In addition, the $Fe_{11}Mo_6C_5$ and $Fe_{21}Mo_2C_6$ phases occurred.

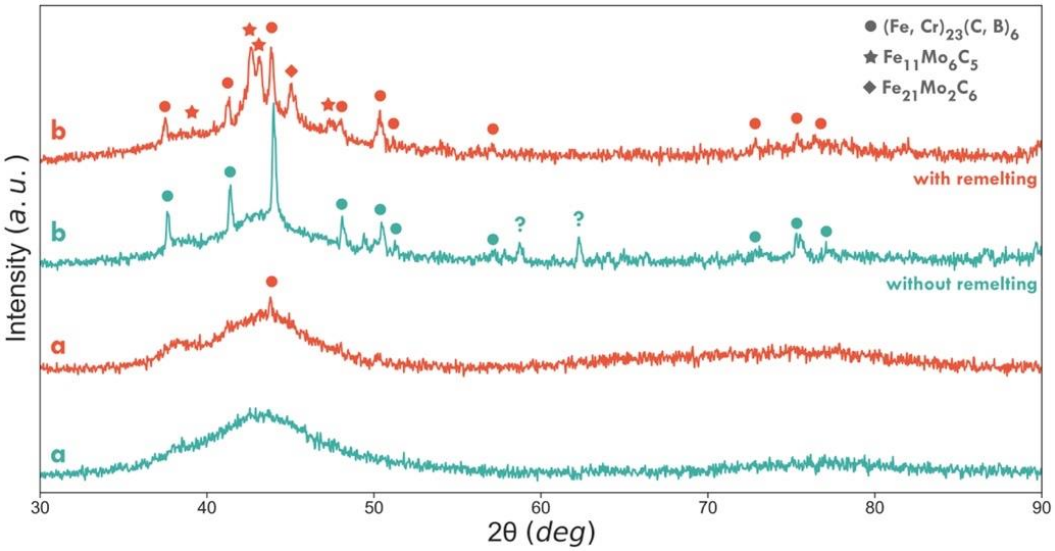

Fig. 6.16. *X-Ray diffraction spectra obtained from samples produced with 1000 mm/s (a) and 700 mm/s (b) scanning speed and 160 W laser power. Samples produced with re-melting are colored orange, and without re-melting, turquoise*

6.6. Hardness

Hardness tests were carried out for two series of samples produced in the L-PBF technology. The results of the measured hardness for samples produced with lower laser power values and lower scanning speeds are shown in Figure 6.17. The obtained values are, in most cases, similar and do not differ significantly. In the case of samples produced with a scanning speed of 364 mm/s, an increasing trend in hardness was observed concerning increasing laser powers. The same was true for samples produced using a laser current of 120 W and decreasing scanning speeds. The highest hardness (median 1196 HV1) had a sample produced using a laser power of 120 W and a scanning speed of 333 mm/s. The sample with the lowest hardness (median 1105 HV1) was obtained using 120 W laser power and a scanning speed of 500 mm/s.

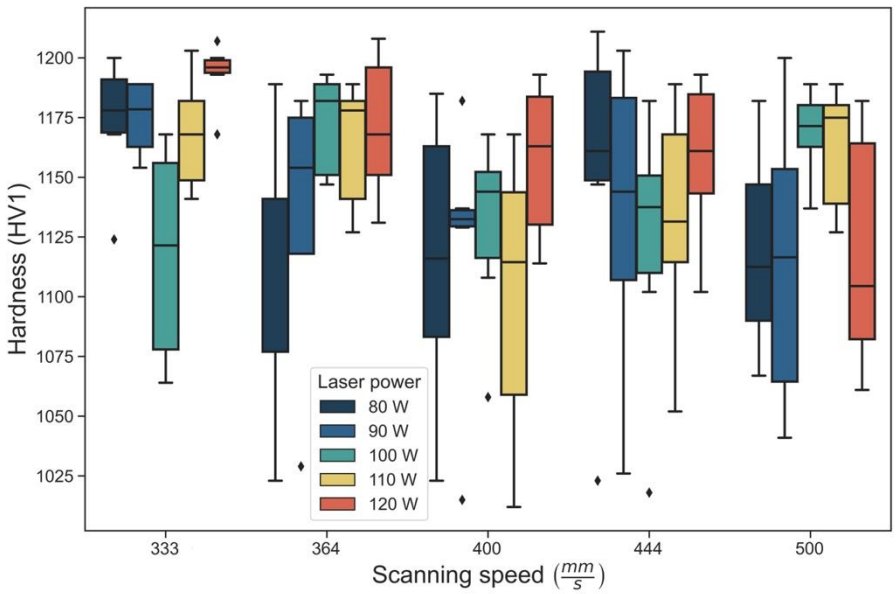

Fig. 6.17. Hardness values of samples produced with lower laser powers and lower scanning speeds

In the case of the second series of samples, produced with higher scanning speeds and higher laser powers, the hardness measurements allowed to observe significant differences in hardness for samples produced with re-melting (Fig. 6.18). Large scatters of hardness values were observed in the case of samples produced without re-melting, whereas in the case of samples produced using re-melting, these values were very close to each other. The maximum hardness (median 1279 HV1) was measured for a sample produced using re-melting, ascanning speed of 700 mm/s, and a laser power of 160 W.

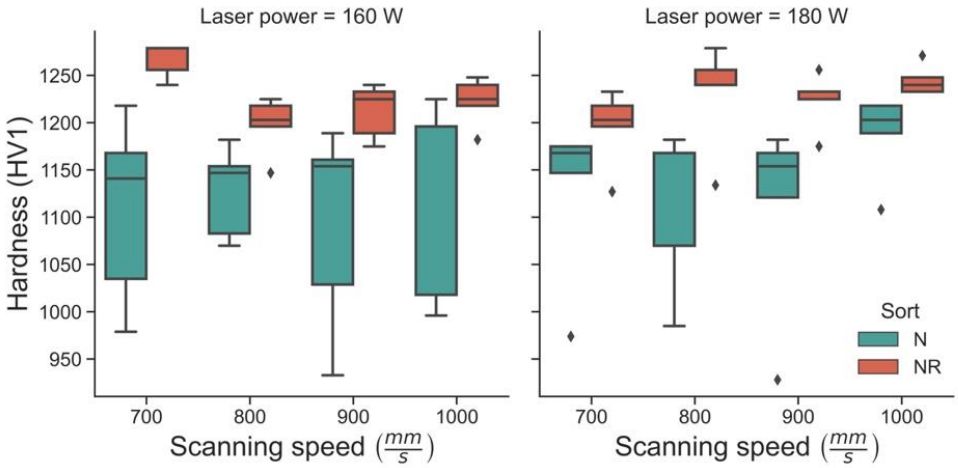

Fig. 6.18. Hardness comparison between samples produced with (NR) and without re-melting (N)

6.7. Discussion

The tests of samples produced in the L-PBF technology with various process parameters made it possible to understand the impact of specific process parameters on processability, structural changes, and hardness of $Fe_{45}Cr_{15}Mo_{14}C_{15}B_6Y_2Ni_3$ alloy. The powder used in the process, due to the presence of elongated droplet particles and often extended shape, negatively affected the uniform distribution of the powder layer at the initial phase. In addition, the observed high porosity of the powder may have contributed to the increase in the existing porosity in the produced samples [92,108]. The powder, after gas atomization, was characterized by an amorphous structure, which indicates a high glass-forming ability. The low reflectivity of the powder, which affects the amount of energy absorbed, made it possible to use lower laser currents to melt the powder layer and the previously created layers, guaranteeing a permanent connection.

The use of different process parameters, in this case, different laser powers and different scanning speeds, played a significant role in obtaining low porosity samples. The low laser powers suggested in work [154] for metallic glasses followed relatively high pore shares (3-8%). Taking into account the entire parameters matrix, laser powers of 80-120 W and scanning speeds of 333-500 mm/s, and obtaining energy density values in the range of 53.3-120.0 J/mm^3, the lowest median porosity (2.78%) was obtained for the highest energy density. In the case of samples produced with higher values of laser powers (160 and 180 W) and higher scanning speeds (700-1000 mm/s), obtaining laser energy densities in the range of 55.3-85.7 J/mm^3, samples with significantly lower porosity were produced. The sample's lowest porosity (1.26%) was achieved using a scanning speed of 700 mm/s and a laser power of 160 W, at an energy density of 76.2 J/mm^3. In relation with the above, it is noteworthy that often energy density does not prompt into porosity reduction. Based on the conducted research, it can be concluded that laser powers or the ratio of scanning speed to laser power have a greater impact [99]. The conducted process with additional re-melting did not directly show any advantages influencing the reduction of porosity.

The use of two different scanning strategies made it possible to compare their effects on the samples produced. The samples prepared in the alternate scanning

strategy showed a greater number of defects, mainly cracks, which caused sample segments to chip during the preparation for observation. The use of the island-alternate scanning strategy limited the formation of cracks and improved the overall quality of the samples observed in the cross-section. In addition, using different island sizes, an increase in the number of cracks was observed with decreasing dimensions. The cracks appeared mainly in the areas of island overlap. Based on the observations, it was found that the size of the islands should be in the range of 2-3 mm. The use of the island scanning strategy and its good effect, caused by the reduction of thermal stresses, on the manufactured elements is confirmed in the literature [115,157]. An increase in the number of cracks was observed in the samples produced by additional re-melting.

Considering the kinetics and dynamics of crystallization of the $Fe_{45}Cr_{15}Mo_{14}C_{15}B_6Y_2Ni_3$ bulk metallic glass, the first phase crystallizing from the amorphous state due to the supplied heat is the phase $(Fe, Cr)_{23}(C, B)_6$. Samples prepared with lower values of laser powers (90-120 W) and lower scanning speeds (333-500 mm/s) were characterized by an amorphous structure throughout the volume, however, a relatively high level of porosity was obtained, as mentioned above. Increasing the laser power (160 W) and the scanning speed (1000 mm/s) still resulted in obtaining an amorphous structure and a simultaneous reduction of porosity to 2.2%. While maintaining the same value of laser powers and decreasing the scanning speeds, in the structure, the amount of the intermetallic $(Fe, Cr)_{23}(C, B)_6$ phase increased, accompanied by a decrease in porosity. In addition, the applied re-melting caused the crystallization or growth of the primary phase and initiated the formation of subsequent phases. Re-supply of thermal energy led to increased diffusion of atoms, which led to the formation of crystallization nuclei and, in the case of crystallized high-melting phases, to their growth [147].

Iron-based metallic glasses are characterized by high hardness, which is confirmed by the conducted tests. For a series of samples with lower laser powers (90-120 W) and lower scanning speeds (333-500 mm/s), the microhardness was in the range of 1105-1196 HV1. Differences in hardness occurred despite the obtained amorphous structure, confirmed by XRD examinations. The reason for the

differences in the obtained hardness may be structural aspects as well as those resulting from technological defects. Pores and cracks present in the material could lead to a false assessment of hardness during the measurement. Nevertheless, the measurements were carried out in areas free of pores and cracks. Considering structural factors in metallic glasses, there may be local differences in hardness due to the growth and distribution of medium-range order clusters [158]. The use of high laser powers and decreasing scanning speeds caused a slight decrease in hardness, despite the increasing share of the hard intermetallic phase $(Fe, Cr)_{23}(C, B)_6$. Using re-melting, an increase in hardness was observed for all samples. The highest hardness (1279 HV1) was achieved for the laser power and scanning speed of 160 W and 700 mm/s and re-melting. The sudden increase in hardness was caused by the appearance of a molybdenum-rich phase [159].

The L-PBF process, due to the wide possibilities of changing parameters, creates great opportunities in the context of the obtained structures and mechanical properties. Proper and conscious selection of process parameters effectively reduces the number of defects in the manufactured parts. Nevertheless, most publications on iron-based metallic glasses still highlight the cracks formation problem during the process. Considering the type of cracks caused by thermal stresses, it would be possible to reduce them during the process by heating the working plate or using an additional laser. Both of these possibilities will result in a reduction in the cooling rate, thus reducing shrinkage and consequent stress reduction. In the case of metallic glasses with high glass-forming ability, the reduction of the cooling rate should not significantly affect the amorphous structure obtained. For this type of material, the use of a cooling rate below 10^3 K/s results in the formation of an amorphous structure. In the case of the first method of reducing thermal stresses during the process, the use of heating the working plate resulted in a reduction of stresses by 40% at a temperature of 160 °C [160]. In the case of the described metallic glass, it would be possible to use heating to higher temperatures, in the range of 350-450 °C, due to the high glass transition temperature. The second method, using an additional laser, selectively reduces the temperature gradient. It was successfully used for materials with a high tendency to crack during manufacturing in the L-PBF technology [161].

In this method, a second laser with a larger spot diameter following the main beam is used, which is correlated with the movement of the main beam. The selective nature of this method reduces the risk of constantly maintaining the manufactured elements at high temperatures, which occurs during the heating of the building platform and powder bed.

7. Summary

Additive manufacturing, which includes the laser powder bed fusion technology, changes the view on the production. The mechanical properties obtained, the possibility of shaping the structure, or great freedom concerning the geometries of the manufactured elements are just a few of its many advantages. The wide range of process parameters underlines this technology's versatility in relation to various materials. Due to the small size of the melt pool and the layer-by-layer nature of the process, high cooling rates are achieved, enabling the formation of amorphous structures of metallic glasses. Nevertheless, in-depth knowledge of the impact of process parameters and their intended use will determine the manufactured elements' usefulness. The main research objective of this work is to evaluate the possibility of producing two types of iron-based metallic glasses with low and high glass-forming abilities using the laser powder bed fusion method and to determine the effect of selected parameters of the L-PBF process on the microstructure, defect formation, and hardness. The alloys studied in the dissertation were produced in the L-PBF technology for the first time. Until now, in the literature, ribbons or rods were produced from them, which limited their subsequent use. Referring to the Technology Readiness Levels, the first four levels have been implemented in this dissertation, covering basic principles, technology concept, experimental proof of concept, and laboratory validation.

Powder quality

In the L-PBF process, the powder, which is the feedstock, should be of satisfactory quality. Poor-quality powder will contain defects that may be compounded during the process. The powder produced from the $Fe_{79}Zr_6Si_{14}Cu_1$ alloy mainly had a spherical shape and fine satellite particles characteristic of gas atomization. The chemical composition was close to the reference one. During the atomization process, the powder crystallized, and the identified phases were α-Fe(Si) solid solution, $Fe_{23}Zr_6$ intermetallic phase, and trace amounts of $FeZr_2$ and $Fe_{16}Si_7Zr_6$. No pores were observed in the cross-sections of the powder. Due to the soft magnetic properties of the material, there were problems with the uniform

formation of the first layers, but as the process continued, they were homogeneous. The reflectivity of the powder for the wavelength of 1070 nm was 16.2%. On the other hand, the $Fe_{45}Cr_{15}Mo_{14}C_{15}B_6Y_2Ni_3$ powder had a developed surface. Additionally, there were stretched drop particles that negatively affected theflowability. After atomization, the powder had an amorphous structure. The chemical composition of the powder differed from the reference composition for both carbon and iron. The cross-section of the powder revealed the present porosity. The measured reflectivity for the wavelength of 1070 nm was 14.0%. In the initial phase of the research, the uniform distribution of the powder was complex due to the presence of elongated droplet-shaped particles, but an improvement was observed after multiple sieving.

Process parameters, volumetric energy density, and their impact on porosity

In addition to mechanical properties, the decisive criterion for the use of manufactured elements is to obtain low porosity (<1%). High proportions of pores create discontinuities and thus reduce the accurate cross-section. In addition, pores over 30 μm in diameter appearing in the material may be crack initiation sites [124]. The general statement appearing in the works on the L-PBF technology that porosity depends on the volumetric density of the supplied energy (J/mm^3) is not always correct. In the case of the $Fe_{79}Zr_6Si_{14}Cu_1$ alloy, the obtained porosities, at variable powers and scanning speeds, decreased exponentially with the increase of the supplied energy density. The lowest proportion of pores (0.4-1.9%) for this material was observed using a laser power of 180 W and scanning speeds in the range of 700-1000 mm/s. On the other hand, for the $Fe_{45}Cr_{15}Mo_{14}C_{15}B_6Y_2Ni_3$ alloy, using low laser powers (80-110 W), the obtained pore shares remained at a relatively high level (8.6-4.5%) despite the changing volumetric energy densities (53-110 J/mm^3). No general relationship between the applied energy density and the obtained porosity could be observed. In this case, the applied laser powers turned out to be more significant. With a doubling of the laser powers from 80 W to 160 W and maintaining the same values of the volumetric energy density, a decrease in porosity from 5.0% to 2.2% was observed. Finally, using the scanning speed of 700 mm/s for 160 and 180 W laser powers, the porosity was reduced to

1.3%. Therefore, increases in the volumetric energy density of the laser will not always be accompanied by a decrease in the pore share if the sufficient laser power is not applied.

Porosity type

With regard to the type of pores, two types of pores were observed in the $Fe_{79}Zr_6Si_{14}Cu_1$ alloy. When low laser power and high scanning speeds were used, porosity with irregular shapes containing powder particles prevailed, resulting from the lack of melting of the powder layer and the previously formed layers. However, with the increased laser power, its occurrence was successfully reduced, and the emerging pores took on a spherical shape, characteristic of gas porosity. For this material, the primary type of porosity was lack of fusion, the values of which below 3% were achieved using laser powers above 160 W and scanning speeds in the range of 700-1000 mm/s. It is worth mentioning that the highest gas porosity among all measured samples was 0.57%. On the other hand, in the $Fe_{45}Cr_{15}Mo_{14}C_{15}B_6Y_2Ni_3$ alloy, most of the pores were gas pores forming clusters. Only when higher laser powers of 160 and 180 W were used changes in the distribution of pore density were observed, affecting their more random location.

Microstructure evolution concerning process parameters

Due to the cyclic nature of the L-PBF process and the changing size of the melt pool, metallic glasses may crystallize during production, depending on the process parameters. High cooling rates are necessary to obtain an amorphous structure, which in this technology can reach up to 10^8 K/s. In order to allow for faster heat dissipation, the components are manufactured directly on the build plate. Nevertheless, the chemical composition of the alloy, which determines the vitrification ability, does not always allow for obtaining an amorphous structure in the entire cross-section. No fully amorphous structure was obtained for metallic glass $Fe_{79}Zr_6Si_{14}Cu_1$ with low glass-forming ability. Using lower laser power (120 W) in the structure, apart from the amorphous phase, α-Fe(Si) solid solution and small amounts of the $Fe_{23}Zr_6$ intermetallic phase occurred. Withincreasing laser power (180 W), there was an increase in the proportion of the

$Fe_{23}Zr_6$ phase and, to a small extent, the crystallization of the $FeZr_2$ phase. In the $Fe_{45}Cr_{15}Mo_{14}C_{15}B_6Y_2Ni_3$ alloy with high glass-forming ability, an amorphous structure was obtained in a wide range of laser powers (80-120 W) and lower scanning speeds (333-500 mm/s). In addition, an amorphous structure was obtained for a laser power of 160 W and a scanning speed of 1000 mm/s. It was the limit value, where the crystallization of the intermetallic phase $(Fe, Cr)_{23}(C, B)_6$ took place while lowering the scanning speed and the constant value of the laser power. A further increase in the laser power resulted in the crystallization of $(Fe, Cr)_{23}(C, B)_6$, $Fe_{11}Mo_6C_5$, and $Fe_{21}Mo_2C_6$ phases. Re-melting the same layer for a laser power of 160 W and a scanning speed of 1000 mm/s resulted in the crystallization of a trace amount of the intermetallic phase $(Fe, Cr)_{23}(C, B)_6$. In the case of an alloy with low glass-forming ability, the crystallization of α-Fe(Si) solid solution is considered desirable, and its use improves the soft magnetic properties.

Hardness

During the L-PBF process, as a result of the supplied energy, diffusion of atoms occurs, affecting the structural changes in the material. Consequently, by changing the process parameters, it is possible to shape the mechanical properties, including hardness. For alloy $Fe_{79}Zr_6Si_{14}Cu_1$, the highest achieved hardness (953 HV1) was obtained for the laser power of 120 W and the scanning speed of 900 mm/s. A decrease in hardness was observed with increasing laser power up to 160 W. On the other hand, there was a jump increase for the laser power value of 180 W. Nevertheless, for this laser power, reduced scanning speeds led to a decrease in hardness. Consequently, the lowest hardness (774 HV1) was obtained for the laser power of 180 W and the scanning speed of 700 mm/s. The decrease in hardness, in this case, could be caused by the increasing shares of the α-Fe(Si) phase with increasing laser power. In alloy $Fe_{45}Cr_{15}Mo_{14}C_{15}B_6Y_2Ni_3$, in the range of laser powers of 80-120 W and scanning speeds of 333-500 mm/s, despite obtaining an amorphous structure, differences in hardness (1105-1196 HV1) were observed, which could be caused by an increase in the medium-range order of clusters as a result of the supplied energy. In turn, both for laser powers of 160 W and 180 W, the hardness decreased with decreasing scanning speeds from 1196 HV1 to 1141

HV1. Additional re-melting of the layer resulted in a hardness increase, reaching the value of 1279 HV1 for the laser power of 160 W and the scanning speed of 700 mm/s. The significant increase in hardness could be caused by the crystallization of the molybdenum-rich phase, in this case, $Fe_{11}Mo_6C_5$ and $Fe_{21}Mo_2C_6$ phases.

Cracks formation

So far, most iron-based metallic glasses produced by the L-PBF technology have been associated with cracking. In all cases, cracking occurred during the process. In alloys $Fe_{79}Zr_6Si_{14}Cu_1$ and $Fe_{45}Cr_{15}Mo_{14}C_{15}B_6Y_2Ni_3$, cracking also occurred, but they differed in the types of cracks. No cracks were observed in alloy $Fe_{79}Zr_6Si_{14}Cu_1$ immediately after the process. In turn, repeated observations three weeks after the process revealed microcracks initiated at the fusion line. The nature of the cracks indicated cold cracking caused by the occurring residual stresses. The type of cracking makes it possible to reduce or eliminate cracks by post-process heat treatment. On the other hand, alloy $Fe_{45}Cr_{15}Mo_{14}C_{15}B_6Y_2Ni_3$ cracked during the process (hot cracking). The cracks most often occurred along the beads and coincided with the applied scanning strategies, which indicates the type of liquation cracks. In this case, the reduction or elimination of cracks should occur during the process, which would enable the heating of the working plate or selective reduction of the temperature gradient by using a second laser beam following the main beam.

A summary of the main research results and a comparison of the two Fe-based alloys produced in the laser powder bed fusion technology are presented in Tab.7.1.

Tab. 7.1. *Comparison of $Fe_{79}Zr_6Si_{14}Cu_1$ and $Fe_{45}Cr_{15}Mo_{14}C_{15}B_6Y_2Ni_3$ alloys produced in L-PBF technology*

		$Fe_{79}Zr_6Si_{14}Cu_1$	$Fe_{45}Cr_{15}Mo_{14}C_{15}B_6Y_2Ni_3$
Powder quality	sphericity	●	◕
	reflectivity	◔	◔
	layer formation	◕	◑
	porosity	○	◔
	crystallinity	●	○
Samples porosity	low laser power (<120 W)	●	◑
	high laser power (>160 W)	○	○
Samples amorphousness degree	low laser power (<120 W)	◔	●
	high laser power (>160 W)	◔	◕
Cracks formation	cold cracking	◑	–
	hot cracking	–	●
Hardness	–	◕	●
○ very low	◔ low	◑ medium	◕ high	● very high

8. Conclusions

Based on the interpretation and discussion of the results of the research conducted as part of the doctoral dissertation, the final conclusions were formulated:

- The powder microstructure depends on the glass-forming ability. By the low glass-forming ability of the alloy, the powder produced during gas atomization is characterized mainly by crystalline phases, while by high glass-forming ability, the occurred powder structure is amorphous.
- The quality of the powder plays a significant role in the production of L-PBF, particularly its shape. The sphericity of the powder affects the ease of spreading a homogeneous powder layer. On the other hand, the presence of elongated or droplet-like powder particles causes difficulties during layering. In addition, a powder with a high pore content can negatively affect the porosity of the manufactured components.
- The use of the island-alternate scanning strategy has a positive effect on the reduction of defects in manufactured elements compared to the alternate strategy.
- The size of the island in the island-alternate strategy affects the number of cracks occurring, as the island boundaries may be the place of crack initiation.
- The crystallization of amorphous alloys during production by the L-PBF method depends on their glass-forming ability. The use of even low laser power in the case of metallic glasses with low GFA can lead to their crystallization.
- In alloys with low glass-forming ability, the melt pool sizes obtained are too large to allow for sufficiently rapid cooling to obtain an amorphous structure throughout the entire bead section. In addition, the cyclically supplied thermal energy may cause an increase in the proportion of crystalline phases.

- Metallic glasses with high glass-forming ability, characterized by critical cooling rates lower than 10^3 K/s, in the L-PBF technology can form an amorphous structure in a wide laser power range, up to 160 W.
- The microstructure depends mainly on the applied laser power. An increase in the proportion of crystalline phases accompanies the increasing laser power.
- Volumetric energy density is not always an objective value based on which process parameters should be selected to obtain low porosity or amorphous structure in manufactured parts.
- The porosity depends mainly on the applied laser power and decreases with its increase. With the use of high laser power and compensation with the scanning speed, it is possible to obtain a high relative density.
- Low laser powers lead to a lack of fusion porosity, while high laser powers can cause keyhole gas porosity.
- Due to thermal stresses caused by volumetric shrinkage and linear thermal expansion, cold cracking may occur after the L-PBF process. Cracks of this type could be eliminated by stress-relieving heat treatment.
- Due to local melting and thermal stress caused by the temperature gradient during the L-PBF process, liquation cracking may occur. In order to reduce or eliminate cracks, it would be possible to additionally heat the powder bed or use an additional laser beam following the main beam, thus reducing the differences in the temperature gradient and consequently lowering thermal stresses.
- Depending on the type of metallic glasses and the crystallization kinetics, the hardness may increase or decrease with increasing laser power values. Most often, it depends on the type of the primary phase.

The processability of metallic glasses in laser powder bed fusion technology is poor due to the low plasticity of these materials at ambient temperature. For this reason, micro-cracks appear during or after the process due to thermal stresses. Referring to the obtained structures and hardness, the L-PBF technology can be an alternative method for producing metallic glasses. However, to reduce or

eliminate cracks, it is necessary to undertake further research on the reduction of thermal stresses by heating the built plate or selective heating with an additional laser beam and post-processing heat treatment.

Bibliography

[1] P. Duwez, R.H. Willens, W. Klement, Continuous series of metastable solid solutions in silver-copper alloys [19], J. Appl. Phys. 31 (1960) 1136–1137. https://doi.org/10.1063/1.1735777.

[2] W. Klement, R.H. Willens, P. Duwez, Non-crystalline structure in solidified Gold-Silicon alloys, Nature. 187 (1960) 869–870. https://doi.org/10.1038/187869b0.

[3] P.B. Hirsch, A. Howie, R. Nicholson, D.W. Pashley, M.J. Whelan, L.L. Marton, Electron Microscopy of Thin Crystals, Nature. 197 (1977) 438.

[4] P.G. Debenedetti, T.M. Truskett, C.P. Lewis, F.H. Stillinger, Theory of supercooled liquids and glasses: Energy landscape and statistical geometry perspectives, Adv. Chem. Eng. 28 (2001) 21–79. https://doi.org/10.1016/s0065-2377(01)28003-x.

[5] D. Turnbull, Under What Conditions Can A Glass Be Formed?, Contemp. Phys. 10 (1969) 473–488. https://doi.org/10.1080/00107516908204405.

[6] C.A.Angell, Formation of Glasses from Liquids and Biopolymers, Science (80-.). 267 (1995) 1924–1935.

[7] E.A. Abou Neel, J.C. Knowles, Biocompatibility and other properties of phosphate-based glasses for medical applications, Woodhead Publishing Limited, 2008. https://doi.org/10.1533/9781845695477.1.156.

[8] H.W. Sheng, W.K. Luo, F.M. Alamgir, J.M. Bai, E. Ma, Atomic packing and short-to-medium-range order in metallic glasses, Nature. 439 (2006) 419–425. https://doi.org/10.1038/nature04421.

[9] H. Lou, Z. Zeng, F. Zhang, S. Chen, P. Luo, X. Chen, Y. Ren, V.B. Prakapenka, C. Prescher, X. Zuo, T. Li, J. Wen, W.H. Wang, H. Sheng, Q. Zeng, Two-way tuning of structural order in metallic glasses, Nat. Commun. 11 (2020). https://doi.org/10.1038/s41467-019-14129-7.

[10] E. Ma, Tuning order in disorder, Nat. Mater. 14 (2015) 547–552. https://doi.org/10.1038/nmat4300.

[11] Y.Q. Cheng, J. Ding, E. Ma, Local Topology vs. atomic-level stresses as a measure of disorder: Correlating structural indicators for metallic glasses, Mater. Res. Lett. 1 (2013) 3–12. https://doi.org/10.1080/21663831.2012.722759.

[12] J.F. Löffler, Bulk metallic glasses, Intermetallics. 11 (2003) 529–540. https://doi.org/10.1016/S0966-9795(03)00046-3.

[13] A. Inoue, High Strength Bulk Amorphous Alloys with Low Critical Cooling Rates, Mater. Trans. JIM. 36 (1995) 866–875. https://doi.org/10.2320/matertrans1989.36.866.

[14] A. Takeuchi, A. Inoue, Quantitative evaluation of critical cooling rate for metallic glasses, Mater. Sci. Eng. A. 304–306 (2001) 446–451. https://doi.org/10.1016/S0921-5093(00)01446-5.

[15] A. Inoue, Stabilization of metallic supercooled liquid and bulk amorphous alloys, Acta Mater. 48 (2000) 279–306. https://doi.org/10.1016/S1359-6454(99)00300-6.

[16] A. Inoue, A. Takeuchi, Recent development and application products of bulk glassy alloys, Acta Mater. 59 (2011) 2243–2267. https://doi.org/10.1016/j.actamat.2010.11.027.

[17] H.X. Li, Z.C. Lu, S.L. Wang, Y. Wu, Z.P. Lu, Fe-based bulk metallic glasses: Glass formation, fabrication, properties and applications, Prog. Mater. Sci. 103 (2019) 235–318. https://doi.org/10.1016/j.pmatsci.2019.01.003.
[18] S.S. Jiang, L. Zhu, H. Zheng, Y.G. Wang, Kinetics of non-isothermal crystallization in FeNiPC(Nb) alloys, Thermochim. Acta. 684 (2020) 178481. https://doi.org/10.1016/j.tca.2019.178481.
[19] M.J. Duarte, A. Kostka, J.A. Jimenez, P. Choi, J. Klemm, D. Crespo, D. Raabe, F.U. Renner, Crystallization, phase evolution and corrosion of Fe-based metallic glasses: An atomic-scale structural and chemical characterization study, Acta Mater. 71 (2014) 20–30. https://doi.org/10.1016/j.actamat.2014.02.027.
[20] Q. Dong, P. Song, J. Tan, X.M. Qin, C.J. Li, P. Gao, Z.X. Feng, M. Calin, J. Eckert, Non-isothermal crystallization kinetics of a Fe–Cr–Mo–B–C amorphous powder, J. Alloys Compd. 823 (2020). https://doi.org/10.1016/j.jallcom.2020.153783.
[21] A.K. Gangopadhyay, K.F. Kelton, Prediction of elemental glass-transition temperatures of metals from thermophysical properties of liquids, J. Non-Crystalline Solids X. 2 (2019) 100016. https://doi.org/10.1016/j.nocx.2019.100016.
[22] G. Kumar, P. Neibecker, Y.H. Liu, J. Schroers, Critical fictive temperature for plasticity in metallic glasses, Nat. Commun. 4 (2013). https://doi.org/10.1038/ncomms2546.
[23] Z. Savaedi, R. Motallebi, H. Mirzadeh, M. Malekan, Superplasticity of bulk metallic glasses (BMGs): A review, J. Non. Cryst. Solids. 583 (2022) 121503. https://doi.org/10.1016/j.jnoncrysol.2022.121503.
[24] G. Herzer, Modern soft magnets: Amorphous and nanocrystalline materials, Acta Mater. 61 (2013) 718–734. https://doi.org/10.1016/j.actamat.2012.10.040.
[25] M.E. McHenry, M.A. Willard, D.E. Laughlin, Amorphous and nanocrystalline materials for applications as soft magnets, 1999. https://doi.org/10.1016/S0079-6425(99)00002-X.
[26] V.I. Tkatch, A.I. Limanovskii, S.N. Denisenko, S.G. Rassolov, The effect of the melt-spinning processing parameters on the rate of cooling, Mater. Sci. Eng. A. 323 (2002) 91–96. https://doi.org/10.1016/S0921-5093(01)01346-6.
[27] J.P. Liao, B.J. Yang, Y. Zhang, W.Y. Lu, X.J. Gu, J.Q. Wang, Evaluation of glass formation and critical casting diameter in Al-based metallic glasses, Mater. Des. 88 (2015) 222–226. https://doi.org/10.1016/j.matdes.2015.08.138.
[28] R.M. Ojeda Mota, Stretching the Limits in Thermoplastic Forming of Bulk Metallic Glasses, Yale Graduate School of Arts and Sciences Dissertations, 2021. https://elischolar.library.yale.edu/gsas_dissertations/246.
[29] A. Inoue, K. Kobayashi, T. Masumoto, Mechanical Properties and Thermal Stability of (Fe, Co, Ni)-Mo-C Quaternary Amorphous Alloys, Sci. Reports Res. Institutes, Tohoku Univ. Ser. A, Physics, Chem. Metall. 28 (1980) 172–181.
[30] M. Kikuchi, H. Fujimori, Y. Obi, T. Masumoto, New Amorphous Ferromagnets with Low Coercive Force, Japanese J. Appl. Physics, Part 1 Regul. Pap. Short Notes Rev. Pap. 14 (1975) 1077–1078. https://doi.org/10.1143/JJAP.14.1077.

[31] K. Yamauchi, Y. Nakagawa, Amorphous Ferromagnetic Fe-P-B Alloys Prepared by a New Technique of Splat Cooling, Japanese J. Appl. Physics, Part 1 Regul. Pap. Short Notes Rev. Pap. 10 (1971) 1730. https://doi.org/10.1143/JJAP.10.1730.
[32] A. Inoue, K. Kobayashi, J. Kanehira, T. Masumoto, Mechanical Properties and Thermal Stability of (Fe, Co, Ni)-M-B (M=IV, V and VI Group Transition Metals) Amorphous Alloys with Low Boron Concentration, 1735th Rep. Res. Inst. Iron, Steel Other Met. (1980) 331–342.
[33] A. Datta, N.J. DeCristofaro, Magnetic amorphous metal alloys, US 4321090, 1982.
[34] Y. Yoshizawa, S. Oguma, K. Yamauchi, New Fe-based soft magnetic alloys composed of ultrafine grain structure, J. Appl. Phys. 64 (1988) 6044–6046. https://doi.org/10.1063/1.342149.
[35] K. Suzuki, A. Makino, A. Inoue, T. Masumoto, Soft magnetic properties of nanocrystalline bcc Fe-Zr-B and Fe-M-B-Cu (M=transition metal) alloys with high saturation magnetization (invited), J. Appl. Phys. 70 (1991) 6232–6237. https://doi.org/10.1063/1.350006.
[36] A. Inoue, Y. Shinohara, J.S. Gook, Thermal and Magnetic Properties of Bulk Fe-Based Glassy Alloys Prepared by Copper Mold Casting, Mater. Trans. JIM. 36 (1995) 1427–1433. https://doi.org/10.2320/matertrans1989.36.1427.
[37] T.D. Shen, R.B. Schwarz, Bulk ferromagnetic glasses in the Fe-Ni-P-B stystem, Acta Mater. 49 (2001) 837–847. https://doi.org/10.1016/S1359-6454(00)00365-7.
[38] B. Shen, H. Kimura, A. Inoue, T. Mizushima, Bulk Glassy Fe-Co-Ga-P-C-B Alloys with High Glass-Forming Ability, High Saturation Magnetization and Good Soft Magnetic Properties, Mater. Trans. JIM. 41 (2000) 1675–1678. https://doi.org/10.2320/matertrans1989.41.1675.
[39] A. Inoue, B. Shen, Soft Magnetic Bulk Glassy Fe-B-Si-Nb Alloys with High Saturation Magnetization above 1.5 T, Mater. Trans. 43 (2002) 766–769. https://doi.org/10.2320/matertrans.43.766.
[40] Z.P. Lu, C.T. Liu, J.R. Thompson, W.D. Porter, Structural Amorphous Steels, Phys. Rev. Lett. 92 (2004) 245503. https://doi.org/10.1103/PhysRevLett.92.245503.
[41] V. Ponnambalam, S.J. Poon, G.J. Shiflet, Fe-based bulk metallic glasses with diameter thickness larger than one centimeter, J. Mater. Res. 19 (2004) 1320–1323. https://doi.org/10.1557/JMR.2004.0176.
[42] A. Inoue, F.L. Kong, Q.K. Man, B.L. Shen, R.W. Li, F. Al-Marzouki, Development and applications of Fe- and Co-based bulk glassy alloys and their prospects, J. Alloys Compd. 615 (2014) S2–S8. https://doi.org/10.1016/j.jallcom.2013.11.122.
[43] B. Sarac, Y.P. Ivanov, A. Chuvilin, T. Schöberl, M. Stoica, Z. Zhang, J. Eckert, Origin of large plasticity and multiscale effects in iron-based metallic glasses, Nat. Commun. 9 (2018) 1–10. https://doi.org/10.1038/s41467-018-03744-5.
[44] A. Inoue, N. Nishiyama, New Bulk Metallic Glasses for Applications as Magnetic-Sensing, Chemical, and Structural Materials, MRS Bull. 32 (2007) 651–658. https://doi.org/10.1557/mrs2007.128.
[45] C. Suryanarayana, A. Inoue, Iron-based bulk metallic glasses, Int. Mater.

Rev. 58 (2013) 131–166. https://doi.org/10.1179/1743280412Y.0000000007.
[46] C. Lei, J. Lei, Z. Yang, Y. Zhou, Improved micro fluxgate sensor with double-layer Fe-based amorphous core, Microsyst. Technol. 19 (2013) 167–172. https://doi.org/10.1007/s00542-012-1523-z.
[47] A. Inoue, A. Takeuchi, Bulk nonequilibrium alloys by stabilization of supercooled liquid: Fabrication and functional properties, AIP Conf. Proc. 708 (2004) 547–558. https://doi.org/10.1063/1.1764223.
[48] S.F. Guo, N. Li, C. Zhang, L. Liu, Enhancement of plasticity of Fe-based bulk metallic glass by Ni substitution for Fe, J. Alloys Compd. 504 (2010) 78–81. https://doi.org/10.1016/j.jallcom.2010.02.058.
[49] H.Y. Jung, M. Stoica, S. Yi, D.H. Kim, J. Eckert, Preparation of cast-iron-based nanocrystalline alloy with Cu and Nb addition, Intermetallics. 69 (2016) 54–61. https://doi.org/10.1016/j.intermet.2015.10.014.
[50] J.M. Park, G. Wang, R. Li, N. Mattern, J. Eckert, D.H. Kim, Enhancement of plastic deformability in Fe-Ni-Nb-B bulk glassy alloys by controlling the Ni-to-Fe concentration ratio, Appl. Phys. Lett. 96 (2010) 65–68. https://doi.org/10.1063/1.3291668.
[51] S.F. Guo, L. Liu, N. Li, Y. Li, Fe-based bulk metallic glass matrix composite with large plasticity, Scr. Mater. 62 (2010) 329–332. https://doi.org/10.1016/j.scriptamat.2009.10.024.
[52] Z.B. Jiao, H.X. Li, J.E. Gao, Y. Wu, Z.P. Lu, Effects of alloying elements on glass formation, mechanical and soft-magnetic properties of Fe-based metallic glasses, Intermetallics. 19 (2011) 1502–1508. https://doi.org/10.1016/j.intermet.2011.05.020.
[53] J. Man Park, D. Hyang Kim, M. Stoica, N. Mattern, R. Li, J. Eckert, The influence of in situ formed precipitates on the plasticity of Fe-Nb-B-Cu bulk metallic glasses, J. Mater. Res. 26 (2011) 2080–2086. https://doi.org/10.1557/jmr.2011.202.
[54] S.F. Guo, Y. Shen, Design of high strength Fe-(P, C)-based bulk metallic glasses with Nb addition, Trans. Nonferrous Met. Soc. China (English Ed. 21 (2011) 2433–2437. https://doi.org/10.1016/S1003-6326(11)61032-7.
[55] H.K. Kim, K.B. Lee, J.C. Lee, Ductile Fe-based amorphous alloy, Mater. Sci. Eng. A. 552 (2012). https://doi.org/10.1016/j.msea.2012.05.059.
[56] J. Zhang, C. Chang, A. Wang, B. Shen, Development of quaternary Fe-based bulk metallic glasses with high saturation magnetization above 1.6 T, J. Non. Cryst. Solids. 358 (2012) 1443–1446. https://doi.org/10.1016/j.jnoncrysol.2012.03.023.
[57] A. Seifoddini, M. Stoica, M. Nili-Ahmadabadi, S. Heshmati-Manesh, U. Kühn, J. Eckert, New (Fe 0.9Ni 0.1) 77Mo 5P 9C 7.5B 1.5 glassy alloys with enhanced glass-forming ability and large compressive strain, Mater. Sci. Eng. A. 560 (2013) 575–582. https://doi.org/10.1016/j.msea.2012.09.104.
[58] C. Zhao, C. Dun, Q. Man, B. Shen, Enhancement of plastic deformation in FeCoNbB bulk metallic glass with superhigh strength, Intermetallics. 32 (2013) 408–412. https://doi.org/10.1016/j.intermet.2012.09.018.
[59] S.F. Guo, J.L. Qiu, P. Yu, S.H. Xie, W. Chen, Fe-based bulk metallic glasses: Brittle or ductile?, Appl. Phys. Lett. 105 (2014). https://doi.org/10.1063/1.4899124.
[60] M. Stoica, S. Scudino, J. Bednarčik, I. Kaban, J. Eckert, FeCoSiBNbCu bulk

metallic glass with large compressive deformability studied by time-resolved synchrotron X-ray diffraction, J. Appl. Phys. 115 (2014). https://doi.org/10.1063/1.4864671.
[61] W. Yang, H. Liu, Y. Zhao, A. Inoue, K. Jiang, J. Huo, H. Ling, Q. Li, B. Shen, Mechanical properties and structural features of novel fe-based bulk metallic glasses with unprecedented plasticity, Sci. Rep. 4 (2014) 1–6. https://doi.org/10.1038/srep06233.
[62] J. Wang, W. Cao, L. Wang, S. Zhu, S. Guan, L. Huang, R. Li, T. Zhang, Fe-Al-P-C-B bulk metallic glass with good mechanical and soft magnetic properties, J. Alloys Compd. 637 (2015) 5–9. https://doi.org/10.1016/j.jallcom.2015.02.205.
[63] C. Su, Y. Chen, P. Yu, M. Song, W. Chen, S.F. Guo, Linking the thermal characteristics and mechanical properties of Fe-based bulk metallic glasses, J. Alloys Compd. 663 (2016) 867–871. https://doi.org/10.1016/j.jallcom.2015.12.196.
[64] S. Guo, C. Su, Micro/nano ductile-phases reinforced Fe-based bulk metallic glass matrix composite with large plasticity, Mater. Sci. Eng. A. 707 (2017) 44–50. https://doi.org/10.1016/j.msea.2017.09.036.
[65] C. Wan, W. Yang, H. Liu, M. Zuo, Q. Li, Z. Ma, Y. Zhao, A. Inoue, Ductile Fe-based bulk metallic glasses at room temperature, Mater. Sci. Technol. (United Kingdom). 34 (2018) 751–756. https://doi.org/10.1080/02670836.2017.1412037.
[66] D. dan Liang, X. shun Wei, C. tao Chang, J. wei Li, X. min Wang, J. Shen, Effect of W addition on the glass forming ability and mechanical properties of Fe-based metallic glass, J. Alloys Compd. 731 (2018) 1146–1150. https://doi.org/10.1016/j.jallcom.2017.10.104.
[67] Y.X. Geng, X. Lin, J. Li, S.M. Fan, H.B. Ju, L.H. Yu, J.H. Xu, Y.M. Wang, Super-high hardness of (Fe,Co)-B-Si-Zr/Hf bulk glassy alloys, J. Alloys Compd. 753 (2018) 351–355. https://doi.org/10.1016/j.jallcom.2018.04.244.
[68] J. Zhou, B. Sun, Q. Wang, Q. Yang, W. Yang, B. Shen, Effects of Ni and Si additions on mechanical properties and serrated flow behavior in FeMoPCB bulk metallic glasses, J. Alloys Compd. 783 (2019) 555–564. https://doi.org/10.1016/j.jallcom.2018.12.331.
[69] F. Hu, C. Yuan, Q. Luo, W. Yang, B. Shen, Effects of heavy rare-earth addition on glass-forming ability, thermal, magnetic, and mechanical properties of Fe-RE-B-Nb (RE = Dy, Ho, Er or Tm) bulk metallic glass, J. Non. Cryst. Solids. 525 (2019) 119681. https://doi.org/10.1016/j.jnoncrysol.2019.119681.
[70] M. Tkaczyk, M. Hasiak, J. Kaleta, K.I. Dragnevski, Microstructural investigation and mechanical properties of rapidly solidified bulk nanocrystalline Fe-based alloys, Mater. Today Proc. 33 (2020) 1775–1780. https://doi.org/10.1016/j.matpr.2020.05.050.
[71] J. Li, Y. Ma, Q. Li, J. Shen, H. Liu, Y. Zhao, W. Yang, Fe-based bulk metallic glass with unprecedented plasticity at room temperature, Intermetallics. 139 (2021) 107377. https://doi.org/10.1016/j.intermet.2021.107377.
[72] T. Liu, L. Lai, S. Xiao, M. Tang, H. Zhang, S. Guo, Ternary Fe–W–B bulk metallic glasses with ultrahigh thermal stabilities, Mater. Sci. Eng. A. 826 (2021) 142034. https://doi.org/10.1016/j.msea.2021.142034.

[73] C. ran Fu, W. Zhang, Q. chun Xiang, Y. dong Qu, Y. lei Ren, B. Yu, K. qiang Qiu, Glass formation in Fe-Cr-Zr-B-Mo alloys by tuning Nb addition, China Foundry. 18 (2021) 450–456. https://doi.org/10.1007/s41230-021-1061-3.
[74] J. Zhou, Q. Wang, Q. Zeng, K. Yin, A. Wang, J. Luan, L. Sun, B. Shen, A plastic FeNi-based bulk metallic glass and its deformation behavior, J. Mater. Sci. Technol. 76 (2021) 20–32. https://doi.org/10.1016/j.jmst.2020.11.016.
[75] C.Y. Liu, Y.X. Zhang, C.Y. Zhang, G. Yuan, J. Kang, Z.L. Li, R.D.K. Misra, Microstructure and performance of novel ductile FeNi-based metallic glasses, J. Alloys Compd. 892 (2022). https://doi.org/10.1016/j.jallcom.2021.162054.
[76] N. Yodoshi, R. Yamada, A. Kawasaki, A. Makino, Micro viscous flow processing of Fe-based metallic glassy particles, J. Alloys Compd. 615 (2014) S61–S66. https://doi.org/10.1016/j.jallcom.2013.12.256.
[77] J. Blink, J. Farmer, J. Choi, C. Saw, Applications in the nuclear industry for thermal spray amorphous metal and ceramic coatings, Metall. Mater. Trans. A Phys. Metall. Mater. Sci. 40 (2009) 1344–1354. https://doi.org/10.1007/s11661-009-9830-4.
[78] J.B. Cheng, X.B. Liang, Z.H. Wang, B.S. Xu, Microstructure and mechanical properties of febsinb metallic glass coatings by twin wire arc spraying, J. Therm. Spray Technol. 22 (2013) 471–477. https://doi.org/10.1007/s11666-013-9892-0.
[79] J.B. Cheng, Z.H. Wang, B.S. Xu, Wear and corrosion behaviors of FeCrBSiNbW amorphous/nanocrystalline coating prepared by arc spraying process, J. Therm. Spray Technol. 21 (2012) 1025–1031. https://doi.org/10.1007/s11666-012-9779-5.
[80] Y. Zhang, L. Wu, X. Guo, S. Kane, Y. Deng, Y.G. Jung, J.H. Lee, J. Zhang, Additive Manufacturing of Metallic Materials: A Review, J. Mater. Eng. Perform. 27 (2018) 1–13. https://doi.org/10.1007/s11665-017-2747-y.
[81] S. Kumar, Additive Manufacturing Processes, Springer International Publishing, Cham, 2020. https://doi.org/10.1007/978-3-030-45089-2.
[82] Z. Mao, X. Lu, H. Yang, X. Niu, L. Zhang, X. Xie, Processing optimization, microstructure, mechanical properties and nanoprecipitation behavior of 18Ni300 maraging steel in selective laser melting, Mater. Sci. Eng. A. 830 (2022). https://doi.org/10.1016/j.msea.2021.142334.
[83] S.Y. Zhou, Y. Su, H. Wang, J. Enz, T. Ebel, M. Yan, Selective laser melting additive manufacturing of 7xxx series Al-Zn-Mg-Cu alloy: Cracking elimination by co-incorporation of Si and TiB2, Addit. Manuf. 36 (2020). https://doi.org/10.1016/j.addma.2020.101458.
[84] E.C. Santos, M. Shiomi, K. Osakada, T. Laoui, Rapid manufacturing of metal components by laser forming, Int. J. Mach. Tools Manuf. 46 (2006) 1459–1468. https://doi.org/10.1016/j.ijmachtools.2005.09.005.
[85] W. Chen, Z. Li, Additive manufacturing of titanium aluminides, in: Addit. Manuf. Aerosp. Ind., 2019. https://doi.org/10.1016/B978-0-12-814062-8.00013-3.
[86] I. Yadroitsev, P. Krakhmalev, I. Yadroitsava, Selective laser melting of Ti6Al4V alloy for biomedical applications: Temperature monitoring and microstructural evolution, J. Alloys Compd. 583 (2014).

https://doi.org/10.1016/j.jallcom.2013.08.183.
[87] E. Fereiduni, A. Ghasemi, M. Elbestawi, Selective laser melting of aluminum and titanium matrix composites: Recent progress and potential applications in the aerospace industry, Aerospace. 7 (2020). https://doi.org/10.3390/AEROSPACE7060077.
[88] A. Gisario, M. Kazarian, F. Martina, M. Mehrpouya, Metal additive manufacturing in the commercial aviation industry: A review, J. Manuf. Syst. 53 (2019). https://doi.org/10.1016/j.jmsy.2019.08.005.
[89] S.L. Sing, J. An, W.Y. Yeong, F.E. Wiria, Laser and electron-beam powder-bed additive manufacturing of metallic implants: A review on processes, materials and designs, J. Orthop. Res. 34 (2016) 369–385. https://doi.org/10.1002/jor.23075.
[90] D. Gu, H. Wang, D. Dai, P. Yuan, W. Meiners, R. Poprawe, Rapid fabrication of Al-based bulk-form nanocomposites with novel reinforcement and enhanced performance by selective laser melting, Scr. Mater. 96 (2015) 25–28. https://doi.org/10.1016/j.scriptamat.2014.10.011.
[91] Q. Chen, G. Guillemot, C.-A. Gandin, M. Bellet, Finite element modeling of deposition of ceramic material during SLM additive manufacturing, MATEC Web Conf. 80 (2016) 08001. https://doi.org/10.1051/matecconf/20168008001.
[92] S. Chowdhury, N. Yadaiah, C. Prakash, S. Ramakrishna, S. Dixit, L.R. Gupta, D. Buddhi, Laser powder bed fusion: a state-of-the-art review of the technology, materials, properties & defects, and numerical modelling, J. Mater. Res. Technol. 20 (2022) 2109–2172. https://doi.org/10.1016/j.jmrt.2022.07.121.
[93] L. Deng, S. Wang, P. Wang, U. Kühn, S. Pauly, Selective laser melting of a Ti-based bulk metallic glass, Mater. Lett. 212 (2018) 346–349. https://doi.org/10.1016/j.matlet.2017.10.130.
[94] E.M. Sefene, State-of-the-art of selective laser melting process: A comprehensive review, J. Manuf. Syst. 63 (2022) 250–274. https://doi.org/10.1016/j.jmsy.2022.04.002.
[95] X.D. Nong, X.L. Zhou, Y.X. Ren, Fabrication and characterization of Fe-based metallic glasses by Selective Laser Melting, Opt. Laser Technol. 109 (2019) 20–26. https://doi.org/10.1016/j.optlastec.2018.07.059.
[96] C.Y. Yap, C.K. Chua, Z.L. Dong, An effective analytical model of selective laser melting, Virtual Phys. Prototyp. 11 (2016). https://doi.org/10.1080/17452759.2015.1133217.
[97] H. Gu, H. Gong, D. Pal, K. Rafi, T. Starr, B. Stucker, Influences of energy density on porosity and microstructure of selective laser melted 17-4PH stainless steel, 24th Int. SFF Symp. - An Addit. Manuf. Conf. SFF 2013. (2013) 474–489.
[98] L.C. Zhang, D. Klemm, J. Eckert, Y.L. Hao, T.B. Sercombe, Manufacture by selective laser melting and mechanical behavior of a biomedical Ti-24Nb-4Zr-8Sn alloy, Scr. Mater. 65 (2011). https://doi.org/10.1016/j.scriptamat.2011.03.024.
[99] S. Greco, K. Gutzeit, H. Hotz, B. Kirsch, J.C. Aurich, Selective laser melting (SLM) of AISI 316L—impact of laser power, layer thickness, and hatch spacing on roughness, density, and microhardness at constant input energy density, Int. J. Adv. Manuf. Technol. 108 (2020) 1551–1562.

https://doi.org/10.1007/s00170-020-05510-8.
[100] J. Chen, X. Wang, Y. Pan, Influence of laser power and scan speed on the microstructure and properties of GH4169 alloy prepared by selective laser melting, in: IOP Conf. Ser. Mater. Sci. Eng., 2019. https://doi.org/10.1088/1757-899X/688/3/033064.
[101] J. Liu, Y. Song, C. Chen, X. Wang, H. Li, C. Zhou, J. Wang, K. Guo, J. Sun, Effect of scanning speed on the microstructure and mechanical behavior of 316L stainless steel fabricated by selective laser melting, Mater. Des. 186 (2020). https://doi.org/10.1016/j.matdes.2019.108355.
[102] N.T. Aboulkhair, N.M. Everitt, I. Ashcroft, C. Tuck, Reducing porosity in AlSi10Mg parts processed by selective laser melting, Addit. Manuf. 1 (2014) 77–86. https://doi.org/10.1016/j.addma.2014.08.001.
[103] D. Dai, D. Gu, Thermal behavior and densification mechanism during selective laser melting of copper matrix composites: Simulation and experiments, Mater. Des. 55 (2014). https://doi.org/10.1016/j.matdes.2013.10.006.
[104] M. Xia, D. Gu, G. Yu, D. Dai, H. Chen, Q. Shi, Porosity evolution and its thermodynamic mechanism of randomly packed powder-bed during selective laser melting of Inconel 718 alloy, Int. J. Mach. Tools Manuf. 116 (2017). https://doi.org/10.1016/j.ijmachtools.2017.01.005.
[105] M. Ma, Z. Wang, M. Gao, X. Zeng, Layer thickness dependence of performance in high-power selective laser melting of 1Cr18Ni9Ti stainless steel, J. Mater. Process. Technol. 215 (2015). https://doi.org/10.1016/j.jmatprotec.2014.07.034.
[106] C. Zhang, Q. Liao, X. Zhang, F. Ma, M. Wu, Q. Xu, Characterization of porosity in lack of fusion pores in selective laser melting using the wavefunction, Mater. Res. Express. 10 (2023) 016501. https://doi.org/10.1088/2053-1591/acaf24.
[107] A. Du Plessis, Porosity in laser powder bed fusion, in: Fundam. Laser Powder Bed Fusion Met., Elsevier, 2021: pp. 155–178. https://doi.org/10.1016/B978-0-12-824090-8.00007-X.
[108] Y. Huang, T.G. Fleming, S.J. Clark, S. Marussi, K. Fezzaa, J. Thiyagalingam, C.L.A. Leung, P.D. Lee, Keyhole fluctuation and pore formation mechanisms during laser powder bed fusion additive manufacturing, Nat. Commun. 13 (2022) 1–11. https://doi.org/10.1038/s41467-022-28694-x.
[109] D.L. Bourell, T. Wohlers, ASM Handbook Volume 24: Additive Manufacturing, Addit. Manuf. Process. 24 (2020).
[110] A.B. Phillion, S.L. Cockcroft, P.D. Lee, X-ray micro-tomographic observations of hot tear damage in an Al-Mg commercial alloy, Scr. Mater. 55 (2006). https://doi.org/10.1016/j.scriptamat.2006.03.035.
[111] S. Kou, Solidification and liquation cracking issues in welding, Jom. 55 (2003) 37–42. https://doi.org/10.1007/s11837-003-0137-4.
[112] J. Zhang, B. Song, Q. Wei, D. Bourell, Y. Shi, A review of selective laser melting of aluminum alloys: Processing, microstructure, property and developing trends, J. Mater. Sci. Technol. 35 (2019). https://doi.org/10.1016/j.jmst.2018.09.004.
[113] Y.S. Huo, C. Hong, H.X. Li, P. Liu, Influence of different processing parameter on distortion and residual stress of inconel 718 alloys fabricated

by selective laser melting (SLM), Mater. Res. 23 (2021). https://doi.org/10.1590/1980-5373-MR-2020-0176.
[114] M. Shiomi, K. Osakada, K. Nakamura, T. Yamashita, F. Abe, Residual stress within metallic model made by selective laser melting process, CIRP Ann. - Manuf. Technol. 53 (2004). https://doi.org/10.1016/S0007-8506(07)60677-5.
[115] W. Zhang, M. Tong, N.M. Harrison, Scanning strategies effect on temperature, residual stress and deformation by multi-laser beam powder bed fusion manufacturing, Addit. Manuf. 36 (2020) 101507. https://doi.org/10.1016/j.addma.2020.101507.
[116] H. Wu, D. Zhang, B. Yang, C. Chen, Y. Li, K. Zhou, L. Jiang, R. Liu, Microstructural evolution and defect formation in a powder metallurgy nickel-based superalloy processed by selective laser melting, J. Mater. Sci. Technol. 36 (2020). https://doi.org/10.1016/j.jmst.2019.08.007.
[117] K.H. Ko, H.G. Kang, Y.H. Huh, C.J. Park, L.R. Cho, Effects of heat treatment on the microstructure, residual stress, and mechanical properties of Co–Cr alloy fabricated by selective laser melting, J. Mech. Behav. Biomed. Mater. 126 (2022). https://doi.org/10.1016/j.jmbbm.2021.105051.
[118] Y. Li, H. Qi, H. Hou, L. Lei, Effects of Hot Isostatic Pressing on Microstructure and Mechanical Properties of Hastelloy X Samples Produced by Selective Laser Melting, in: Proc. Second Int. Conf. Mech. Mater. Struct. Eng. (ICMMSE 2017), Atlantis Press, n.d.: pp. 31–40. https://doi.org/10.2991/icmmse-17.2017.6.
[119] A. Kreitcberg, V. Brailovski, S. Turenne, C. Chanal, V. Urlea, Influence of thermo- and HIP treatments on the microstructure and mechanical properties of IN625 alloy parts produced by selective laser melting: A comparative study, in: Mater. Sci. Forum, 2017. https://doi.org/10.4028/www.scientific.net/MSF.879.1008.
[120] S. Pauly, L. Löber, R. Petters, M. Stoica, S. Scudino, U. Kühn, J. Eckert, Processing metallic glasses by selective laser melting, Mater. Today. 16 (2013) 37–41. https://doi.org/10.1016/j.mattod.2013.01.018.
[121] H.Y. Jung, S.J. Choi, K.G. Prashanth, M. Stoica, S. Scudino, S. Yi, U. Kühn, D.H. Kim, K.B. Kim, J. Eckert, Fabrication of Fe-based bulk metallic glass by selective laser melting: A parameter study, Mater. Des. 86 (2015) 703–708. https://doi.org/10.1016/j.matdes.2015.07.145.
[122] N. Li, J. Zhang, W. Xing, D. Ouyang, L. Liu, 3D printing of Fe-based bulk metallic glass composites with combined high strength and fracture toughness, Mater. Des. 143 (2018) 285–296. https://doi.org/10.1016/j.matdes.2018.01.061.
[123] D. Ouyang, W. Xing, N. Li, Y. Li, L. Liu, Structural evolutions in 3D-printed Fe-based metallic glass fabricated by selective laser melting, Addit. Manuf. 23 (2018) 246–252. https://doi.org/10.1016/j.addma.2018.08.020.
[124] W. Xing, D. Ouyang, N. Li, L. Liu, Insight into micro-cracking in 3D-printed Fe-based BMGs by selective laser melting, Intermetallics. 103 (2018) 101–106. https://doi.org/10.1016/j.intermet.2018.10.011.
[125] Z. Mahbooba, L. Thorsson, M. Unosson, P. Skoglund, H. West, T. Horn, C. Rock, E. Vogli, O. Harrysson, Additive manufacturing of an iron-based bulk metallic glass larger than the critical casting thickness, Appl. Mater. Today. 11 (2018) 264–269. https://doi.org/10.1016/j.apmt.2018.02.011.

[126] Ł. Żrodowski, B. Wysocki, R. Wróblewski, A. Krawczyńska, B. Adamczyk-Cieślak, J. Zdunek, P. Błyskun, J. Ferenc, M. Leonowicz, W. Święszkowski, New approach to amorphization of alloys with low glass forming ability via selective laser melting, J. Alloys Compd. 771 (2019) 769–776. https://doi.org/10.1016/j.jallcom.2018.08.075.
[127] S. Alleg, R. Drablia, N. Fenineche, Effect of the Laser Scan Rate on the Microstructure, Magnetic Properties, and Microhardness of Selective Laser-Melted FeSiB, J. Supercond. Nov. Magn. 31 (2018). https://doi.org/10.1007/s10948-018-4621-z.
[128] Y.G. Nam, B. Koo, M.S. Chang, S. Yang, J. Yu, Y.H. Park, J.W. Jeong, Selective laser melting vitrification of amorphous soft magnetic alloys with help of double-scanning-induced compositional homogeneity, Mater. Lett. 261 (2020) 127068. https://doi.org/10.1016/j.matlet.2019.127068.
[129] Ł. Szczepański, M. Bambach, F. Jensch, A. Ambroziak, T. Kurzynowski, Structural investigations of Fe-Zr-Si-Cu metallic glass with low glass-forming ability produced in laser powder bed fusion technology, Mater. Des. 210 (2021). https://doi.org/10.1016/j.matdes.2021.110112.
[130] Q. Jiang, P. Zhang, Z. Yu, Y. Tian, S. Ma, AlCoCrFeNi high entropy alloy fabricated via selective laser melting reinforced by Fe-based metallic glass, Mater. Lett. 307 (2022). https://doi.org/10.1016/j.matlet.2021.130994.
[131] H. Wang, J. Chen, H. Luo, D. Wang, C. Song, X. Yao, P. Chen, M. Yan, Bimetal printing of high entropy alloy/metallic glass by laser powder bed fusion additive manufacturing, Intermetallics. 141 (2022). https://doi.org/10.1016/j.intermet.2021.107430.
[132] X.Y. Yao, J.C. Tang, Y.H. Zhou, Z.Z. Huang, J.B. Xu, Y. Long, L.L. Tan, B. Wiese, T. Ebel, M. Yan, Selective laser melting of an Mg/Metallic Glass hybrid for significantly improving chemical and mechanical performances, Appl. Surf. Sci. 580 (2022). https://doi.org/10.1016/j.apsusc.2021.152229.
[133] Q. Jiang, P. Zhang, J. Tan, Z. Yu, Y. Tian, S. Ma, D. Wu, Influence of the microstructure on mechanical properties of SLM additive manufacturing Fe-based bulk metallic glasses, J. Alloys Compd. 894 (2022). https://doi.org/10.1016/j.jallcom.2021.162525.
[134] L. Thorsson, M. Unosson, M. Teresa Pérez-Prado, X. Jin, P. Tiberto, G. Barrera, B. Adam, N. Neuber, A. Ghavimi, M. Frey, R. Busch, I. Gallino, Selective laser melting of a Fe-Si-Cr-B-C-based complex-shaped amorphous soft-magnetic electric motor rotor with record dimensions, Mater. Des. 215 (2022) 110483. https://doi.org/10.1016/j.matdes.2022.110483.
[135] J. Long, D.E. Laughlin, M.E. McHenry, Structural and soft magnetic properties of a new nanocrystalline Fe-based and B-free alloy, in: J. Appl. Phys., 2008: pp. 79–81. https://doi.org/10.1063/1.2829396.
[136] M. Kopcewicz, A. Grabias, J. Latuch, M. Kowalczyk, Soft magnetic amorphous Fe–Zr–Si(Cu) boron-free alloys, Mater. Chem. Phys. 126 (2011) 669–675. https://doi.org/10.1016/j.matchemphys.2010.12.064.
[137] M. Kopcewicz, A. Grabias, J. Latuch, Nanocrystalline Fe–Zr–Si(Cu) boron-free alloys, Intermetallics. 33 (2013) 92–98. https://doi.org/10.1016/j.intermet.2012.10.002.
[138] K. Hono, K. Hiraga, Q. Wang, A. Inoue, T. Sakurai, The microstructure evolution of a Fe73.5Si13.5B9Nb3Cu1 nanocrystalline soft magnetic

material, Acta Metall. Mater. 40 (1992) 2137–2147. https://doi.org/10.1016/0956-7151(92)90131-W.
[139] J.D. Ayers, V.G. Harris, J.A. Sprague, W.T. Elam, H.N. Jones, On the formation of nanocrystals in the soft magnetic alloy Fe73.5Nb3CU1Si13.5B9, Acta Mater. 46 (1998) 1861–1874. https://doi.org/10.1016/S1359-6454(97)00436-9.
[140] Y.C. Li, C. Zhang, W. Xing, S.F. Guo, L. Liu, Design of Fe-Based Bulk Metallic Glasses with Improved Wear Resistance, ACS Appl. Mater. Interfaces. 10 (2018) 43144–43155. https://doi.org/10.1021/acsami.8b11561.
[141] Y. Lv, Q. Chen, Y. Huang, Tunable Curie temperature and magnetocaloric effect of FeCrMoCBYNi bulk metallic glass with different crystallized phases, J. Rare Earths. 37 (2019) 404–409. https://doi.org/10.1016/j.jre.2018.07.017.
[142] M. Klinger, A. Jäger, Crystallographic Tool Box (CrysTBox): Automated tools for transmission electron microscopists and crystallographers, J. Appl. Crystallogr. 48 (2015) 2012–2018. https://doi.org/10.1107/S1600576715017252.
[143] N. Doebelin, R. Kleeberg, Profex: A graphical user interface for the Rietveld refinement program BGMN, J. Appl. Crystallogr. 48 (2015) 1573–1580. https://doi.org/10.1107/S1600576715014685.
[144] P. Karimi, T. Raza, J. Andersson, L.E. Svensson, Influence of laser exposure time and point distance on 75-µm-thick layer of selective laser melted Alloy 718, Int. J. Adv. Manuf. Technol. 94 (2018) 2199–2207. https://doi.org/10.1007/s00170-017-1019-1.
[145] Q. Jiang, H. Liu, J. Li, D. Yang, Y. Zhang, W. Yang, Atomic-level understanding of crystallization in the selective laser melting of Fe50Ni50 amorphous alloy, Addit. Manuf. 34 (2020) 101369. https://doi.org/10.1016/j.addma.2020.101369.
[146] S.X. Liang, X. Wang, W. Zhang, Y.J. Liu, W. Wang, L.C. Zhang, Selective laser melting manufactured porous Fe-based metallic glass matrix composite with remarkable catalytic activity and reusability, Appl. Mater. Today. 19 (2020) 100543. https://doi.org/10.1016/j.apmt.2019.100543.
[147] H. Liu, Q. Jiang, J. Huo, Y. Zhang, W. Yang, X. Li, Crystallization in additive manufacturing of metallic glasses: A review, Addit. Manuf. 36 (2020) 101568. https://doi.org/10.1016/j.addma.2020.101568.
[148] A. Sola, A. Nouri, Microstructural porosity in additive manufacturing: The formation and detection of pores in metal parts fabricated by powder bed fusion, J. Adv. Manuf. Process. 1 (2019) 1–21. https://doi.org/10.1002/amp2.10021.
[149] R. Li, J. Liu, Y. Shi, L. Wang, W. Jiang, Balling behavior of stainless steel and nickel powder during selective laser melting process, Int. J. Adv. Manuf. Technol. 59 (2012) 1025–1035. https://doi.org/10.1007/s00170-011-3566-1.
[150] C.Y. Yap, C.K. Chua, Z.L. Dong, Z.H. Liu, D.Q. Zhang, L.E. Loh, S.L. Sing, Review of selective laser melting: Materials and applications, Appl. Phys. Rev. 2 (2015). https://doi.org/10.1063/1.4935926.
[151] J.P. Oliveira, T.G. Santos, R.M. Miranda, Revisiting fundamental welding concepts to improve additive manufacturing: From theory to practice, Prog. Mater. Sci. 107 (2020) 100590.

https://doi.org/10.1016/j.pmatsci.2019.100590.
[152] Y. Zou, Z. Qiu, C. Tan, Y. Wu, K. Li, D. Zeng, Microstructure and mechanical properties of Fe-based bulk metallic glass composites fabricated by selective laser melting, J. Non. Cryst. Solids. 538 (2020) 120046. https://doi.org/10.1016/j.jnoncrysol.2020.120046.
[153] N. Li, S. Wu, D. Ouyang, J. Zhang, L. Liu, Fe-based metallic glass reinforced FeCoCrNiMn high entropy alloy through selective laser melting, J. Alloys Compd. 822 (2020) 153695. https://doi.org/10.1016/j.jallcom.2020.153695.
[154] L. Wang, H. Wang, Y. Liu, Z. Fu, T. Peng, J. Shen, S. Zhou, M. Yan, G. Wang, Y. Dai, Selective laser melting helps fabricate record-large bulk metallic glass: Experiments, simulation and demonstrative part, J. Alloys Compd. 808 (2019). https://doi.org/10.1016/j.jallcom.2019.151731.
[155] J. Suryawanshi, K.G. Prashanth, U. Ramamurty, Mechanical behavior of selective laser melted 316L stainless steel, Mater. Sci. Eng. A. 696 (2017) 113–121. https://doi.org/10.1016/j.msea.2017.04.058.
[156] Y.M. Zou, Y.S. Wu, K.F. Li, C.L. Tan, Z.G. Qiu, D.C. Zeng, Selective laser melting of crack-free Fe-based bulk metallic glass via chessboard scanning strategy, Mater. Lett. 272 (2020) 2–5. https://doi.org/10.1016/j.matlet.2020.127824.
[157] Y. Lu, S. Wu, Y. Gan, T. Huang, C. Yang, L. Junjie, J. Lin, Study on the microstructure, mechanical property and residual stress of SLM Inconel-718 alloy manufactured by differing island scanning strategy, Opt. Laser Technol. 75 (2015). https://doi.org/10.1016/j.optlastec.2015.07.009.
[158] K. Nomoto, A. V. Ceguerra, C. Gammer, B. Li, H. Bilal, A. Hohenwarter, B. Gludovatz, J. Eckert, S.P. Ringer, J.J. Kruzic, Medium-range order dictates local hardness in bulk metallic glasses, Mater. Today. 44 (2021) 48–57. https://doi.org/10.1016/j.mattod.2020.10.032.
[159] A. Inoue, S. Arakawa, T. Masumoto, Effect of Alloying Elements on Defect Structure and Hardness of M23C6 Type Carbides., Trans. Japan Inst. Met. 20 (1979) 585–592. https://doi.org/10.2320/matertrans1960.20.585.
[160] M. Shiomi, K. Osakada, K. Nakamura, T. Yamashita, F. Abe, Residual stress within metallic model made by selective laser melting process, CIRP Ann. - Manuf. Technol. 53 (2004) 195–198. https://doi.org/10.1016/S0007-8506(07)60677-5.
[161] M. Gerstgrasser, Selective laser melting of CM247LC, ETH Zurich, 2021. https://doi.org/10.3929/ethz-b-000529003.